

## ESD ACCESSION LIST

ESTI Call No. 70612Copy No. 1 of 1 cys.

## Technical Report

473

Development of UHF Switch  
for LES-6 Satellite

R. N. Assaly

4 December 1969

Prepared under Electronic Systems Division Contract AF 19(628)-5167 by

## Lincoln Laboratory

MASSACHUSETTS INSTITUTE OF TECHNOLOGY

Lexington, Massachusetts



ESD RECORD COPY

RETURN TO  
SCIENTIFIC & TECHNICAL INFORMATION DIVISION  
(ESTI), BUILDING 1211

AD 710612



This document has been approved for public release and sale;  
its distribution is unlimited.

MASSACHUSETTS INSTITUTE OF TECHNOLOGY  
LINCOLN LABORATORY

DEVELOPMENT OF UHF SWITCH FOR LES-6 SATELLITE

*R. N. Assaly*

*Group 68*

TECHNICAL REPORT 473

4 DECEMBER 1969

This document has been approved for public release and sale;  
its distribution is unlimited.

The work reported in this document was performed at Lincoln Laboratory, a center for research operated by Massachusetts Institute of Technology, with the support of the Department of the Air Force under Contract AF 19(628)-5167.

This report may be reproduced to satisfy needs of U.S. Government agencies.

Non-Lincoln Recipients

**PLEASE DO NOT RETURN**

Permission is given to destroy this document  
when it is no longer needed



## ABSTRACT

A UHF switch matrix was developed for the LES-6 satellite to electronically despun the antenna beam as the satellite rotated on its axis. Initially, a study was carried out to determine the optimum antenna system and switch configuration for the constraints of satellite geometry and minimal complexity. Two such switch matrices, operated by logic circuits and sun and earth sensors, were used on the satellite, one to excite two adjacent of eight pairs of antenna dipoles, and the other to excite two adjacent of eight pairs of cavity-backed slots. The polarizations of the signals from the dipoles and slots are orthogonal and by adjusting the phase difference to  $90^\circ$ , the satellite will transmit and receive on right-hand circular polarization during normal operation. Furthermore, by squinting the beam formed by two element pairs  $+11.25^\circ$  or  $-11.25^\circ$  from the center line of the element pairs, any of 16 beams can be formed which are equally spaced in azimuth about the satellite. Each switch consists of three parts, namely, a hybrid to divide the input power into two equal parts, a 2P2T section which switches phase, and two SP4T sections to switch on two antenna pairs.

The switch was built in strip transmission line using PIN diodes in series with the inner conductor as the switching element. In its development, a number of conflicting characteristics were required to be optimized. These include the RF characteristics such as VSWR, insertion loss, and isolation; thermal heating of the diodes which determine their reliability; and intermodulation products, switching noise, and random noise which can degrade the satellite receiver performance. It was also necessary to demonstrate that the switch was free from multipactor breakdown and could survive prolonged space radiation. Finally, it had to be proven that the switch had good reliability under the stresses of the rocket launch and through an expected 5-year life in orbit.

A detailed discussion of the testing programs is given, as this type of information is not generally available in the open literature.

Accepted for the Air Force  
Franklin C. Hudson  
Chief, Lincoln Laboratory Office

## CONTENTS

Abstract	iii
I. INTRODUCTION	1
II. SWITCH CIRCUIT AND ITS COMPONENTS	7
A. Switch Matrix Circuit and Basic Operation	7
B. SPST Unit	9
C. PIN Diode	9
D. Strip Transmission Line	13
E. 0.68- $\mu$ H Coil	21
F. Ferrite Coil	21
G. Capacitor	21
H. Boron Nitride	22
I. Coaxial Connector	22
J. 3-dB Hybrid and Joining Cables	22
III. DEVELOPMENT, CONSTRUCTION AND CHARACTERISTICS OF SWITCH MATRIX	23
A. Laying Out the Switch	23
B. Steps in Switch Development	25
C. Assembly	31
D. Switch Performance	35
IV. MEASURED AND THEORETICAL PERFORMANCE OF SEVERAL SWITCH CONFIGURATIONS	41
A. SPST and SP2T Switches	41
B. Theoretical Approach to Loss of SPnT Switch	41
V. TEMPERATURE PROBLEM	44
A. Introduction	44
B. Diode and SPST Unit	45
C. Switch Matrix Temperatures	48
VI. MULTIPACTOR	50
VII. INTERMODULATION PRODUCTS	52
A. General	52
B. Intermodulation Products from the PIN Diodes	55
C. Intermodulation Products Generated in Switch Matrix	65
VIII. SWITCHING NOISE	66
A. PIN Diode	66
B. Switch Matrix	72

IX. NOISE FIGURE	73
A. Basic Aspects	73
B. PIN Diode and SPST Unit	76
C. Switch Matrix	78
X. EFFECT OF RADIATION DOSAGE IN ORBIT	79
XI. RELIABILITY	82
A. Various Considerations Involved	82
B. PIN Diodes – Accelerated Life Tests	83
C. PIN Diodes – Screening	89
D. Switch Matrix – Mechanical Tests	89
E. Switch Matrix – Thermal Cycle	91
XII. ANTENNA PATTERNS AND CHOICE OF SWITCH MATRIX CONFIGURATION	92
A. Discussion of Antenna Patterns in General	92
B. Arrangements of Antenna Excitations and Beams	100
C. Calculated Antenna Patterns	103
D. Pattern Measurements	105
E. Choice of Configuration for the Switch Matrix	107
XIII. CONCLUSIONS	108
APPENDIX A – Summary of Characteristics of LES-6 Switches	
APPENDIX B	
APPENDIX C – Quality Assurance Screening Specifications for PIN Diode for LES-6 Switch Matrix	117
References	121



# DEVELOPMENT OF UHF SWITCH FOR LES-6 SATELLITE

## I. INTRODUCTION

This report describes the evolution of the design of an RF switch used to despin the antenna beam on the LES-6 satellite as it rotates on its axis. Many design considerations had to be taken into account and the following description indicates how increasingly complex the project became as an attempt was made to satisfy all the conditions simultaneously. This report, in addition to giving a full description of the switch, serves a second purpose. It provides a model testing program, which is not otherwise given in the general literature, on a solid state device for use on satellites. We then hope to fulfill two main objectives here: to demonstrate that an RF solid state switch in a satellite antenna system is practical despite the many problems encountered, and to convey information on a suitable testing program needed for the development of a satellite component like the switch.

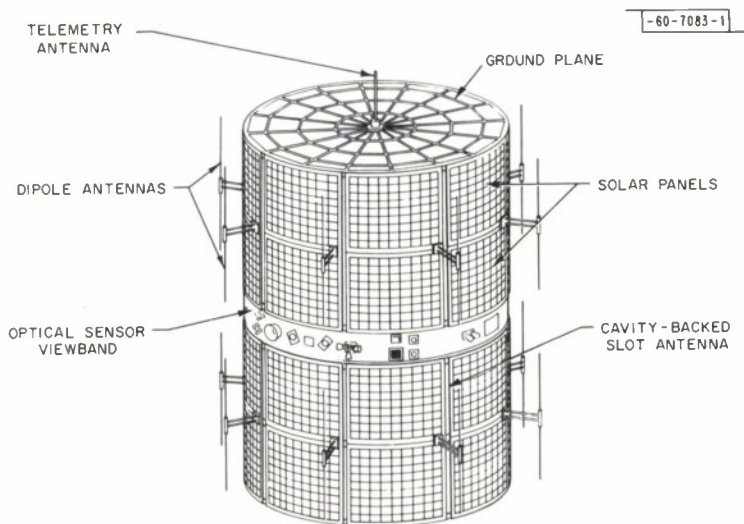


Fig. 1. Configuration of LES-6 satellite.

The satellite in question (Fig. 1) is cylinder shaped, 66 inches long and 48 inches in diameter, covered with 32 solar panels except for a 6-inch wide band around the center. Separating the panels, top and bottom, are eight pairs of slots equally spaced around the satellite that provide a radiation field with a polarization perpendicular to the cylinder axis. Directly over each slot and parallel to it is a dipole supported 6 inches from the cylinder to provide the orthogonal polarization. Appropriate electrical phasing of the excitations of the slots and dipoles provides

TABLE I PARAMETERS OF RF SIGNALS IN SATELLITE				
Signal	Center Frequency (MHz)	Bandwidth (MHz)	Power Level (W)	Expected Sensitivity (dBm)
Transmitter	$f_T \approx 250$	0.5	$P_T = 100$ (+50 dBm)	-120
Receiver	$f_R = f_T + 50.0$	0.5		
Beacon	$f_B = f_T + 5.0$	0	$P_B = 4$ (+36 dBm)	-120
RFI	$f_{RFI} = f_T + 40.0$ to $f_T + 65.0$	25.0		
Telemetry	$f_L = f_T - 12.4$	0	$P_L = 1$ (+30 dBm)	-

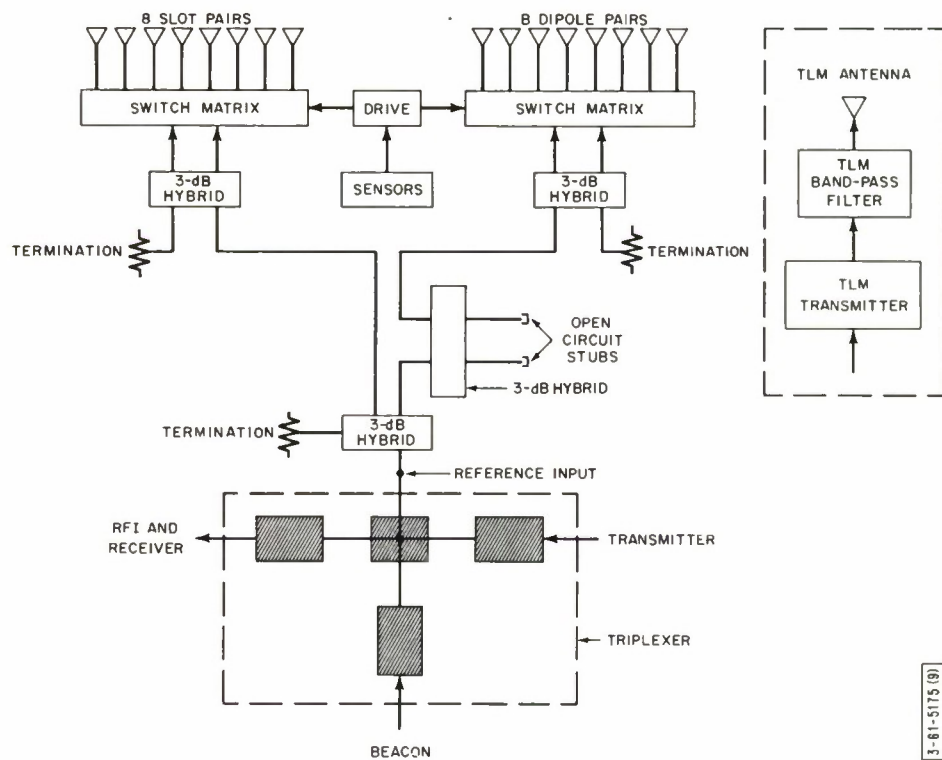


Fig. 2. Antenna system of satellite.

the required right-hand circular polarization. It was planned that the satellite be located in synchronous equatorial orbit and that it spin about the cylinder axis oriented perpendicular to the orbit plane.

Within the satellite is a transponder whose function is to receive signals at a frequency  $f_R$  in the neighborhood of 300 MHz at levels as low as  $-120$  dBm, translate them to a frequency  $f_T$  50 MHz less, and transmit them at a power level  $P_T$  of 100 watts. Also, the satellite generates a beacon signal with a frequency  $f_B$  5 MHz above  $f_T$  and a power level  $P_B$  of 4 watts. In addition, the satellite carries a radiometer instrument to monitor RFI signals throughout a band  $f_{RFI}$  extending from 40 to 65 MHz above  $f_T$  at levels down to  $-120$  dBm. It was planned that the slot-dipole antenna system be used for the radiation and reception of these signals simultaneously. In order that the signals be handled in common, they are combined by a triplexer with passbands at frequencies  $f_T$ ,  $f_B$ , and  $f_{RFI}$ . Also carried aboard the satellite is a telemetry system whereby a signal of frequency  $f_L$  12.35 MHz below  $f_T$  and a power level of 1 watt, is radiated from a monopole mounted centrally on the end of the satellite. The parameters of the RF signals used in the satellite are summarized in Table 1. A layout of the RF system is shown in Fig. 2.

The satellite was designed to produce a beam collimated so that any user on the earth may benefit by an increase in antenna gain. Hence it was necessary to develop a system of antenna switching to maintain the same beam direction as the satellite spun on its axis. This then required that a UHF switch be located in the RF circuit between the triplexer and antenna system. This switch matrix would enable any one of a number of radiation beams which are equally spaced around the satellite to be turned on. It is hence in nature a digital system, and compared with systems that rotate the beam in a continuous mode, has the advantage of requiring less elaborate apparatus, providing the number of beams is sufficiently small. It has the disadvantage that the peak of the beam that is "on" will not be aimed at the center of the earth during most of the switch cycle. The decrease in gain, as a result of this "stepping" characteristic, approaches zero as the number of beams  $n$  becomes infinitely large, and it shall be shown later that the decrease in gain is acceptably small for values of  $n$  that are not too large.

In making the initial decisions concerning the switch configuration, a number of points were considered:

- (a) The number of antenna element pairs to turn on simultaneously: 1 alone or 2, 3 or more adjacent pairs.
- (b) The relative amplitudes of the excitations to provide optimum beamwidth and gain.
- (c) The phasing of the element excitations to aim the beams in the desired directions; with the same elements being excited, more than one beam may be obtained by use of more than one set of phases and hence the switch may serve to switch phases as well as amplitudes.
- (d) The number of beams  $n$ ; in order that the beams be distributed around the satellite in intervals compatible with the antenna arrangement, reasonable values for  $n$  are 4, 8, 12 or 16.

In normal operation, as the satellite spins in its orbit, each one of the  $n$  beams will be turned on in sequence as it sweeps past the earth. An observer on the earth can be located anywhere within a range of angles relative to the pattern of the beam that is on and it is in this range that one strives for maximum pattern gain. Hence, the extent of this range of angles, which depends on the value of  $n$ , determines the pattern gain available throughout the range. The choice of switch configuration is therefore based partly on how closely it provides the optimum



pattern and thus the antenna patterns assume importance in this regard. The study of different switch configurations and antenna patterns applicable to the LES-6 satellite necessarily occupied the initial phase of this program. However, the first purpose of this report is to give a full description of the adopted switch design, its characteristics, development, and testing. Therefore, we postpone to Sec. XII the discussion of pattern calculations and measurements, alternative configurations and the rationale for the chosen configuration.

Any configuration for a switch matrix consists of

- (a) A network of SPST units each of which has either of two states, ON where the RF signal is transmitted with ideally no loss, and OFF where ideally no signal is transmitted.
- (b) Runs of transmission lines where the change in signal phases is significant.
- (c) Suitable power dividers.

For this satellite, the switch must be a nine-port device, one port to accept the signal coming in on a single coaxial line and eight ports that connect to the eight antenna element sets (one slot pair, one dipole pair or both).

The basic element of the switch was chosen to be, because of its good ON and OFF RF characteristics, the PIN diode, which consists of a silicon semiconductor chip of three layers, the P-, I-, and N-layers. It has the desirable characteristics of low bias power requirements and small size. The switch was constructed in a strip transmission line for the convenience it provides for laying out microwave networks. Section 11 describes the switch hardware in detail.

Switch development is dealt with in Sec. III. Its construction procedure is detailed and the RF characteristics, i.e., VSWR, insertion loss and isolation, are summarized. The intent was to strive for the best performance at the transmit frequency due to the power limitation of the satellite. The characteristics throughout the RFI band, though important, were considered secondary.

A discussion of the performance of various switch configurations including SPST and SP2T switches is given in Sec. IV.

Each diode in the switch matrix is required to handle tens of watts of RF power and due to resistive losses, its temperature will stabilize significantly above the ambient temperature. Because diode temperature affects its reliability, various methods to keep the temperature low were examined and one technique implemented. The temperatures in the operating switch matrix in a vacuum were then measured (see Sec. V).

In another experiment in a vacuum, signs of multipactor were sought (Sec. VI). This is a type of electrical breakdown occurring between two surfaces with an RF electric field between them. It arises with certain resonant conditions of frequency and field amplitude, and the nature and configuration of the surface. It is not associated with the presence of a gas in the region insofar as its normal mechanism of operation is concerned.

The two signals at frequencies  $f_T$  and  $f_B$  pass through each diode simultaneously, and due to the nonlinear character of the diode, intermodulation products will be generated in the RFI and transponder receiver bands. It is important that their amplitudes be sufficiently low so that the sensitivities of receiving instruments are not degraded. In addition, each time a diode is switched, a brief burst of noise is generated together with an increase in the intermodulation amplitude. Ensuing from a study of these problems using the SPST and SP2T switches, specific diode requirements were established and a diode with improved characteristics was fabricated.

Extensive measurements of intermodulation product and switching noise amplitudes of each switch matrix were then carried out (Secs. VII and VIII).

The noise figures of some diodes and a complete switch matrix were determined (Sec. IX). It was noted that the noise figure of a diode increases when its leakage current increases. This provided a criterion on the acceptability of the diode for the reliability testing.

The possible effects on diode performance in a radiation environment existing outside the earth's atmosphere were examined and are described in Sec. X.

A study of diode reliability was carried out and a screening procedure set up. Each switch matrix was subjected to environmental tests including mechanical shock, vibration, and thermal cycle to qualify it for the satellite. These studies are described in Sec. XI.

It was decided that it would be more desirable to use two switches rather than one in the satellite for a number of reasons. The single output of the triplexer would be divided to provide two equal signals for each of the switches. One switch would connect to the slots and the other to the dipoles (Fig. 2). Each switch then needs to handle only half the power, with several consequences, namely, the diode temperature increase is reduced and the intermodulation product and switching noise amplitudes are lessened. In addition, a failure in one of the switches affects only one antenna polarization rather than the whole antenna pattern. In the discussion in Sec. XII, it is indicated that there is a specific length for the lines joining the switch to the antenna elements to provide the optimum pattern. These lengths may differ for the slots and the dipoles and if this is so, one switch cannot be used to serve both antenna element types with maximum efficiency. Also the very fact that the slot and dipole feed systems are essentially isolated facilitates their development.

Concern arose about a possible failure in the switching logic in which the antenna beam would not be aimed in the correct direction. To safeguard against this mishap, a back-up mode of operation was provided which enables the satellite to be commanded to an omnidirectional pattern. This is accomplished by applying a unique set of biases to the switch diodes. Throughout this report, characteristics of the switch matrix in this additional mode of operation are included along with the normal mode. The two modes of operation shall be designated the Scan Mode and the Omni-Mode.

A summary of the characteristics of the two switches used in the LES-6 satellite is given in Appendix A. Other final data may be found in Figs. 37, 38, and 39. A photograph of a switch is shown in Fig. 35 and the two switches can be seen mounted at the center of the satellite platform in Fig. 3. The completed satellite which supports the platform at its equator is pictured in Fig. 4.

Each section of this report was written with the view to keeping it distinct and independent. The reader if interested in one aspect of the switch should be able to read the relevant section with a minimum of cross reference to other sections except Sec. II, of course, which describes the switch circuit and components. A condensed version of this report has been published in another technical report for the reader who is interested only in a general picture of the switch performance.<sup>1</sup>

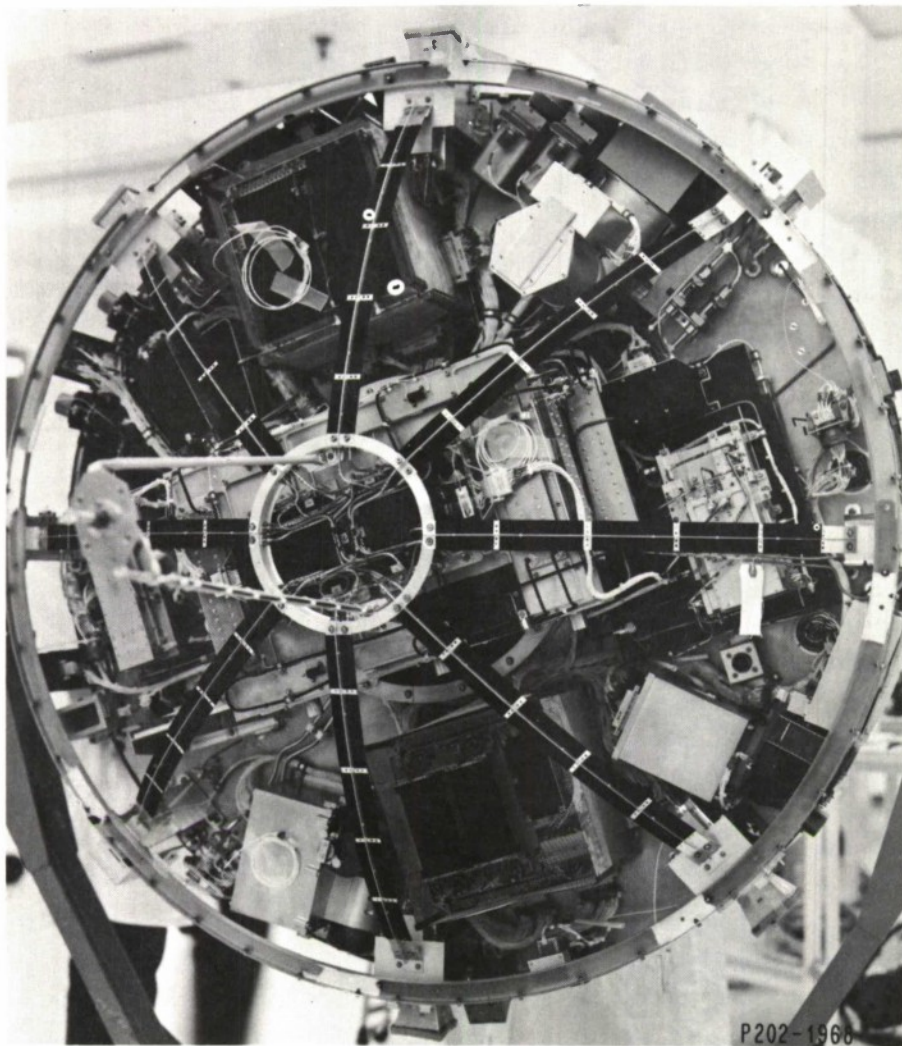
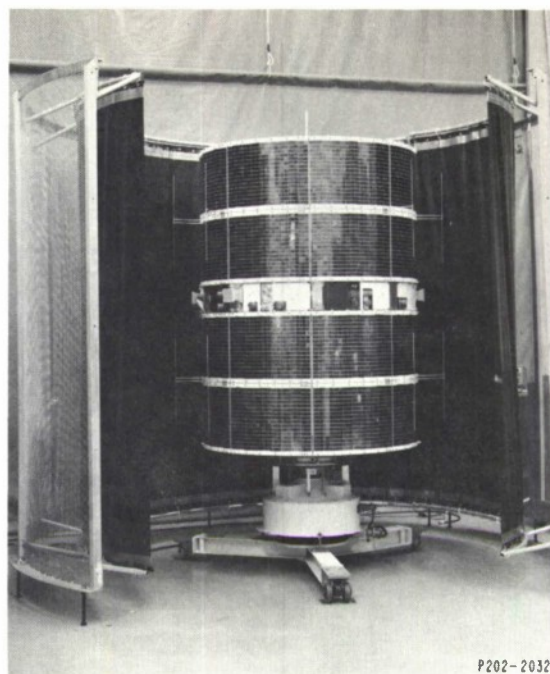


Fig. 3. Satellite platform containing electronic instrumentation; switches are mounted on triplexer in central location and can be seen inside aluminum ring.



Fig. 4. Completed satellite shortly before launch.



## II. SWITCH CIRCUIT AND ITS COMPONENTS

### A. Switch Matrix Circuit and Basic Operation

It is possible to obtain antenna patterns of different beam widths and gains by exciting various numbers of adjacent elements on the satellite with signals of various amplitudes and phases. For each pattern, the spacing of the antenna beams around the satellite has an optimum value. This optimum value in turn determines the number of satellite beams needed. In each case, the switch matrix design required to provide the appropriate amplitudes, phases, and number of beams has a specific complexity and loss. By taking all these points into account, choices can be made on the number of beams  $n$ , the number of antennas excited simultaneously, and the switch configuration. A full account of this study is given in Sec. XII.

The plan that seemed to be the best choice was to generate  $n = 16$  beams where two adjacent antennas at a time are excited. The pointing directions of these beams relative to the antenna positions are shown in Fig. 90(g) on page 102. (The antenna elements are numbered consecutively, and beams lettered consecutively with the letter I omitted.) The beam directions, that is, the directions central in the coverage angles of the beams, are equally spaced around the satellite with the antennas lying midway between them.

To obtain beam A from antennas 1 and 2, there must be a difference of phase of the signals at the two antennas, which may be rendered by the addition of a length of line to antenna 1. Likewise, beam B comes about by reversing the phases of the two antenna signals. This implies that a 2P2T switch section is needed. For any beam, one even-numbered and one odd-numbered antenna is on. Hence, two SP4T sections are needed, one to select one of the four odd-numbered antennas, and one to select one of the even-numbered.

Under these considerations, the switch matrix takes the configuration shown in Fig. 5(a). The input signal is divided by a hybrid into two equal parts. One signal leads in phase by  $90^\circ$ , so that an additional length of line must be added to reduce this phase lead to a suitable value.

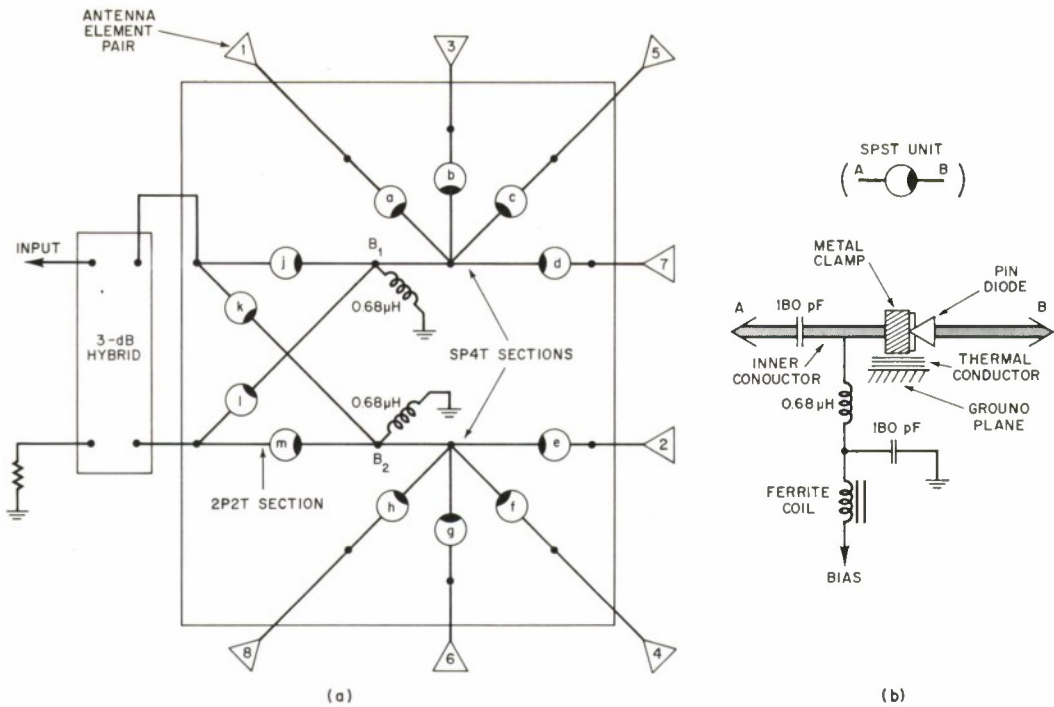


Fig. 5. (a) Switch matrix configuration chosen for satellite. (b) Circuit of 12 SPST units in switch matrix.

The two signals are then fed into the two input ports of a 2P2T section. The two outputs are tied to the inputs of two SP4T sections and their output ports in turn are connected to the eight antennas.

The 2P2T and SP4T sections consist of 12 SPST units shown in Fig. 5(b). They are labeled a through d and e through h in the two SP4T sections and j through m in the 2P2T section. If the states of these units are represented by waveforms which swing up for the OFF state and down for the ON state, they take the shape shown in Fig. 6. Any beam can be checked by determining the states shown in the figure and tracing the signal through the circuit in Fig. 5(a). For example, for beam A, SPST units a, e, k and l are ON. This switches ON antennas 1 and 2. The additional line length ties to antenna 2 and the beam is shifted to the side of antenna 1.

In the initial phase of the program, a power divider rather than a hybrid was developed and tested. It was designed to give an equal power division with the correct phase difference over the frequency range involved in the satellite RF system while maintaining a 50-ohm characteristic impedance. It was found on testing with the antenna system that because the antenna impedance varied significantly with frequency, the

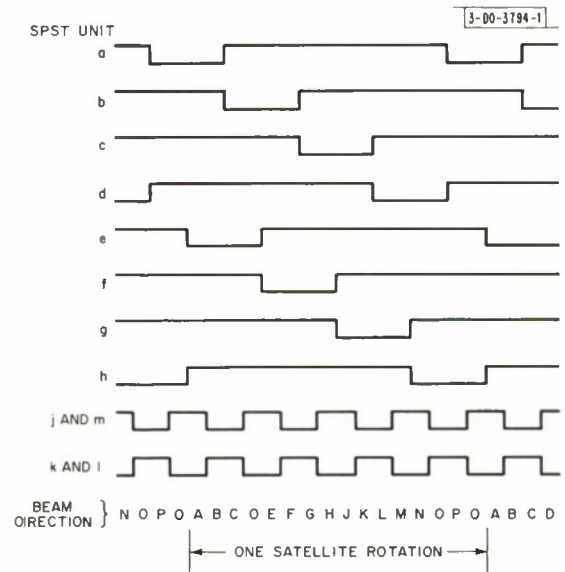


Fig. 6. Voltage waveforms applied to SPST units of switch matrix; positive swing turns unit OFF, negative swing turns it ON.

parameters of the two signals that excited the two antennas could deviate radically from the desired values and the antenna patterns were unacceptable over much of the frequency band. The hybrid power division is not affected in this way. In addition, the hybrid has the advantage that the phases of the two excitations are readily adjustable by the selection of the two lengths of transmission line tying the hybrid to the switch matrix proper.

## B. SPST Unit

The switch matrix and other switch configurations will consist of SPST units, which then can be considered as building blocks. Therefore, to facilitate the discussion of the complete switch and its performance, the structure of the SPST unit is first described followed by a detailed description of the components that make up the switch.

The diode must be placed in the transmission line so that it will alter the RF signal in the desired way. There are two choices, namely, to put the diode in series with the inner conductor or in shunt from the inner to outer conductor. This latter choice was ruled out since in one of its states the diodes will short the transmission line and if it is not to affect the operation of the switch section (such as the SP4T section), it must be placed a quarter wavelength from the junction. This would consequently produce a larger switch package and probably a narrow bandwidth. In the former choice, the diode may be, or rather should be if we are to have a circuit free of RF line stubs, placed at the common junction which results in a more compact unit.

To get the bias signals to the diodes with minimum effect on the RF signal, coils that have high impedance in the frequency band of interest are tied in shunt with the RF line to provide the route for the bias, as shown in Fig. 5(b). To block the bias from getting to other diodes, low impedance capacitors are placed in series with the RF line at each bias input point. An additional ferrite coil and capacitor are used in each bias line which further isolate the RF and bias signals, reduce RFI that might get to the diode via the bias line, and reduce the switching noise. These points will be discussed more fully later. Two coils like those tied to the RF line are sufficient to provide the bias return for the 12 diodes. They are shown in Fig. 5(a) at the points  $B_1$  and  $B_2$ .

The diodes are oriented, as the figure shows, so that the bias is applied to the cathode to allow better performance as we shall see later. Therefore, a negative voltage forward biases the diode, turning it ON, and a positive voltage turns it OFF.

The components that went into the switch can now be described in detail. All were chosen based on acceptability for the space environment.

## C. PIN Diode

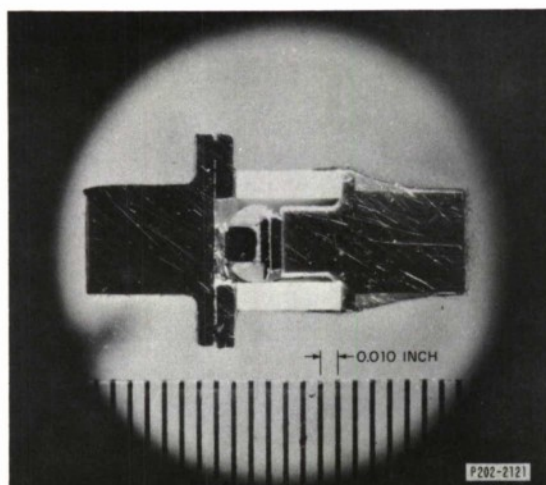
Of the devices that may be used to switch an RF signal, the PIN diode has advantages which make it the most attractive. These include such factors as its electrical characteristics, small size, good reliability and the low power needed to operate it. The qualities of these characteristics will become more evident as we proceed in the discussion.

The PIN diode<sup>2,3</sup> is a 3-layer semiconductor chip, usually silicon. The P- and N-layers are separated by an I- (intrinsic) layer which is lightly doped so that on forward bias it conducts and on reverse bias part of it, depending on the amount of bias, is swept free of charge carriers (called the depletion layer) and acts like an insulator. The state of the I-layer changes little with bias when it is sufficiently large (forward or reverse) and therefore the bias is not critical. On reverse bias, the presence of the I-layer raises the breakdown voltage substantially over the

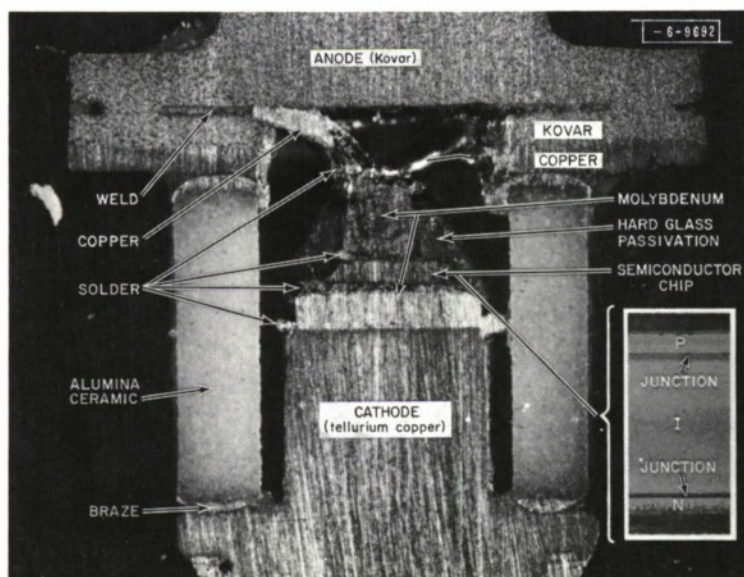


ordinary P-N junction and thus large biases enable the diode to handle large RF signals without the diode entering a too nonlinear region. Likewise, on forward bias, the diode can be biased by a DC current many times smaller than the RF current it carries, providing the period of the RF signal is small relative to the minority carrier lifetime.

Two PIN diodes of differing construction were considered in this program. One was of planar construction with an I-layer thickness of 0.002 inch and passivated using silicon dioxide. This was later discarded in favor of a diode of mesa construction having a 0.003-inch I-layer and passivated using a low-melting-point glass. The structure of this diode is shown in Figs. 7(a) and 7(b). It exhibited lower intermodulation product and switching noise amplitudes than the



(a)



(b)

Fig. 7. 3-mil PIN diode used on switch. (a) Cross section. (b) Detailed structure of diode. Metal parts are gold plated before soldering.

diode of the thinner I-layer (discussed in Secs. VII and VIII). A diode of one of these two types shall from now on be referred to as the 2-mil or 3-mil diode according to the I-layer thickness. In the course of the program, 4-mil diodes were also tested and were found to have similar or poorer performance than the 3-mil diodes and they were not readily available in quantity.

TABLE II CHARACTERISTICS OF PIN DIODES USED IN PROGRAM		
Characteristic	Diode I-Layer Thickness (inches)	
	0.002	0.003
Series resistance (ohms) ( $f = 500$ MHz, forward bias = 100 mA)	0.6 – 1.0	0.45 – 0.8
Total capacitance (pF) ( $f = 1$ MHz, reverse bias = 50 V)	0.3 – 0.5	0.65 – 0.9
Case capacitance (pF)	0.16	0.16
Reverse bias voltage for a current of 10 $\mu$ A (V)	200 – 500	800 – 1200
Minority carrier lifetime ( $\mu$ s)	1.5	2 – 4

The characteristics of the diodes ranged over the values given in Table II as determined by the manufacturer.

As indicated by the chart, the diode at the RF frequency is much like a resistor with a resistance of less than 1 ohm on forward bias. The DC resistance is about 16 ohms when the bias is 50 mA (corresponding to a voltage drop of 0.8 V). On reverse bias, the diode behaves like a capacitor with a capacitance of less than 1 pF. The dependence of this capacitance on bias is shown in Fig. 8. It is a plot of the diode junction elastance (reciprocal of the capacitance) of a typical 2- and 3-mil diode as a function of  $V - \phi$  as measured at 1 MHz, where  $\phi$  is the contact potential for doped silicon. For an abrupt P-N junction, such a plot is a straight line equivalent to a half-power power law. We see that the 3-mil diode has a constant capacitance above about 20 V, the "punch-through" voltage. On the other hand, the 2-mil diode showed no such characteristic. This difference is important in the investigation of intermodulation.

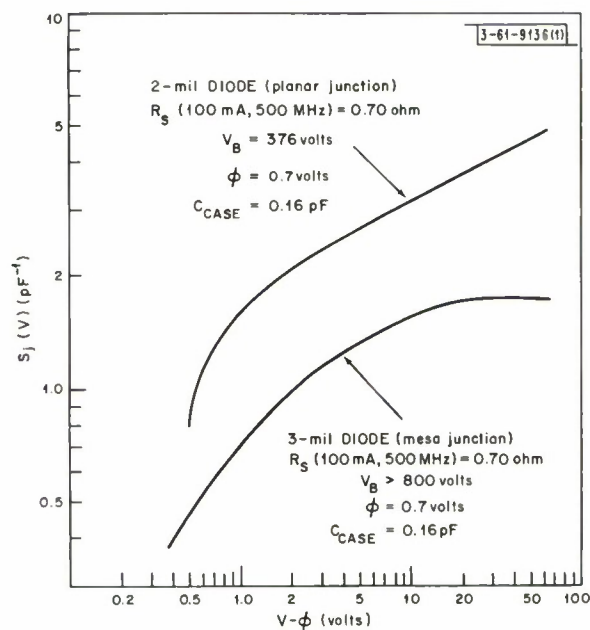
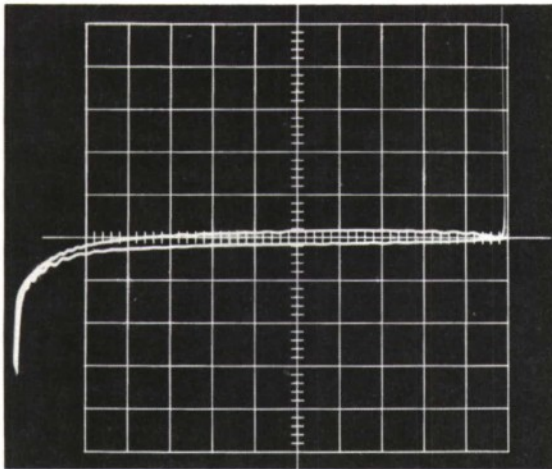


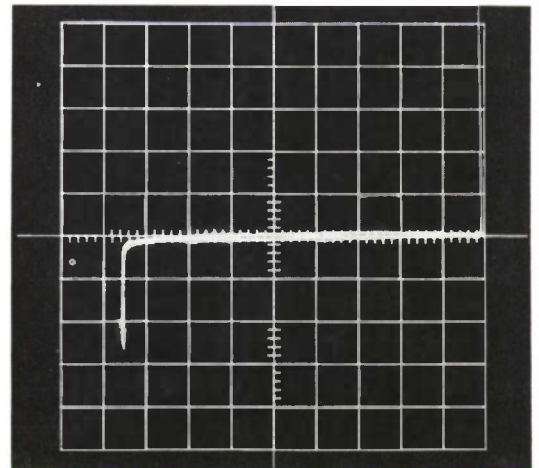
Fig. 8. Elastance of 2- and 3-mil diodes as measured at 1 MHz.

The leakage current is of the order of a microampere or less at normal operating levels. This leakage current is significant in that it gives an indication of the quality of the diode. If the diode were perfect, breakdown would occur in the bulk of the semiconductor. It is characterized



(a) Very good diode with high reverse-bias breakdown voltage.

(b) Semiconductor bulk breakdown over 800 V, a good value.



(c) Bulk breakdown low.

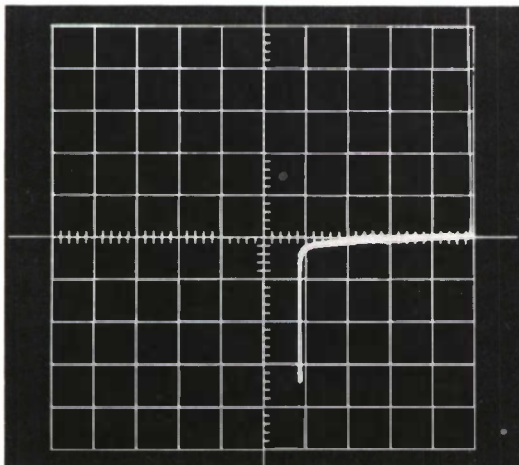


Fig. 9. V-I curve traces of a number of 3-mil diodes typifying different qualities. Origin is on center line at right side of grid. Horizontal scale is 100 V/major division, and vertical scale is 10  $\mu$ A/major division.



by an avalanche effect — a rapid increase in leakage current with a small increase in voltage beyond a certain level. Furthermore, this avalanche occurs at a voltage of 400 V per thousandths of an inch I-layer thickness. For the 3-mil diode, this value is 1200 V. If in actual observation, this avalanche occurs at a somewhat lower voltage, an ununiform I-layer is indicated. Either it is narrower in some locations, or some of the P- or N-type material has penetrated imperfections of the I-layer. A second quality to consider is the nature of the semiconductor surface. Impurities on the surface give rise to channels through which current can leak. This is characterized by a gradual increase in leakage current rather than by an abrupt change. A significant mode of failure for a diode is then too large a leakage current relative to the nominal values resulting from the imperfect semiconductor or contaminated surface. This is important in the problem of diode reliability (Sec. XI).

The V-I traces of some 3-mil diodes of varying quality are shown in Fig. 9. The origin is located at the center of the right edge of the grid. The horizontal scale is 100 V per major division and the vertical is  $10\mu\text{A}$  per major division.

Figure 9(a) shows about the best V-I characteristic observed in any of these diodes. The bulk breakdown occurs near 1200 V and a little surface impurity causes some rounding of the curve near breakdown. (The double trace is due to a small amount of pick-up of line voltage radiation into the system and can be ignored.) In Fig. 9(b) there is bulk breakdown at 850 V. Although this is not ideal, it is sufficiently high to be acceptable. This diode has a good surface quality. Figure 9(c) shows a low bulk breakdown indicating a poor quality semiconductor chip. The surface quality of the diodes of Figs. 9(d) and (e) is poor as indicated by the gradual increase in leakage current with bias. The diodes of Figs. 9(f) and (g) have good bulk characteristics and acceptable surface quality. Most of the diodes tested were like these. Both diodes in Figs. 9(h) and (i) have poor bulk and surface quality.

Nearly all diodes examined were quite acceptable. Only a few percent showed the poor characteristics exhibited in Figs. 9(c), (d), (e), (h), and (i) (see Table VII, Sec. XI-C).

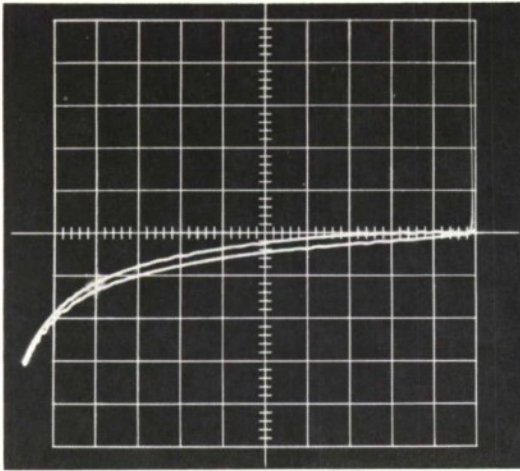
This description of PIN diodes, though brief, should be sufficient to aid in understanding the testing and observations described in the rest of the report.

#### D. Strip Transmission Line

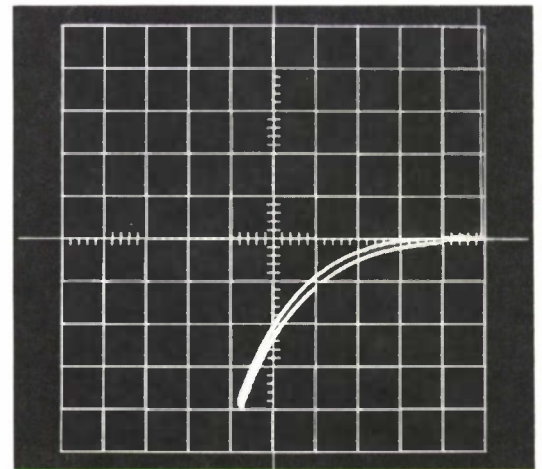
Strip transmission line or stripline provides a convenient technique for laying out microwave systems while furnishing a compact package. It is a double layer dielectric with the parallel outside surfaces covered by metal ground planes as shown in Fig. 10(a). The ground planes form the one conductor of the transmission line while the other conductor is a thin metal strip in an appropriate form laid out in the plane midway between the ground planes. The electric field then has the configuration shown in Fig. 10(b).

The material obtained for the stripline is  $\frac{1}{8}$ -inch thick rexolite board clad on both sides with copper 0.0027-inch thick. Rexolite is a cross-linked styrene copolymer with a dielectric constant of 2.53 and dissipation factor of 0.0004 at 250 MHz. Except for its brittle nature, it is well suited for the space environment.

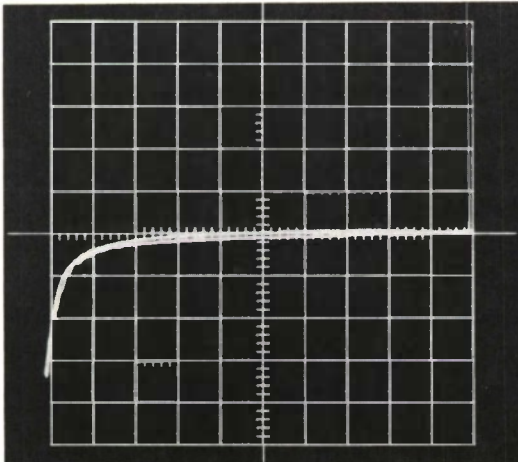
To make up a stripline with a circuit pattern, the circuit is first laid out on rubylith, a transparent plastic sheet with a colored coating. The coating is peeled off wherever appropriate, leaving the circuit outlined against the transparent backing. The sheet is then photographed and a negative made. One copper surface of the rexolite is sprayed with a photo resist and the negative placed on top. After making an exposure, the surface is etched with chromic acid. The copper



(d) Semiconductor surface contaminated.



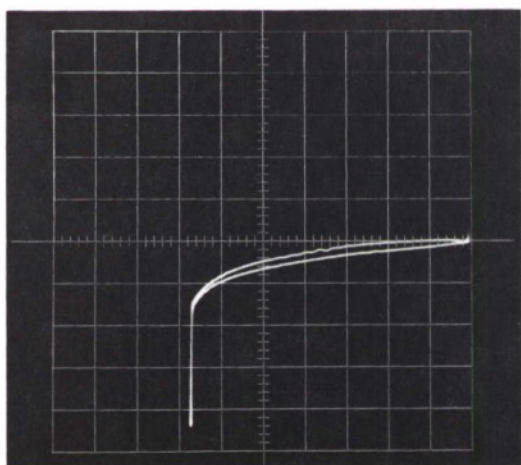
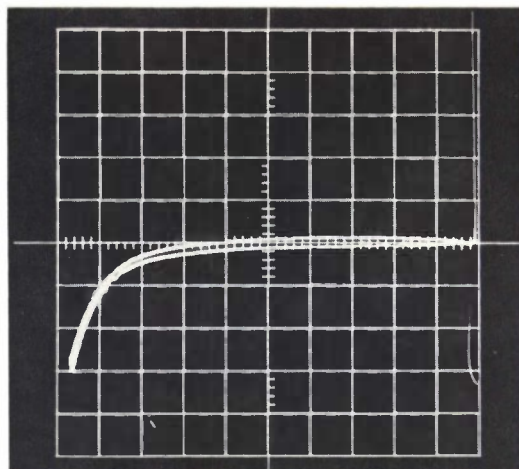
(e) Surface highly contaminated.



(f) Good characteristic.

Fig. 9. Continued.

(g) Acceptable.



(h) Bulk and surface only fair.  
This diode is unacceptable.

(i) Bulk and surface only fair.

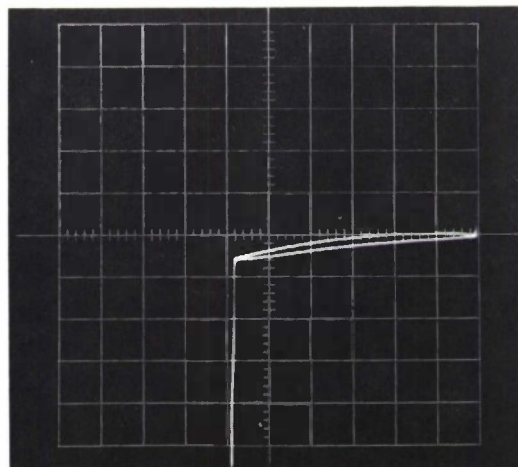


Fig. 9. Continued.



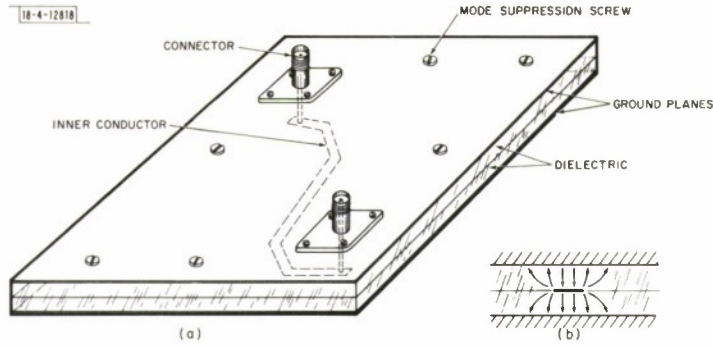


Fig. 10. (a) Layout of strip transmission line circuit containing no components other than connectors. (b) Electric field lines between stripline conductors.

clad is removed completely on the other side of the rexolite as well as on both sides of a second board. Both boards are then well cleaned and placed together to form a 1/4-inch thick sandwich. Gold-plated aluminum plates, 1/32-inch thick, are added to provide the ground planes. In addition to giving a stronger assembly, the plates have other advantages. For one, the circuit electrical characteristics are sensitive to any air gap next to the inner conductor (see further detail below) and this structure reduces the size of the gap. Also, one ground plane can be used to provide a path for heat dissipation (see Sec. V). (The two boards with the etched circuits that are used for the switch matrix are shown in Figs. 28 and 29 of Sec. III-C.)

In the normal circuit condition, the electric field lines for the RF signal extend from the inner conductor symmetrically to the two ground planes as shown in Fig. 10(b). If there are asymmetries in the circuit such as those due to imperfect construction or the connectors shown in the figure, a field may be set up which extends from one ground plane to the other and this field will propagate freely in any direction resulting in degradation of the circuit characteristics. A number of screws are then used to suppress this unwanted mode as well as to hold the rexolite boards close together.

An important design consideration is to relate the stripline characteristic impedance to the inner conductor width. Since the chosen characteristic impedance of the system is 50 ohms, the corresponding strip width must be found. The analysis of this problem is discussed in the following paragraphs. The theory is extracted from other published literature.<sup>4,5,6</sup>

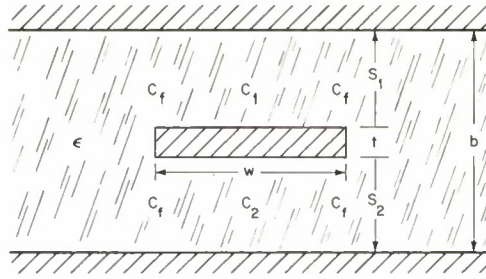
The characteristic impedance  $Z_0$  of any transmission line propagating a TEM wave is related to the capacitance  $C$  per unit length by the equation

$$Z_0 = \frac{\eta_0}{\sqrt{\frac{\epsilon}{\epsilon_0}} \frac{C}{\epsilon}} \quad (1)$$

where

$$\eta_0 = \sqrt{\frac{\mu_0}{\epsilon_0}} = 376.7 \text{ ohms} \quad (2)$$

Fig. 11. Stripline geometry showing dimension and capacitance parameters.



Suppose the strip has width  $w$ , thickness  $t$  and distances from the two ground planes of  $s_1$  and  $s_2$  as shown in Fig. 11. The separation of the ground planes is then

$$b = s_1 + s_2 + t \quad (3)$$

In the special case where

$$t = 0, \quad s_1 = s_2 = \frac{1}{2} b \quad (4)$$

$C/\epsilon$  is given by the exact relation

$$\frac{C}{\epsilon} = 4 \frac{K(\tanh \pi w / 2b)}{K(\operatorname{sech} \pi w / 2b)} \quad (5)$$

where  $K(\cdot)$  is the complete elliptical integral of the first kind. In the more general situation,  $C/\epsilon$  has to be approximated. The approximation differs if  $w/b$  is greater or less than 0.35 due to the comparative accuracy.

If

$$\frac{w}{b} > 0.35 \quad (6)$$

the capacitance can be viewed as consisting of several shunt components:  $C_1$  and  $C_2$  are the capacitances between parallel plates and  $C_f$  is a capacitance due to a fringing in the electric field at a corner of the inner conductor. Thus, approximately (see Fig. 11),

$$\frac{C}{\epsilon} = \frac{C_1}{\epsilon} + \frac{C_2}{\epsilon} + 4 \frac{C_f}{\epsilon} \quad (7)$$

$$\frac{C_1}{\epsilon} = \frac{w}{s_1}, \quad \frac{C_2}{\epsilon} = \frac{w}{s_2} \quad (8)$$

and

$$\frac{C_f}{\epsilon} = \frac{1}{\pi} [(r+1) \ln(r+1) - (r-1) \ln(r-1)] \quad (9)$$

where

$$r = \frac{b}{b-t} \quad (10)$$

Let us add a correction factor  $\gamma$  to improve the accuracy of the formula. The formula is then

$$\frac{C}{\epsilon} = \left\{ w \left( \frac{1}{s_1} + \frac{1}{s_2} \right) + \frac{4}{\pi} [(r+1) \ln(r+1) - (r-1) \ln(r-1)] \right\} \gamma \quad (11)$$

If  $w = 0.182$  inch,  $s_1 = s_2 = 0.126$  inch and  $t = 0$ , Eq. (5) gives

$$\frac{C}{\epsilon} = 4.736 \quad (12)$$

and Eq. (11) gives

$$\frac{C}{\epsilon} = 4.654\gamma \quad (13)$$

The value of  $\gamma$  is then 1.0175 indicating good accuracy. (For  $\epsilon/\epsilon_0 = 2.53$ , Eq. (1) gives an impedance of 50 ohms.)

In the actual stripline  $s_1 = 0.120$  inch,  $s_2 = 0.132$  inch and  $t = 0.0027$  inch. The problem is to determine  $w$  so that  $Z_0 = 50$  ohms. Although the value of  $\epsilon/\epsilon_0$  for rexolite is 2.53, some measurements of stripline circuits indicated an effective  $\epsilon/\epsilon_0$  of about 2.47. These measurements and the discrepancy are discussed below. For the following calculations we take

$$\frac{\epsilon}{\epsilon_0} = 2.47 \quad (14)$$

Then, Eq. (1) requires that

$$\frac{C}{\epsilon} = 4.794 \quad (15)$$

for  $Z_0 = 50$  ohms, and Eq. (11) gives

$$w = 0.1799 \text{ inch} \quad (16)$$

If

$$\frac{w}{b} < 0.35 \quad (17)$$

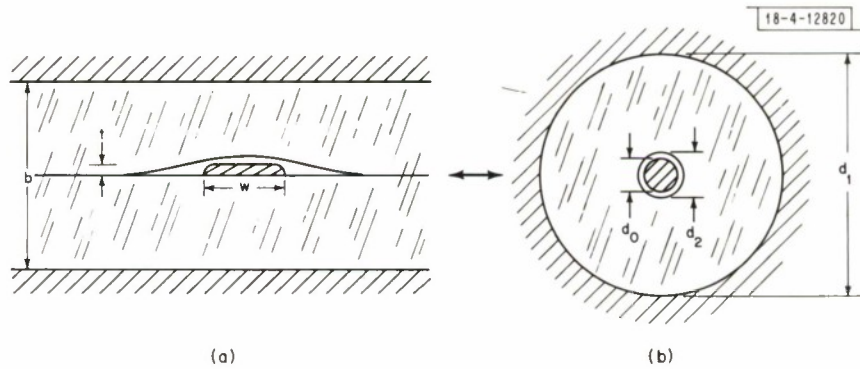


Fig. 12. (a) Stripline with gap between inner conductor and dielectric.  
(b) Equivalent coaxial line.

the stripline can be equated to a coaxial line as shown in Fig. 12. For coaxial line,

$$\frac{C}{\epsilon} = \frac{2\pi}{\ln(d_1/d_0)} \gamma \quad (18)$$

As before, a correction factor  $\gamma$  has been included. The outer diameter is simply

$$d_1 = \frac{4}{\pi} b \quad (19)$$

On the other hand, the inner diameter  $d_0$  does not have a simple form. [It is given by Eq. (8) in Sec. 5.11 of Ref. 7, where  $d' = w$  and  $d'' = t$ .] For  $w \gg t$



$$d_o \approx \frac{w}{2} + \frac{t}{2\pi} (1 + \ln 4\pi \frac{w}{t}) \quad . \quad (20)$$

In the switch, a line of width  $w = 0.032$  inch is used. For this width, the factor  $\gamma$  can be estimated by comparing these formulas with the accurate value given by Eq. (5) for  $t = 0$  and  $b = 0.252$  inch. It evaluates to 0.9406. For  $t = 0.0027$  inch, Eq. (18) gives  $C/\epsilon = 2.067$  and Eq. (1) gives  $Z_o = 116.0$  ohms.

The formulas for attenuation in stripline are rather complex and not sufficiently important to reproduce here. However, they are given in several references.<sup>4,5,8</sup> The attenuation consists of two parts, dielectric loss and conductor loss. Using the values for the specific stripline considered here, we obtain a total loss of 0.0028 dB/inch for the 50-ohm line and 0.0057 dB/inch for the 116-ohm line at 250 MHz. These values will contribute very little to the total loss of the switch matrix.

To determine the effective dielectric constant of the stripline, two pieces of uniform line were constructed, each containing simply a straight inner conductor of 0.176-inch width. Between connectors, the pieces were about  $3\frac{3}{8}$  and  $16\frac{1}{4}$  inches long, and showed VSWR's of 1.05 or less at 250 MHz.

Three types of measurements were made, all at 250 MHz. The first consisted of measuring the phase of the reflection coefficient of the transmission lines terminated in short circuits. With this approach, the effective dielectric constant is

$$\frac{\epsilon_e}{\epsilon_o} = \left[ \frac{\lambda_o(\varphi_1 - \varphi_2)}{(L_2 - L_1)(720^\circ)} \right]^2 \quad . \quad (21)$$

$\varphi_1 - \varphi_2$  is the difference of the reflection coefficient phases which measured  $309^\circ$  in this experiment.  $L_2 - L_1$ , the difference in length between the two pieces, is 12.86 inches.  $\lambda_o$  is the free space wavelength, 47.21 inches. Therefore, the calculated value of  $\epsilon/\epsilon_o$  is 2.484.

The second measurement required reckoning the phase by the use of probes at two points along the longer stripline piece terminated in a matched load. The probes had no apparent effect on the characteristics and therefore the measurements should be accurate. The dielectric constant is given by Eq. (21) again, but with the factor  $720^\circ$  replaced by  $360^\circ$ . Now  $\varphi_1 - \varphi_2$  measured  $143.9^\circ$  and the separation of the probed points  $L_2 - L_1 = 12.019$  inches. Therefore, the value 2.465 is obtained for  $\epsilon/\epsilon_o$ .

The third technique was an observation of the characteristic impedance of the stripline using a time domain reflectometer. This indicated a value of 51 ohms. Equation (11) shows that the capacitance for the dimensions of the piece should be  $C/\epsilon = 4.737$ . Equation (1) then gives 2.432 for  $\epsilon/\epsilon_o$ . The accuracy of this measurement is not good, and no importance should be placed on the result, other than that the characteristic impedance was not the 50 ohms that would have existed if  $\epsilon/\epsilon_o = 2.53$ .

One can assume the value of  $\epsilon/\epsilon_o$  to be about 2.47, less than the dielectric constant for rexolite, 2.53. The probable reason for the discrepancy is the presence of a gap between one side of the inner conductor and the rexolite. To illustrate, take the example where  $s_1 = 0.120$  inch,  $s_2 = 0.132$  inch,  $t = 0.0027$  inch, and  $w = 0.1799$  inch for a 50-ohm impedance. Considering the equivalent coaxial line, the dimensions are, by Eq. (19) and (20),  $d_o = 0.0933$  inch and  $d_1 = 0.3243$  inch. Suppose there is a gap of 0.001 inch around the inner conductor where the dielectric constant is 1.00 and the remaining space is rexolite with a dielectric constant of 2.53 as shown in Fig. 12. The diameter of the gap is then  $d_2 = 0.0953$  inch. The equivalent dielectric constant is given by

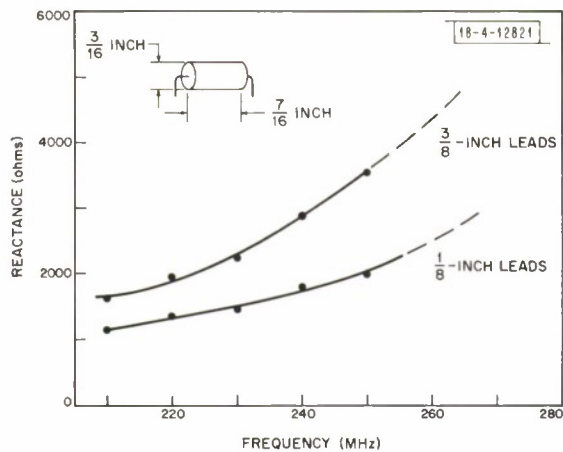


Fig. 13. 0.68- $\mu$ H coils used on switches and their measured reactances.

Fig. 14. Ferrite coils used on switches, and series resistance and reactances as provided by the manufacturer.

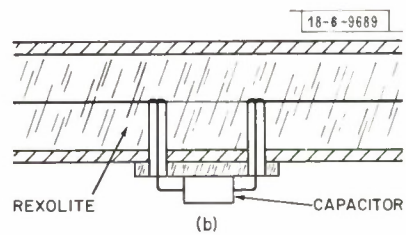
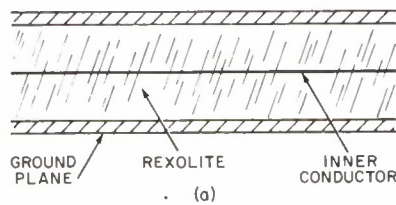
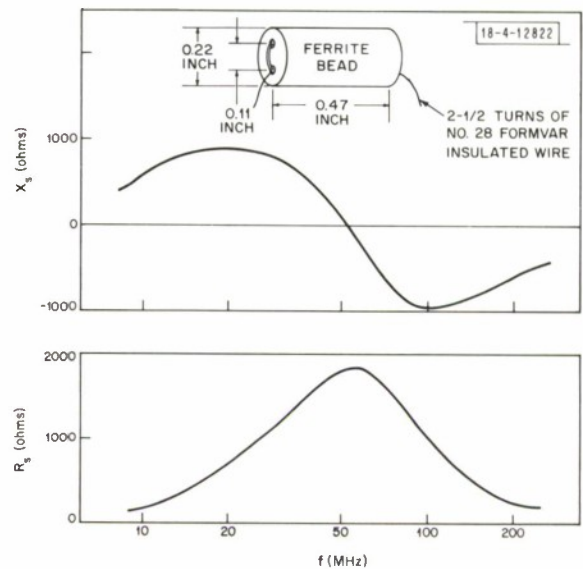


Fig. 15. Two hardware items which showed negligible difference in VSWR. (a) Stripline with single straight inner conductor. (b) Stripline with capacitor in series with single straight inner conductor.

$$\frac{\epsilon_e}{\epsilon_o} = \frac{\log(d_1/d_o)}{\frac{\log(d_2/d_o)}{1.00} + \frac{\log(d_1/d_2)}{2.53}} \quad (22)$$

Hence,

$$\frac{\epsilon_e}{\epsilon_o} = 2.465 \quad (23)$$

Thus, we see that the presence of a 0.001-inch gap reduces the effective dielectric constant from 2.53 to 2.465. In the case of the stripline, the effect may be even more pronounced because of the large electric field along the edge of the inner conductor. It is evident that in assembling a stripline circuit, the two boards should be in good contact.

In summary, the value of  $\epsilon/\epsilon_o$  is taken as 2.47. For a strip width of 0.180 inch,  $Z_o = 50$  ohms, and a width of 0.032 inch,  $Z_o = 116$  ohms. The wavelength in the stripline is then

$$\lambda_g = \frac{7510}{f} \text{ inches} \quad (24)$$

where  $f$  is the frequency in MHz. (The stripline wavelength is 30.04 inches at 250 MHz and 25.03 inches at 300 MHz.)

#### E. 0.68- $\mu$ H Coil

Coils, obtained commercially, are connected to the RF line in the switch and provide the path for the bias signal to the diode. They may be considered as helical transmission lines which have a nominal inductance of 0.68  $\mu$ H at "zero" frequency. They are nearly parallel self-resonant in the operating frequency range and therefore have high impedance. Figure 13 is a plot of the reactance of two such coils (with a sketch of one), one with  $\frac{1}{8}$ -inch leads and the other with  $\frac{3}{8}$ -inch leads. The highest frequency of the measurement is only 250 MHz because of the limitation of the instrumentation. The reactance depends on the lead length; the longer leads have the effect of lowering the resonant frequency. In the switch, the leads are about  $\frac{1}{4}$  to  $\frac{3}{8}$  inch. It can be assumed then that the reactance will remain above 2000 ohms in the 250- to 300-MHz range, a sufficiently high value to have little effect on the RF signal.

The coils also have a resistive component. In all the measurements, the equivalent parallel resistance proved to be over 50,000 ohms.

#### F. Ferrite Coil

The ferrite coils help reduce the switching noise and minimize RF interference coming from the switching logic and the bias leads to the switch. Each coil consists of  $2\frac{1}{2}$  loops of wire on a ferrite bead as shown in Fig. 14. The resistive and reactive components are plotted in Fig. 14 over a frequency band. It is evident that these coils effectively attenuate RF signals over a wide frequency range.

#### G. Capacitor

The capacitors located in the RF lines as well as the bias lines are  $\frac{1}{4}$  inch square and are obtained commercially. The nominal capacitance is 180 pF which corresponds to a reactance of -3.5 ohms at 250 MHz. The leads on the capacitor, which are about  $\frac{1}{4}$  inch long when used on the switch, shift this reactance closer to 0. The capacitors of the SP4T sections of the switch are mounted on the outside of one of the ground planes as shown in Fig. 15(b). Measurements of



a stripline with a single straight inner conductor interrupted by one of the capacitors showed no observable difference in characteristics from the uninterrupted line (Fig. 15).

## H. Boron Nitride

Slabs of boron nitride are also used on the switch to conduct the heat away from the diodes to the ground plane. Their presence in the RF field affects the circuit characteristics. At 250 MHz, boron nitride has a dielectric constant of 4.4 and a dissipation factor of 0.0007. The thermal conductivity of boron nitride is 0.4 to 0.6 watt/cm/°C at 100°C, which is close to that of steel. It is not isotropic in the form obtained commercially which accounts for the range in the thermal conductivity value.

## I. Coaxial Connector

The connectors used on the switch are of the OSM type and have the outline shown in Fig. 16. The flange is mounted on the surface of the ground plane with bolts passing through

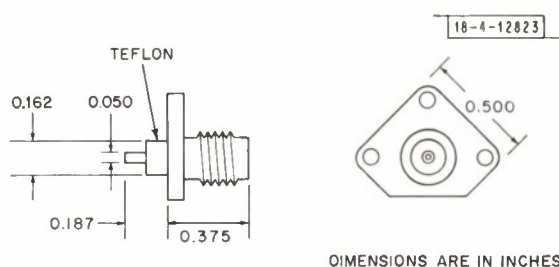


Fig. 16. Configuration of OSM connectors used on switches. Metal inner and outer conductors are gold plated.

the stripline sandwich. The inner conductor projects through a hole in the rexolite to the circuit where it is soldered. This layout exhibits a VSWR of no more than 1.05.

## J. 3-dB Hybrid and Joining Cables

The 3-dB hybrid used in conjunction with each switch is described in a separate report.<sup>9</sup> The connecting cables are semi-rigid coaxial which can be bent to any shape. The conductors of the cable are solid copper and their outer diameters are 0.0359 and 0.141 inch. The inner conductor is silver plated. The dielectric used is teflon. The characteristic impedance is 50 ohms and the wavelength of a signal on this cable is given by

$$\lambda_g = \frac{8190}{f} \text{ inches} \quad (25)$$

where  $f$  is the frequency in MHz.

In the satellite, the two cables joining the hybrid and the dipole switch are  $13\frac{1}{2}$  and  $16\frac{5}{8}$  inches long. The difference in length,  $3\frac{1}{8}$  inches, corresponds to a phase difference of  $34^\circ$  at 250 MHz and  $41^\circ$  at 300 MHz. The hybrid output signals have a phase difference of approximately  $90^\circ$  throughout the band. Hence the difference in phase of the signals at the output ports of the switch that are ON are  $56^\circ$  and  $49^\circ$  at the two respective frequencies. Similarly, the two cables connected to the switch tied to the slots are  $13\frac{1}{8}$  and  $17\frac{1}{2}$  inches long. Therefore, the phase differences of the two output signals are  $42^\circ$  and  $32^\circ$  at the two frequencies.

These coaxial line lengths were chosen to produce the best pointing directions for the radiation patterns at the transmit frequency (near 250 MHz). The pattern pointing directions at the receive frequency are satisfactory in spite of the apparent incorrect phasing.<sup>1,10</sup>

### III. DEVELOPMENT, CONSTRUCTION AND CHARACTERISTICS OF SWITCH MATRIX

#### A. Laying Out the Switch

To build up the circuit of the switch matrix, it was divided into two parts and laid out on two separate stripline boards. One board contained both SP4T sections in two X-shaped arrangements with a diode in each arm of the X, while the other had the 2P2T section laid out in a square where two opposite corners are the inputs. The two boards were then placed on top of each other so the remaining corners of the square were aligned with the centers of the X's. These points were joined by conductors to complete the circuit. This arrangement is pictured in Fig. 17.

The conducting lines of the circuit which are photoetched on the copper-clad rexolite included the lines for both the RF signal and the bias signal. The main RF lines were 0.180 inch wide for 50-ohm impedance. Lines of high impedance were also needed for matching purposes, and thus were kept at the narrowest width without being too fragile, namely 0.032 inch which corresponds to 116-ohm impedance. The bias lines were also 0.032 inch wide.

To choose the shape of bends in the 50-ohm line, characteristics of a simple square bend (like a corner of a picture frame) and a straight line of the same length on the same stripline sandwich were compared. The VSWR value of about 1.08 differed by no more than 0.02 in the 250 to 300 MHz range for the two lines.

A second consideration was the allowable proximity of two RF lines. Reference to charts given in the literature indicated that typical figures for the maximum coupling between two parallel 50-ohm lines are 23, 37 and 66 dB for separations of  $\frac{1}{16}$ ,  $\frac{1}{8}$ , and  $\frac{1}{4}$  inch, respectively. It seemed reasonably safe to separate RF lines by at least  $\frac{1}{4}$  inch and to place mode suppression screws at least  $\frac{3}{8}$  inch from the RF line.

With regard to the coils and capacitors, it appeared more expedient to bond them on one side of the ground plane on the outside, to bring their leads through holes drilled in the rexolite, and to solder them to the circuit. In addition to simplifying the machining, the gaps in the printed circuit provided paths for the bias lines. As shown in Fig. 15, the capacitors were supported on  $\frac{1}{16}$ -inch thick rexolite strips on the ground plane. On the other hand, the coils were bonded directly to the ground plane. Measurements of two hardware pieces having the two configurations shown in Fig. 15 showed no observable difference in VSWR.

The PIN diode needed special consideration because of the heat developed. A way had to be found to mount the diodes in order to efficiently drain off the heat inasmuch as the diode reliability depends on its operating temperature. Two major approaches were taken, the first depending on radiation and the second on conduction.

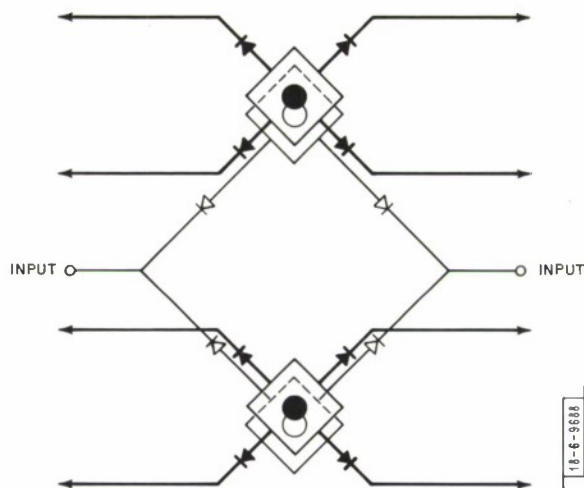


Fig. 17. Planned layout and alignment of 2P2T section (light lines) and SP4T sections (heavy lines).

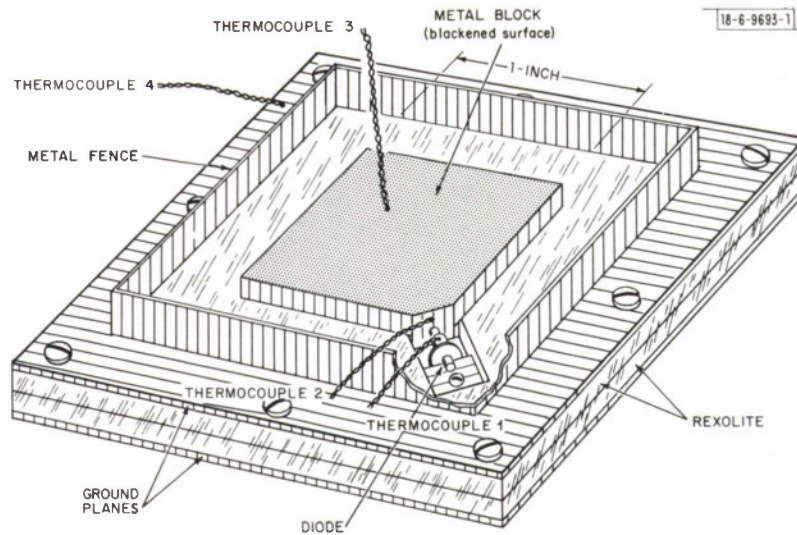


Fig. 18. SPST unit configuration tested for radiation of heat generated in diode.

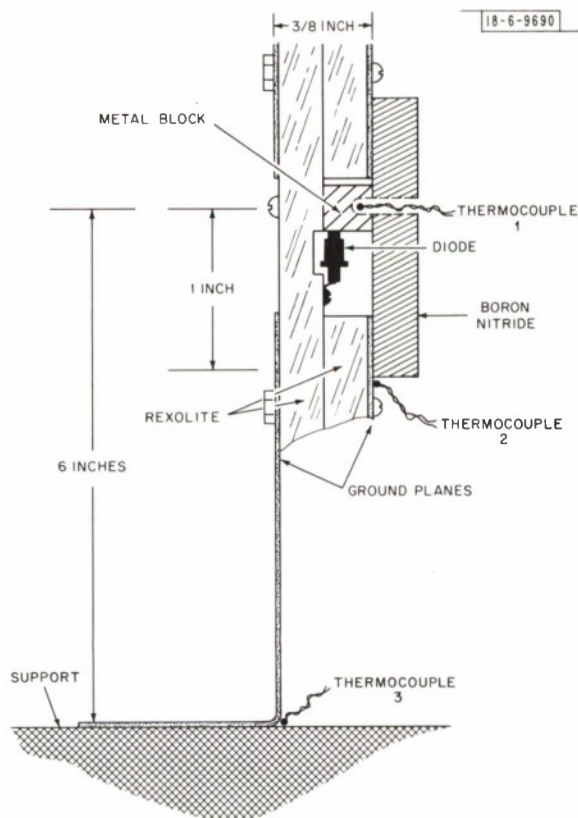


Fig. 19. Configuration adopted for satellite switches showing a unit mounted for thermol-vacuum measurements. Boron nitride is bonded to ground plane and diode metal block by a thin film of RTV.



The first approach is pictured in Fig. 18. The diode cathode pin is soldered in a 1-inch square metal block which in turn is soldered to the RF line. The metal block is painted black to give maximum heat emissivity. The measurements described in Sec. V-B showed poor efficiency in a vacuum, but we mention it since it was involved in some of the later measurements.

The second approach as pictured in Fig. 19, also has the diode cathode soldered in a small metal block which is soldered to the RF line. Now, the heat is conducted from the diode to the ground plane by a 1/8-inch-thick slab of boron nitride which is a good thermal conductor. This was the approach implemented in the final switch design. Aluminum covers were later added to shield the RF signal from interfering with other sensitive components in the satellite. The cover is constructed so that its central surface is raised 1/4 inch above the boron nitride in order that there be negligible effect on the VSWR.

Incidentally, the diode is constructed with good thermal bonding between the N layer and the one metal lug but not between the P layer and the other lug as is evident by the photographs in Fig. 7. Hence, the heat dissipation can be effective only by way of the cathode. In the X arrangement of Fig. 17, we desire that the diodes be located as close as convenient to the junction. Thus, the diode cathodes are faced away from the junction to facilitate the mounting of the diodes in their metal blocks. Furthermore, the biases can be conveniently brought to the cathodes, whereas there would be difficulty in bringing a separate bias signal to each anode.

Figures 20(a) and (b) show the final switch circuit layout although there were several stages in the development preceding this. Also shown is the labelling of the diodes and antennas to which the output ports are connected corresponding to Fig. 5(a).

The two sections were assembled together so that the components lay in the region between them. The spacer used to provide a frame to which the sections are bolted is 5/16-inch thick to allow sufficient clearance for the components, and fits along the edge of the assembly.

## B. Steps in Switch Development

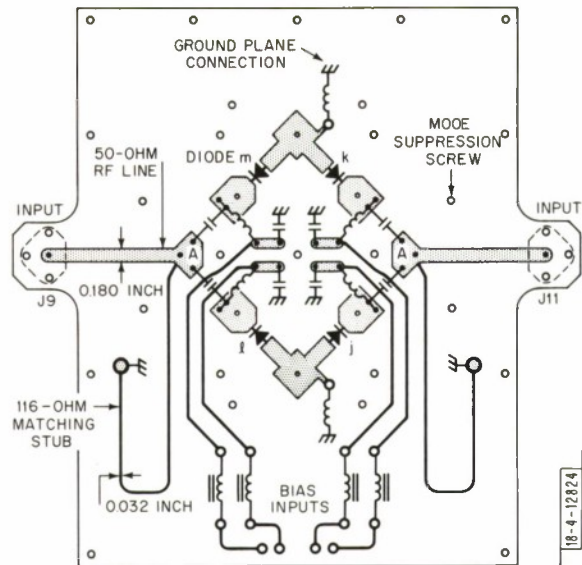
Figure 21 is the SP4T circuit, showing the form of the cutouts on the ground planes where the diodes are located and the outline of the boron nitride. Throughout the development, this form remained essentially unchanged and we need not discuss it further.

The 2P2T section, as shown in Fig. 22(a), had, in its early development, the diodes located near the junctions which connect to the SP4T sections. Furthermore, the 2P2T and SP4T sections were tied electrically by two short coaxial lines at the junction points.

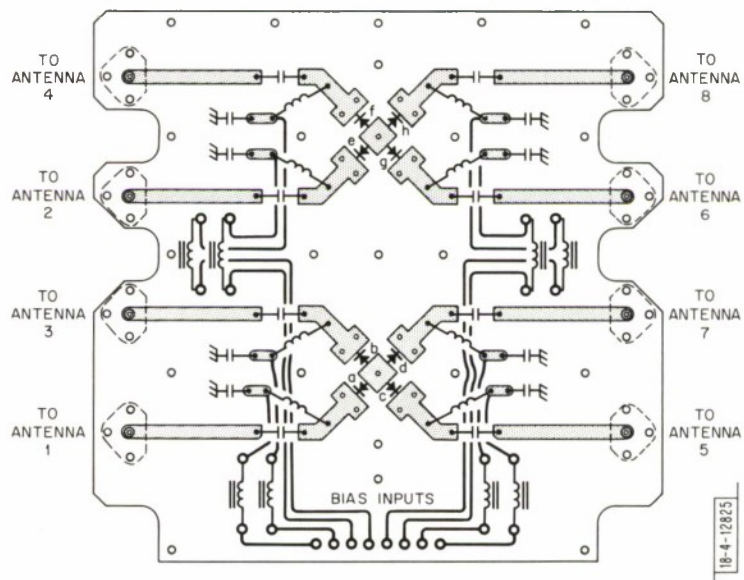
The stubs resulting from this configuration significantly mismatched the unit. To illustrate, if diode  $j$  is ON and diode  $k$  is OFF, the line going to diode  $k$  is a stub on the line carrying the RF signal to diode  $j$ . The VSWR was 1.85 at 250 MHz measured at one of the inputs. When the capacitor on the stub line was removed, the stub was essentially eliminated and the VSWR measured 1.05. This indicates, incidentally, that the SP4T section performance is satisfactory.

This stub behaves like a capacitor shunting the main line, and it is then logical to attempt to reduce the capacitance. To do this, the outer conductors on the two coaxial lines joining the 2P2T and SP4T sections were first eliminated and the two ground plane holes under the diodes were enlarged to a 1.25-inch diameter. This reduced the VSWR to 1.66. By narrowing the RF lines running from the points where they meet, which we henceforth designate points A, to the diodes to a width of 0.040 inch (for a characteristic impedance of 108 ohms), the VSWR is further reduced to 1.45. The normalized admittance at A was found to be  $0.953 + j0.359$ . This can nearly be matched by narrowing a short length of the line from the points A to the inputs. For





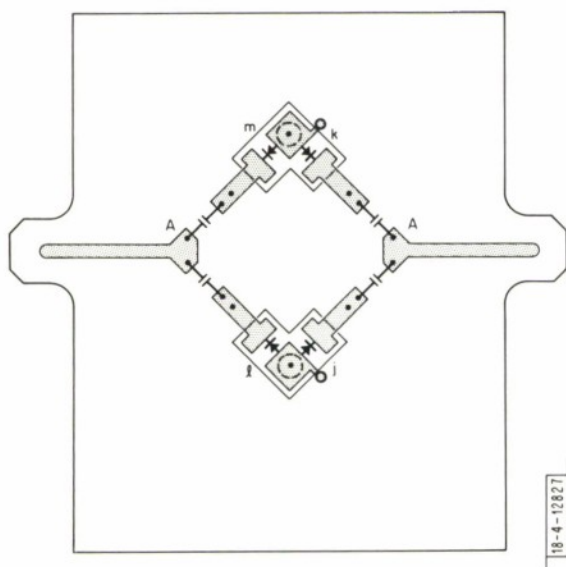
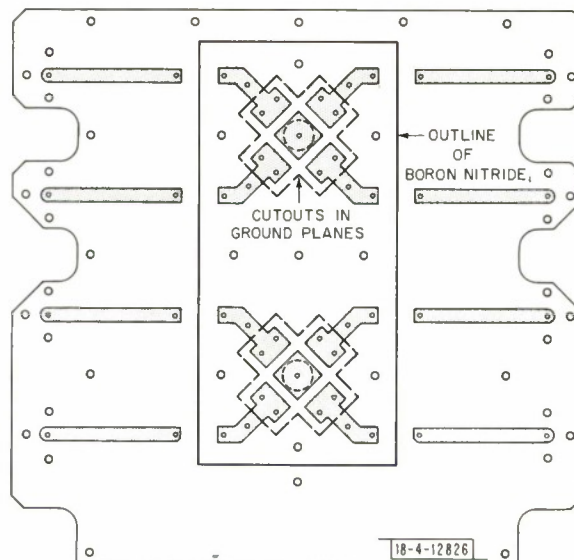
(o)



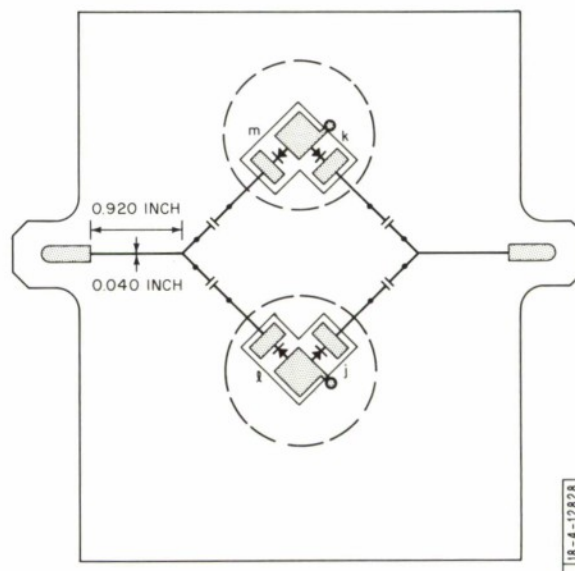
(b)

Fig. 20. View of etched circuit side of (o) 2P2T circuit layout and (b) SP4T circuit layout. Coils, capacitors and connectors would actually be hidden but have been added to this view.

Fig. 21. Cutouts in ground plane of SP4T circuit for diodes, and location of boron nitride slob.



(a)



(b)

Fig. 22. (a) Initial layout of 2P2T circuit showing diode positions and ground plane cutouts. (b) 2P2T circuit showing enlargement of cutouts on for ground plane and changes in RF line which improved match of layout of (a).

the best match, this length is determined to be 0.920 inch when the width is 0.040 inch. Implementing this change resulted in a VSWR of 1.14 at 250 MHz and 1.25 at 300 MHz. The 2P2T section is now as shown in Fig. 22(b).

It appeared that these VSWR values were satisfactory and this switch design was accepted until the investigation regarding intermodulation products indicated a necessary redesign. The information concerning intermodulation is given in Sec. VII, but we shall only indicate now that intermodulation amplitude increases when the two RF signals (transmit and beacon) across the diode are increased.

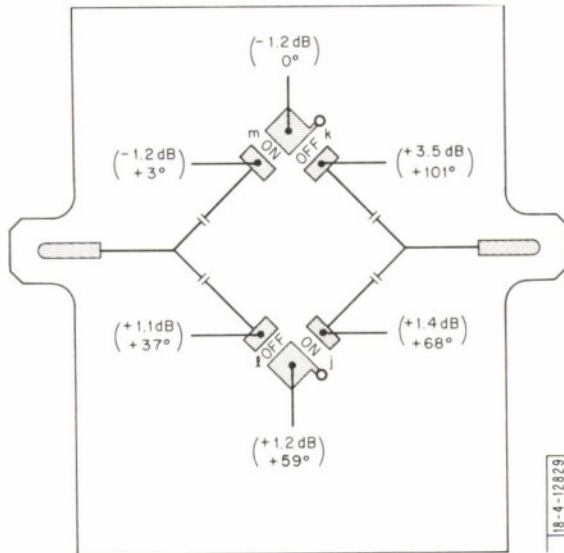


Fig. 23. Relative voltages and phases measured at various points in 2P2T section of Fig. 22(b). A high voltage exists across diode j or k, whichever is OFF, resulting in high intermodulation product levels (frequency 250 MHz).

It was found that when this switch was connected to the hybrid, thus providing signals at both inputs, the voltage across one diode was large. The measured relative amplitudes and phases are shown in Fig. 23 with diodes j and m ON, k and l OFF. The signals at the junction points tied to the SP4T sections differ in phase by  $59^\circ$  as set by the lengths of the coaxial lines joining the switch and hybrid. But we notice that one signal is 1.2 dB high and the other 1.2 dB low resulting from a peculiarity in the operation of this circuit (and not the hybrid, as verified in a separate measurement). Furthermore, the voltage across the OFF diode k is +5.4 dB above the normal signal (set at 0 dB); this is the vector difference of the  $(3.5 \text{ dB}, 101^\circ)$  and  $(-1.2 \text{ dB}, 0^\circ)$  voltages.

Removing the signal from the input tied to diodes l and m, the signal across diode k reduced to +2.4 dB, but nevertheless remained above the normal signal. Only the capacitances across the OFF diodes could have caused this change, since the two input signals are isolated in all other ways.

There was an attempt to demonstrate this behavior mathematically where signals are applied at both inputs, but the equations proved to be very complex. On the other hand, with a signal at one input only, the theory can be carried through easily. Let us consider the simplified circuit of Fig. 24. The line of characteristic

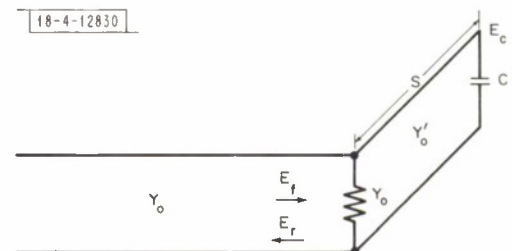


Fig. 24. Simple circuit illustrating high voltage across diode j or k represented here by a capacitor.

admittance  $Y_O$  is terminated in a load of admittance  $Y'_O$ . At the load is a stub of length  $s$  and characteristic admittance  $Y'_O$  terminated in a capacitance  $C$  to simulate the capacitances of the diode and boron nitride. Let the admittance of the capacitor be  $jbY'_O$  so that

$$bY'_O = \omega C \quad (26)$$

The reflection coefficient at the junction is

$$\frac{E_r}{E_f} = \Gamma = \frac{1}{jz - 1} \quad (27)$$

where

$$z = \frac{2(1 - bt)}{y(b + t)} \quad (28)$$

$$y = Y'_O/Y_O \quad (29)$$

and

$$t = \tan \beta s \quad (30)$$

$E_f$  and  $E_r$  are the voltages of the signals, incident and reflected, at the junction.

Let the signal across the capacitor be  $E_c$ . Since the reflection coefficient of the capacitor is

$$\Gamma_c = \frac{1 - jb}{1 + jb} \quad (31)$$

the incident and reflected signals at the capacitor are  $\frac{1}{2}(1 + jb) E_c$  and  $\frac{1}{2}(1 - jb) E_c$ . At the junction, these signals are  $\frac{1}{2}(1 + jb) e^{j\beta s} E_c$  and  $\frac{1}{2}(1 - jb) e^{-j\beta s} E_c$ , respectively. The combined voltage must be the combined voltage of  $E_f$  and  $E_r$ . Therefore

$$\begin{aligned} \left[ \frac{1}{2}(1 + jb) e^{j\beta s} + \frac{1}{2}(1 - jb) e^{-j\beta s} \right] E_c &= E_f + E_r \\ &= E_f(1 + \Gamma) \end{aligned} \quad (32)$$

Substituting Eqs. (27) and (28) and simplifying,

$$\frac{E_c}{E_f} = \frac{\sqrt{1 + t^2}}{1 - bt + j \frac{y}{2}(b + t)} \quad (33)$$

Amplitudes and phases of  $E_c/E_f$  are plotted in Fig. 25 for different stub lengths  $s$ , normalized admittances  $y$ , and capacitances  $C$ . Just what values this switch has is not known, but the plots show that the signal across the diode can be somewhat larger than the main signal.

With the high voltages across the diode, high intermodulation product amplitudes resulted, and consequently it was necessary to face the task of redesign. As evident from the data of Fig. 25, it was apparent that the stub lines had to be reduced in length and the capacitances at the diode reduced if possible. The diodes were repositioned as close to the junctions A as the diode blocks and capacitors would allow. Furthermore, instead of bonding the four capacitors in the RF line on the ground plane, an elongated hole was machined in the ground plane and half way through the rexolite sheet to accommodate these capacitors as shown in Fig. 26. This further reduced the line lengths. Little could be done to reduce the capacitances at the diode, and only the corners of the diode block were cut off.



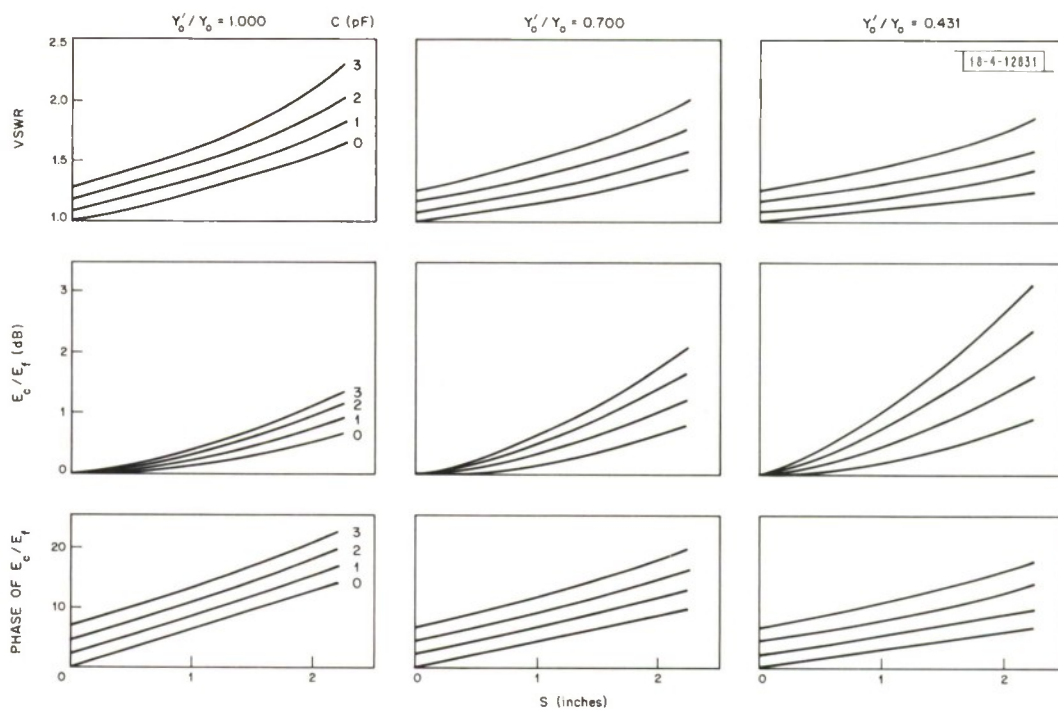


Fig. 25. Calculated characteristics of circuit of Fig. 24.

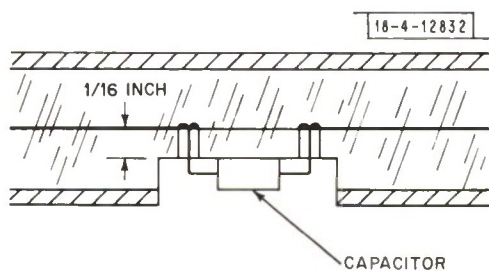


Fig. 26. Revised mounting configuration of capacitors of 2P2T section which helped reduce voltage across diode j or k.

In this new configuration, without any attempt at matching, the VSWR measured 1.46 at 250 MHz and 1.71 at 300 MHz. The admittances at the junction points A measured respectively about  $1 + j0.384$  and  $1 + j0.542$  at the two frequencies. By narrowing part of the lines from the inputs to the junctions as before, the lowest value of the VSWR that can be obtained theoretically at 250 MHz is 1.20. Instead, short-circuited stub lines were added at the junctions to achieve better matching. The bandwidth of the assembly is best when the stub is as short as possible. This means that the shorted stubs should have a high characteristic impedance. Choosing the stub lines 0.032 inch wide ( $Z_0 = 116$  ohms) and 4.124 inches long, the calculated VSWR's are 1.02 and 1.33 at 250 and 300 MHz. If we had used 5.75-inch long stubs of 50-ohm impedance, the VSWR's would have been 1.02 and 1.52. Incorporating the stubs into the switch, the VSWR's averaged about 1.14 and 1.25. To note the effect of the boron nitride, both slabs were removed; the VSWR values were then 1.08 and 1.13.

The question now arises as to whether the voltages across the diodes are sufficiently reduced. As before, the phases and amplitudes were measured, and the voltage across diode k relative to the normal signal level was found to be +4.1 dB. This value is some improvement, sufficient to bring the intermodulation product levels to acceptable values. It would have been desirable if the voltage could have been reduced further, but other attempts had little effect. It is to be noted that the uneven power division of the signals to the SP4T sections is less pronounced, i.e., +0.5 dB and -0.5 dB at the two junctions.

The final accepted layout of the 2P2T section circuit is shown in Fig. 20. The cutouts in the ground planes and the location of the boron nitride is pictured in Fig. 27.

In later mechanical vibration tests, it was indicated that additional material was needed to bond the components to the ground plane. This resulted in some degradation in the VSWR values to 1.20 and 1.30 on the average at the two frequencies. Complete characteristics of the switches used on the satellite are given in Sec. III-D and Appendix A.

### C. Assembly

Figures 28 through 35 show the steps in the construction of the switch matrix.

Figure 28 shows the SP4T section rexolite circuit board after the photoetching, and Fig. 29 the 2P2T section circuit after photoetching, machining and drilling. Subsequently, each circuit board is fastened to an appropriately cut ground plane and the components, including the diodes, are bonded and soldered in place as shown in Fig. 30. The completed rexolite sandwiches have the appearance shown in Fig. 31. The remaining hardware that makes up the whole switch is also shown.

Figure 32 shows the mounting of the diodes in their respective metal blocks in an SP4T section. Each diode is bonded in a rexolite strip which in turn is bonded to the metal block to help strengthen the diode support. The diode mount of a 2P2T section is shown in Fig. 33. A metal

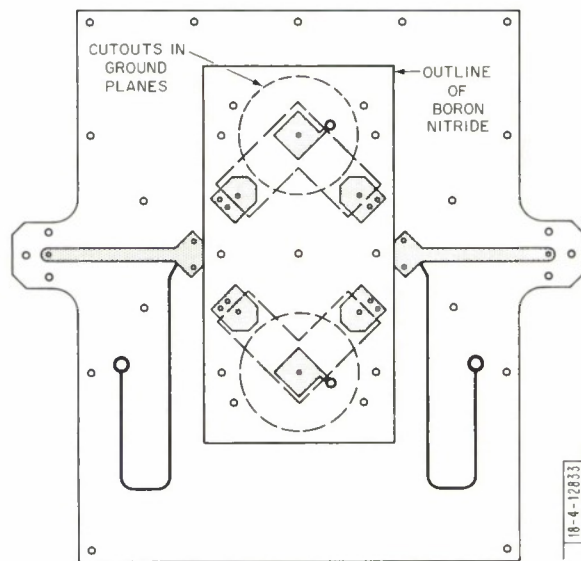


Fig. 27. Cutouts in ground planes of 2P2T section and location of boron nitride slab in final configuration [see circuit of Fig. 20(a)].

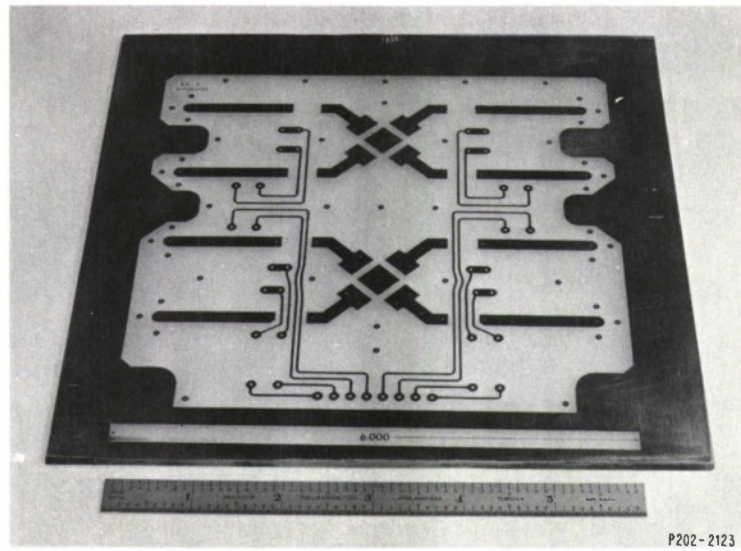


Fig. 28. Rexolite board with circuit of SP4T sections etched on copper clad.

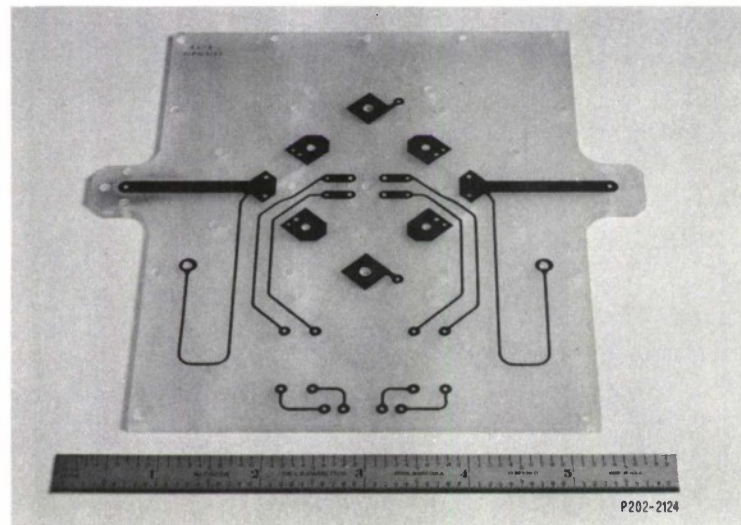


Fig. 29. Rexolite board with circuit of 2P2T section etched on copper clad after machining.

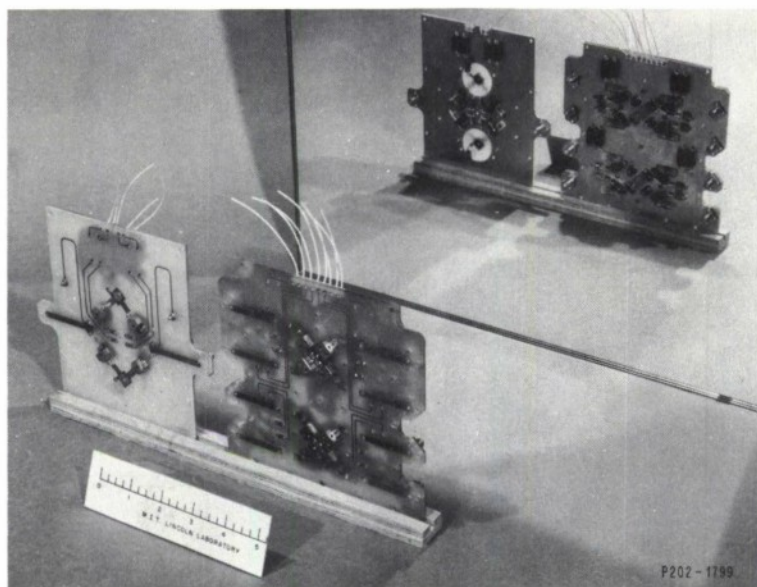


Fig. 30. Circuit boards of 2P2T and SP4T sections with ground planes and components mounted and soldered in place.

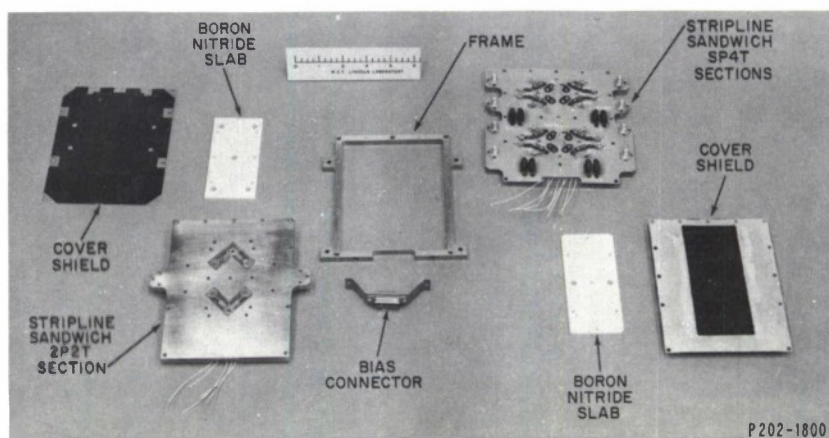


Fig. 31. Completed stripline sandwiches and remaining parts needed for full switch assembly.



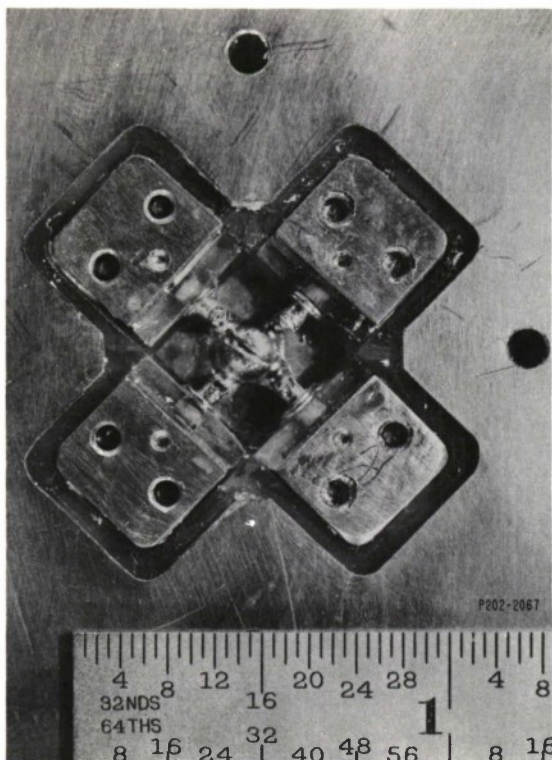
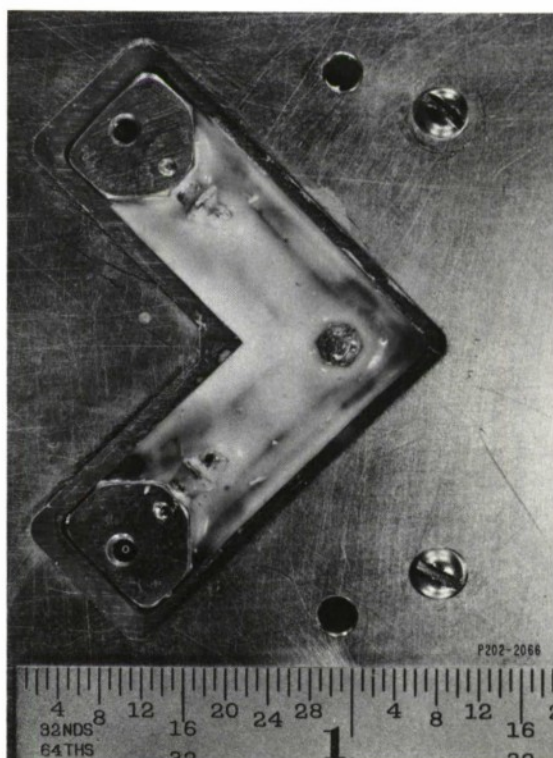


Fig. 32. Magnified view of diodes mounted in SP4T section. Each diode is bonded in a rexolite piece for additional strength.

Fig. 33. Magnified view of two diodes mounted in 2P2T section. Thin layer of RTV cushions diode against vibrations of launch.



strip joins the diode electrically to the junction. A thin layer of RTV is used to cushion against vibration of the strip and the diode during the satellite launch.

Figure 34 shows the switch assembled except for the shield cover, the last item to go in place, and Fig. 35 is a photograph of the completed switch. All the metal parts machined for the switch were made from light weight aluminum and gold plated. Some had small holes drilled to allow the air to bleed out when the satellite leaves the atmosphere. (One is visible in the middle of the shield cover in Fig. 34.) The shield covers were painted black on the outside and the underside of the raised portion to help dissipate the heat through radiation.

A procedure was set up for assembling the flight switches. All the machined parts were first thoroughly inspected and cleaned. The diodes were subjected to a screening procedure to improve their reliability as we shall describe in Sec. XI. Each switch was assembled under "clean room" conditions and repeatedly inspected for workmanship quality and cleaned. It was particularly important to have good solder connections especially because of the intermodulation products that arise from imperfect contacts. The electrical characteristics were checked several times during the assembly as a second check on the construction.

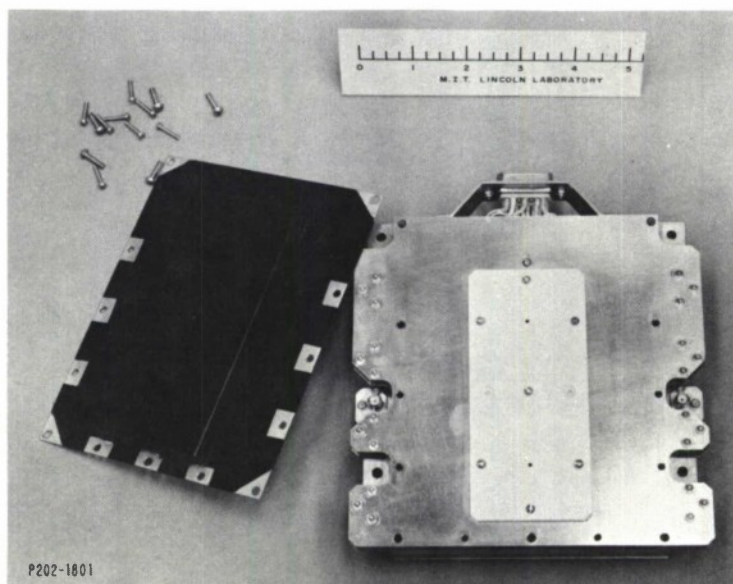


Fig. 34. Switch matrix with shield cover removed to reveal boron nitride slab banded and bolted in place.

The dimensions of the switch are given in Fig. 36. Its weight is 1 pound,  $13\frac{1}{2}$  ounces (837 grams). Each switch contains more than 400 separate items.

The two switches were later mounted on the triplexer in the satellite. Figure 3 is a photograph of the satellite platform with the switches and other electronic components mounted on it. The switches can be seen centrally located inside the aluminum ring. The two input hybrids are to the left and right of the switches.

#### D. Switch Performance

In normal operation, the switch may be in any of the 16 states corresponding to the 16 beam positions as illustrated in Fig. 6. To suitably characterize the RF performance of the switch

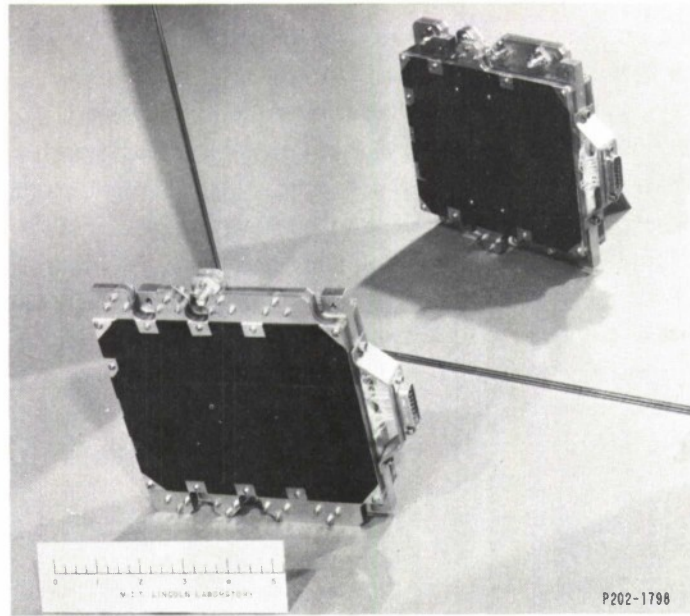


Fig. 35. Completed switch.

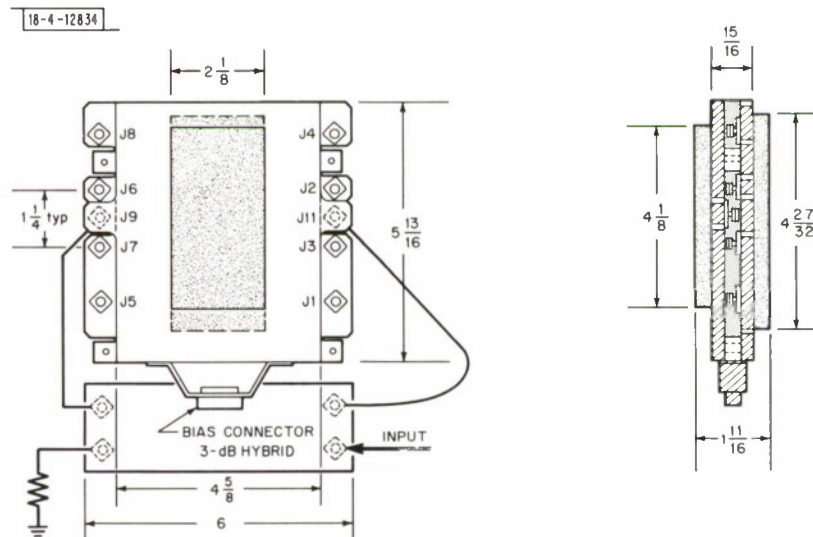


Fig. 36. Outline of switch showing dimensions.

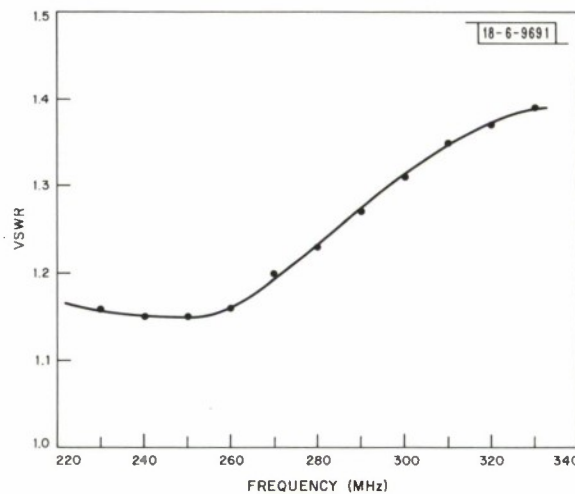


involves measurements of VSWR, insertion loss, isolation, and phase of all 16 states. Complete data on the switches that went into the satellite are given in Appendix A.

Let us summarize the characteristics here. In all cases, the diode was forward biased at 50 mA or reverse biased at 100 V. At these values, the characteristics are not sensitive to bias.

By measuring at either of the two inputs of the switch, the VSWR varied from 1.1 to 1.25 at 250 MHz and 1.25 to 1.35 at 300 MHz. (In all measurements, the output ports were terminated in loads or detectors whose VSWR never exceeded 1.05.) The insertion loss ranged from 0.4 to 0.5 dB and 0.5 to 0.7 dB at the two frequencies. The isolation, the ratio of the signals exiting from an ON and an OFF port, always exceeded 19 and 17 dB. The VSWR was measured over a frequency range for one beam position of one of the switches. The results shown in Fig. 37 indicate the good bandwidth of the design. (It thus may be expected that the insertion loss and isolation also vary little throughout the band.)

Fig. 37. Typical VSWR characteristic of switch matrix as a function of frequency as measured at an input.



A hybrid, such as one used on the satellite, was connected to the switch, and additional data taken. The relative phases of the signals at the two output ON ports depends on the lengths of the lines connecting the switch and hybrid. For the lengths chosen for this measurement, the phase difference ranged from  $44^\circ$  to  $48^\circ$  at 250 MHz and  $34^\circ$  to  $38^\circ$  at 300 MHz. Figure 38 shows a complete set of data on the relative signal levels at various points in the combination using the satellite switch that was later connected to the dipoles. The values given at the input and output ports are measured. The other values are calculated from them and are probably less accurate.

Another mode of operation of the switch was suggested in which all the output ports would have signals equal in phase and amplitude. As mentioned in Sec. I, this mode, the Omni-Mode, was introduced to guard against a failure in the logic circuit operating the switch. To obtain this condition in the switch, the only method that could be used without redesign was putting all 12 diodes on forward bias. Then, any output port would receive the same signal as any other for they all see the same configuration within the switch. It is expected that the switch will not be well matched and there is increased loss. The results of measurements in the Omni-Mode are shown in Fig. 39. The values are affected by the relative phases of the two connecting cables, so two sets are given, one for a  $46^\circ$  phase difference and the other for a  $63^\circ$  phase difference, roughly the values corresponding to those used on the satellite for the slots and dipoles, respectively.



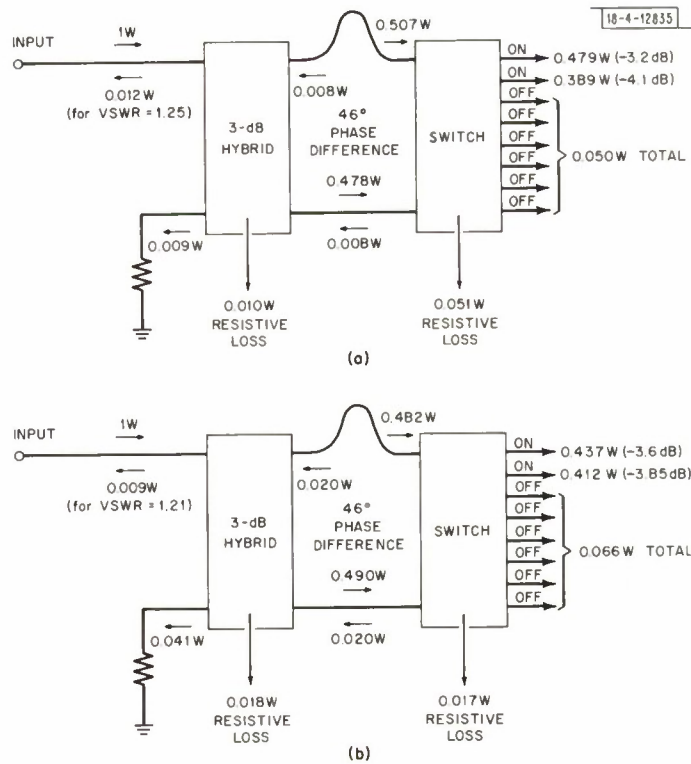
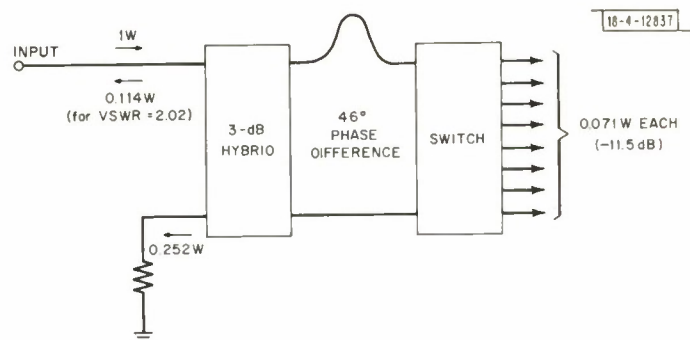
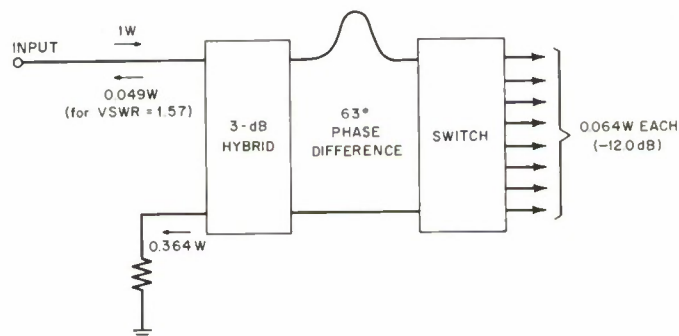


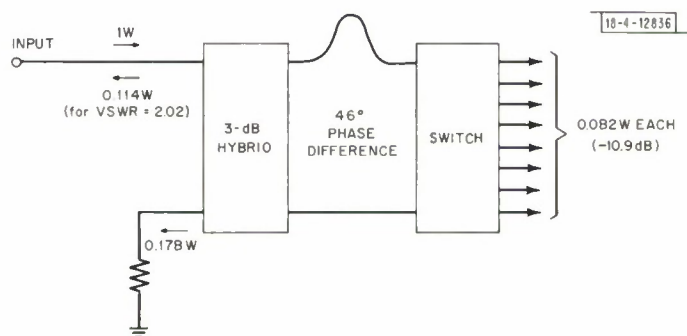
Fig. 38. Signal levels an various lines of switch-hybrid combination with input level normalized to 1 W and switch in Scan Mode. (a) Frequency = 250 MHz; relative phase of the two output ON signals is set to  $46^\circ$  at 250 MHz. (b) Frequency = 300 MHz; relative phase =  $46^\circ$  at 250 MHz.



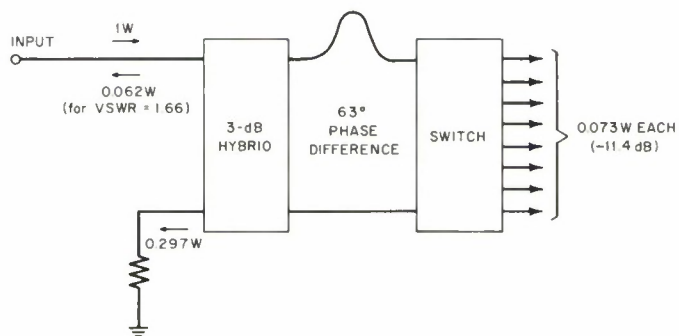
(a)



(b)



(c)



(d)

Fig. 39. Signal levels of switch-hybrid combination with switch in Omni-Mode. Relative phase values given are those that would be exhibited by switches operating in Scan Mode at 250 MHz. (a) Frequency = 250 MHz; relative phase =  $46^\circ$ . (b) Frequency = 250 MHz; relative phase =  $63^\circ$ . (c) Frequency = 300 MHz; relative phase =  $46^\circ$ . (d) Frequency = 300 MHz; relative phase =  $63^\circ$ .

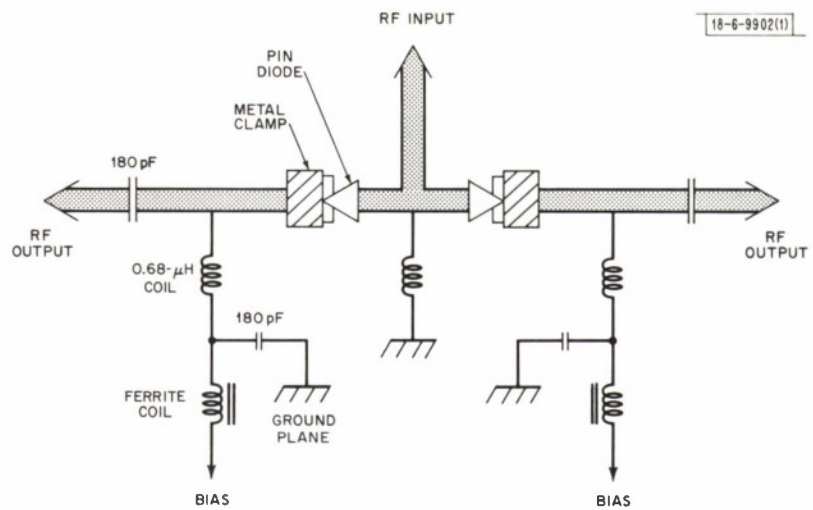


Fig. 40. Circuit of SP2T switch used in some tests.

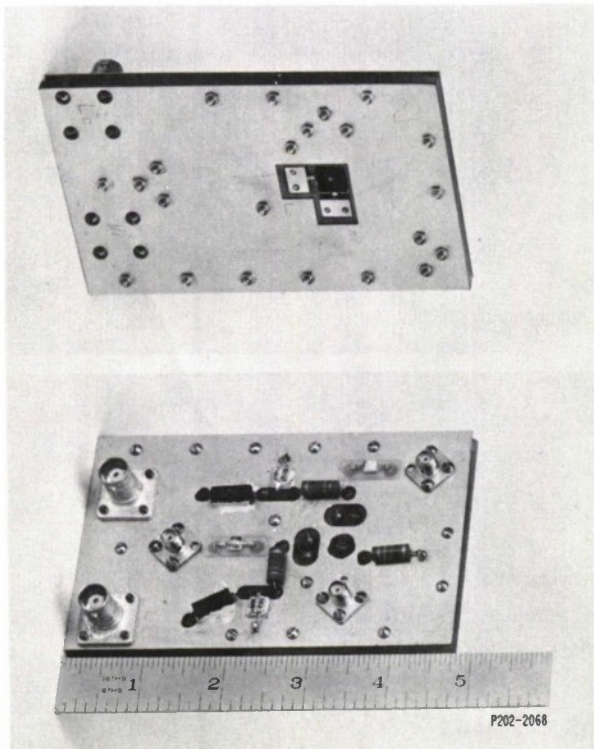


Fig. 41. SP2T switch, front and back views.

#### IV. MEASURED AND THEORETICAL PERFORMANCE OF SEVERAL SWITCH CONFIGURATIONS

##### A. SPST and SP2T Switches

In addition to the switch matrix, SPST and SP2T switches were constructed. The SPST switches were built to be used for thermal-vacuum and noise figure measurements. The circuit of each is shown in Fig. 5(b) and the diode mounted in the manner of either Fig. 18 or 19. The insertion loss of these switches measured about 0.15 dB where the diode resistance was quoted to be about 1 ohm.

The SP2T switches were used for measurements of intermodulation products and switching noise. The circuit is shown in Fig. 40 and a photograph in Fig. 41. The two diodes were placed at the junction as in the SP4T sections of the switch matrix. No provision was made for heat dissipation since it was not needed for the particular measurements for which the switches were built. The same type of coils, capacitors and OSM connectors as those of the switch matrix were mounted in the same way.

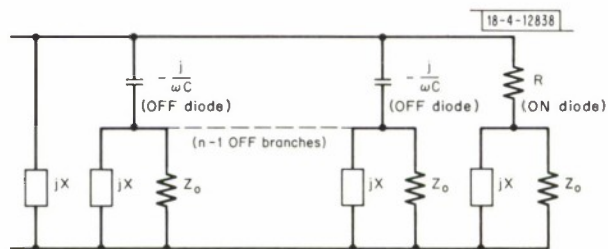
Typically, the SP2T switches exhibited an insertion loss of about 0.17 dB and an isolation (ratio of the signals at the two output ports) of about  $21\frac{1}{2}$  dB at 250 MHz. The average VSWR was 1.15. (The diodes had parameter values of about 0.6 ohm resistance forward bias and 0.8 pF capacitance reverse bias according to the manufacturer.) In a separate measurement of one switch, one diode was removed and the other replaced by a metal rod. The loss measured 0.03 dB (after subtracting the loss due to reflection). It may then be supposed that there is 0.12 dB loss due to the resistance of the ON diode and leakage out of the OFF port, 0.03 dB loss due to other components including the stripline itself, and 0.02 dB loss due to reflection.

##### B. Theoretical Approach to Loss of SPnT Switch

It is useful to compare the measured losses of these various switches with theoretical values to aid in understanding their operation. Furthermore, the losses of a switch determine the temperature characteristic and this is important in the consideration of reliability as we shall see later.

The general SPnT switch can be described with little difficulty and the results applied to the SPST, SP2T switches and SP4T section of the switch matrix. On the other hand, the 2P2T section poses enough difficulty to warrant omitting its consideration. In this case, for the sake of expediency, it will be assumed that the OFF diodes are absent and the loss results from the ON diodes alone.

Fig. 42. Representation of general SPnT circuit. Diode behaves like a capacitor when OFF and resistor when ON.



As pictured in Fig. 42, the SPnT switch is a junction of  $n - 1$  OFF diodes and 1 ON diode, each terminated in the characteristic impedance  $Z_0$ . Shunting each impedance  $Z_0$  is the reactance  $X$  of the coil carrying the bias signal. (The resistive component of the coil can be neglected due to its large value.) Each OFF diode is represented by a reactance  $-1/\omega C$  and the ON diode



by a resistance  $R$ . These representations are sufficiently accurate at UHF frequencies, although the diode equivalent circuit is rather complex.

The input power  $P_i$  equals the total power absorbed by the  $n$  branches. (This is the incident power reduced by the amount of reflected power.) If  $P_j$  is the power absorbed by each OFF branch and  $P_a$  the power absorbed by the ON branch, then

$$P_i = \sum_{j=1}^{n-1} P_j + P_a \quad (34)$$

where the summation is over all the OFF branches. If they are identical,  $\sum P_j$  can be replaced by  $(n-1) P_j$ . Let  $P_o$  be the output power, that is, the power absorbed by the impedance  $Z_o$  in the ON branch. The magnitude of the current in the impedance is

$$I_o = \sqrt{\frac{P_o}{Z_o}} \quad (35)$$

The current through the diode resistance  $R$  is

$$I_R = I_o \left| 1 + \frac{Z_o}{jX} \right| \quad (36)$$

and the power absorbed by it is

$$P_d = I_R^2 R \quad (37)$$

Substituting Eqs. (36) and (35) into Eq. (37), we get

$$\frac{P_d}{P_o} = R \left( \frac{1}{Z_o} + \frac{Z_o}{X^2} \right) \quad (38)$$

The magnitude of the voltage across the input to the circuit is

$$V_i = I_o \left| Z_o + R + \frac{RZ_o}{jX} \right| \quad (39)$$

The power absorbed in an OFF branch is then

$$P_j = V_i^2 \operatorname{Re} \frac{1}{-\frac{j}{\omega C} + \frac{jXZ_o}{jX + Z_o}} \quad (40)$$

( $\operatorname{Re}$  denotes the real part of the expression.) Substituting Eqs. (39) and (35) and simplifying,

$$\frac{P_j}{P_o} = (\omega CR)^2 \frac{\left( \frac{1}{Z_o} + \frac{1}{R} \right)^2 + \left( \frac{1}{X} \right)^2}{\left( \frac{1}{X} - \omega C \right)^2 + \left( \frac{1}{Z_o} \right)^2} \quad (41)$$

The ratio  $P_j/P_o$  is just the isolation as defined earlier (or its reciprocal if the sign of the dB value is significant). It should be noted that it is independent of the characteristics and the number of other ports in the switch.

The power absorbed in the ON branch  $P_a$  is simply

$$P_a = P_o + P_d \quad (42)$$

Equation (34) then gives us

$$\frac{P_i}{P_o} = \sum_{j=1}^{n-1} \frac{P_j}{P_o} + \frac{P_d}{P_o} + 1 \quad (43)$$

where  $P_j/P_o$  can be found from Eq. (41) and  $P_d/P_o$  from Eq. (38). The ratio  $P_i/P_o$  is the insertion loss of the switch if the reflected signal is neglected. (A correction can always be applied when a VSWR value is found by calculation or measurement. It is usually small.)

For the SPST unit, one case that can be handled by these equations is when the unit is in series with the transmission line and is ON. Then  $P_j = 0$  and the insertion loss is given by the quantity in Eq. (38) plus one. If the unit shunted the line and is OFF, then  $P_d = 0$  and the insertion loss is the isolation plus one. The isolation can be found from Eq. (41) where  $R = 0$ .

Let us now compare the characteristics resulting from these sets of equations with the measured values. A specific example of one of the measurements of an SP2T switch is when the isolation is  $21\frac{1}{2}$  dB and insertion loss is 0.12 dB (the total loss of 0.17 dB less 0.05 dB loss due to other components and reflection). The values as used in the equations are then

$$\frac{P_j}{P_o} = 0.0072$$

$$\frac{P_i}{P_o} = 1.028$$

$$Z_o = 50 \text{ ohms}$$

and

$$X = 2000 \text{ ohms} \quad (44)$$

This value of  $X$ , as estimated from the graph of Fig. 13, may not be accurate, but it is not critical because of its large size.

Equation (43) gives  $P_d/P_o = 0.0208$ , and Eq. (38) then gives  $R = 1.04$  ohms. In this example, the particular diode used in the ON port has  $R = 0.56$  ohm according to the manufacturer. The difference in resistance arises from other losses including contacts associated with the diode package as well as a difference in technique in making the resistance measurement.

With  $R = 1.04$  ohms, Eq. (41) gives  $C = 1.06$  pF. The diode in the OFF port has a value  $C = 0.88$  pF according to the manufacturer. The difference in values is probably due to the mount for the diode which must necessarily increase the capacitance across the diode.

In the case of the SPST unit, which is ON and in series with the line, if the same value of  $R$ , 1.04 ohms, is assumed, the insertion loss would be expected to be

$$\frac{P_i}{P_o} = 1 + \frac{P_d}{P_o} = 1.0208 \quad (45)$$

which corresponds to 0.09 dB. The measured value of 0.15 dB is in line with this result considering that the resistance of the diode is a little higher than that used in the SP2T switch (1 ohm according to the manufacturer) and the reflection and other component losses were not included.

For the SP4T section of the switch matrix, if again the diode loss is taken as  $P_d/P_o = 0.0208$  and isolation as  $P_j/P_o = 0.0072$ , the insertion loss is expected to be [Eq. (43)]  $P_i/P_o = 1.0424$  which corresponds to 0.18 dB.

If an additional loss of about 0.15 dB is estimated for the 2P2T section (a best guess based on the losses evaluated above) and smaller losses totaling about 0.1 dB are assumed for other hardware items of the switch matrix, the total loss of the switch approximates the measured values of 0.4 to 0.5 dB.

Based on these estimates, a reasonable approximation is that there is a 0.2-dB loss for each diode the RF signal passes through. This point is a factor in the choice of switch configuration as discussed in Sec. XII. A more critical point relates to the determination of the increase in diode temperature from the power dissipation. In the light of the values determined here, the insertion loss is not too accurate. If it is not known whether the loss is 0.11 or 0.15 dB, this amounts to an uncertainty of  $\pm 15$  percent in the power dissipation in the diode. With this point in mind, a discussion is given in the next section on the temperature measurements of the SPST switches and the switch matrix.

Many measurements were made on the SPST unit for the thermal problem and the intermodulation product study as presented in the following sections. These problems were handled when the unit was both ON and OFF. In both instances, the same set of conditions as seen by the diode in the operating switch matrix had to be approximately duplicated. Namely, the forward-bias diode is in series with the transmission line and passes the RF signal. The reverse-bias diode with its termination is like a shunt on the line carrying the RF signal. Hence, measurements of the SPST unit were carried out accordingly; that is to say, for the ON case, the unit was placed in series with the RF line and for the OFF case, it was placed as a stub on the line and its free port terminated in a matched load.

## V. TEMPERATURE PROBLEM

### A. Introduction

The reliability of the switch matrix, and specifically of its components, depends on the temperatures these components will encounter in normal operation; a higher temperature generally implies poorer reliability. As made evident in the preceding sections, the losses of various components of the switch other than the diodes are sufficiently low that heating is not expected to be a problem for them. On the other hand, the diodes absorb more of the RF power and are more sensitive to temperature so we must be primarily concerned with them.

In the vacuum of space, the operating temperature of an electronic component depends upon the balance between internal heat generation and the conduction and radiation coupling to the satellite proper. Convection heat transfer is totally absent in the space environment. The satellite as a whole will assume a temperature profile determined by absorbed and radiated energy for given orbital conditions and total heat generation.

Efficient heat rejection from a component carrying a high power density requires that the composite internal resistance be minimized, and that the conduction and radiation thermal resistances from the component package to the satellite be controlled. Specifically for each switch diode, it was of primary importance to provide a good thermally conductive path between the diode stud and the package ground plane as well as between the ground plane and the satellite mounting. This meant that, in addition to a proper choice of materials, the geometry of the structure was important. Furthermore, close attention had to be given to the problem of

interface thermal resistances. And lastly, component surfaces had to be treated to provide high emissivity to maximize radiation heat transfer.

Measurements of temperatures on various switches were carried out in vacuum chambers where the pressure was kept below  $10^{-5}$  Torr (mm mercury) which is low enough to be representative of the space vacuum. It was not practical to attempt to duplicate actual conditions in every respect, namely mounting switches on a complete satellite and simulating the sun-earth environment. The investigation was carried out in logical stages that eased the study of the problem. As described in Sec. V-B, the SPST unit design was first examined to establish a scheme to keep the diode temperature within tolerable limits efficiently. A complete switch matrix was then checked to verify that temperatures remained acceptable in the more authentic system, as outlined in Sec. V-C. The detailed measurements made on the SPST units and switch matrix provided information on the overall thermal resistance of the package relative to the surrounding environment. This information was then used in a separate study of the complete satellite in its normal operating conditions.

#### B. Diode and SPST Unit

The temperature rise of a diode in an SPST unit is a function of the power absorbed as given by Eq. (38) and the composite thermal resistance. If the subtle but small effect of the bias coil is neglected, the second term of the equation can be omitted and we have

$$P_d = \frac{R}{Z_o} P_o \quad . \quad (46)$$

We shall define the thermal resistance  $\Theta_d$  as the ratio of the diode temperature increase  $\Delta T$  to the power dissipation  $P_d$ :

$$\Delta T = \Theta_d P_d \quad . \quad (47)$$

If the heat dissipation is entirely by conduction, the factor  $\Theta_d$  is independent of the sink temperature but is related to the thermal conductivity of the materials involved and the geometry of the piece. If radiation is an important factor in the value of the temperature, then  $\Theta_d$  depends on the viewing temperature according to the Stefan-Boltzmann law.

The temperature critical to the diode is that of the semiconductor chip itself and this cannot be measured conventionally. The manufacturer provides a thermal resistance value  $\Theta_j$  which relates the temperature increase  $\Delta T_j$  of the diode chip with respect to its stud to the power dissipation  $P_d$ . Then

$$\Delta T_j = \Theta_j P_d \quad . \quad (48)$$

Since the mechanism is conduction, the factor  $\Theta_j$  is a constant. Its value is determined for each diode using a method requiring two measurements, one involving power dissipation in the diode and the other not. In the two instances, the temperatures are set to give the same V-I characteristic and their difference observed.

To the temperature increase  $\Delta T_j$  can be added an increase  $\Delta T_c$  of the diode stud over the background temperature. This increase can be related as follows to the factor  $P_d$  by a relation corresponding to Eq. (48).

$$\Delta T_c = \Theta_c P_d \quad . \quad (49)$$



Depending on how much heat is radiated, the factor  $\Theta_c$  will depend to some extent on the background temperature. The total temperature increase  $\Delta T$  as given by Eq. (47) is then the sum of the increases of Eqs. (48) and (49). We have

$$\Delta T = \Delta T_j + \Delta T_c \quad (50)$$

and

$$\Theta_d = \Theta_j + \Theta_c \quad (51)$$

Combining Eqs. (47), (46), and (51)

$$\Delta T = (\Theta_j R + \Theta_c R) \frac{P_o}{Z_o} \quad (52)$$

The factor  $P_o/Z_o$  is fixed for the satellite. The term  $\Theta_j R$  is determined entirely by the choice of diode and the selection of diode is then a point for concern. The value of  $\Theta_j$  ranges from 10 to 20°C/watt for the 2-mil diodes and 15 to 30°C/watt for the 3-mil diodes that were obtained for this project. Although the 3-mil diodes exhibited a higher value generally, the resistance  $R$  was generally lower, as shown in Table II. The  $\Theta_j R$  product, which determines the temperature rise of the junction at a given RF power level, is then little different in the two cases. A good switch design must then be reflected in a low value of  $\Theta_c$ , the only parameter in Eq. (52) left to our control.

Two configurations were investigated, one (Fig. 18) depending on a 1-inch square metal block bonded to the diode to radiate the heat away, and the other (Fig. 19) using a  $\frac{1}{8}$ -inch slab of boron nitride, a good thermal conductor, to conduct the heat from the diode to the switch package. Measurements on the unit implementing the radiating block were carried out to determine whether this diode mounting arrangement was successful in minimizing interface thermal resistances and at the same time to obtain information about the radiation heat transfer capability of the package. This design was eventually discarded for two reasons. The first was that the 1-inch square radiating block did not have sufficient surface area to be an effective heat radiator. Secondly, the radiating block, being part of the center conductor of the transmission line, removed the shielding feature of strip transmission line leaving the circuit somewhat vulnerable to RFI. Nevertheless, temperature measurements for this configuration shall be included in this section because of the extent to which they characterize the diode performance under a number of conditions; these measurements were not made for the alternate configuration. The alternate arrangement by which a slab of boron nitride conducted the heat away from the diode to the switch package proved to be a much more efficient device, as we shall see shortly, and it was ultimately used in the switch design.

Measurements were made on two SPST units, one of each configuration, where the two diodes were 2-mil diodes having the same characteristics, namely, a thermal resistance  $\Theta_j$  of 18°C/watt and  $R$  of 1.0 ohm (manufacturer's values). Both switches had a measured insertion loss of 0.15 dB which corresponds to a calculated  $R$  of 1.67 ohms (using Eqs. (43) and (38)).

In the configuration employing the radiating block, five chromel-alumel thermocouples were bonded at the various points shown in Fig. 18. They were insulated by a thin film of epoxy (maximum thickness 0.010 inch) before being set in place. The thermocouple labeled number 1 in the figure was bonded on the metal cathode of the diode near the ceramic body to provide the temperature of the diode stud. Thermocouples Nos. 2 and 3 were bonded on the surface of the metal radiating block, one near the diode, to indicate whether an interface thermal resistance

problem existed. Thermocouple No. 4 was bonded near the edge of the switch package to give a measure of how much heat was conducted away from the diode rather than radiated from the metal block. Thermocouple No. 5 was located on the vacuum chamber inner wall to give the background or viewing temperature. The switch was suspended in the middle of the chamber by only the two coaxial cables that carried the RF power to and from the switch, so that the primary mode of heat transfer from the switch would be by radiation.

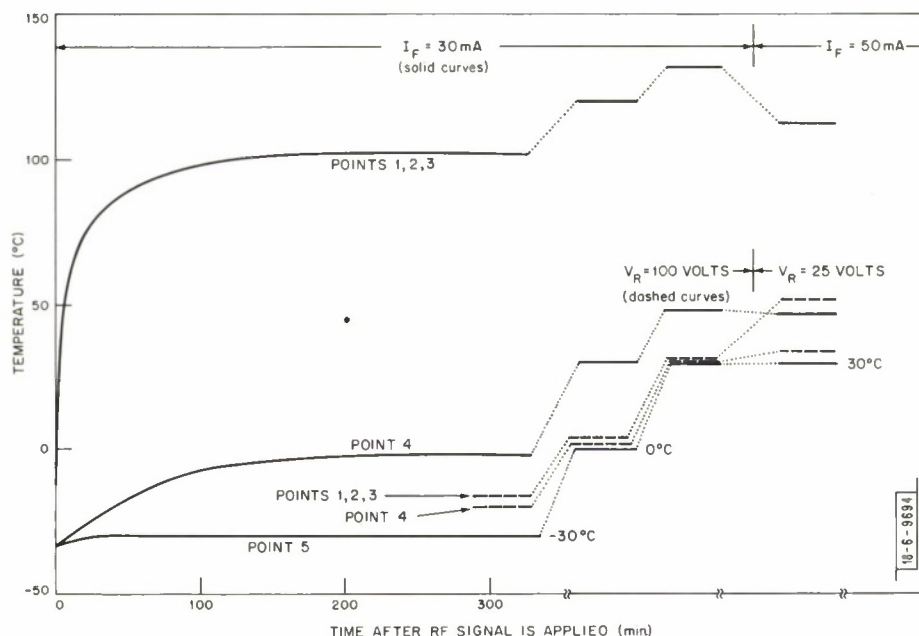


Fig. 43. Temperatures measured in vacuum chamber ( $P < 10^{-5}$  Torr) of SPST unit with radiative heat sink as shown in Fig. 18;  $P_T = 30\text{ W}$ .

Temperatures were measured for background temperatures of  $-30^\circ\text{C}$ ,  $0^\circ\text{C}$ , and  $30^\circ\text{C}$  with the RF power level set at  $f_T$ ; this power level is consistent with the RF power the switch matrix experiences in normal operation. Although the presence of the thermocouples did alter the performance of the switch slightly, it was considered to have negligible effect on the temperature values. The results of the measurements are plotted in Fig. 43. The first 300 minutes show the trend in the temperature; the other levels give the temperatures after stabilization. For forward bias, the switch was placed in series with the RF line, and for reverse bias, the switch shunted the line. The corresponding values of  $\theta_c$  are given in Table III.

Several observations can be made:

- (1) The temperature drop between the diode stud and radiating block was immeasurably small indicating low interface thermal resistance.
- (2) A reverse-biased diode in shunt with the transmission line experienced a considerably smaller temperature rise than the forward-biased diode in series with the line. (In the theory of Sec. IV, it was assumed that on reverse bias, the diode has no resistance. These measurements bear out that this assumption is sufficiently valid for most considerations.)
- (3) Decrease in the bias, forward or reverse, causes the temperature to rise indicating the dependence of diode resistance on bias. This characteristic is one reason for operating the switch at higher bias levels.
- (4) The radiation heat transfer capability of the package was poor as indicated by the high values of  $\theta_c$ .

TABLE III VALUES OF $\theta_c$ FOR VARIOUS VIEWING TEMPERATURES				
Viewing Temperature (°C)	$\theta_c$ (°C/watt)			
	Forward Bias		Reverse Bias	
	30 mA	50 mA	100 V	25 V
-30	130	—	14	—
0	120	—	4	—
30	100	80	2	22

On the second switch configuration, three thermocouples were bonded in place and the switch mounted as shown in Fig. 19. One thermocouple was implanted in the metal block holding the diode. Since it has been demonstrated that there is good heat transfer from the diode, this should provide accurate values of diode temperature. A second thermocouple was bonded on the ground plane at the edge of the boron nitride slab about 1 inch from the diode. A third monitored the temperature of the base supporting the switch. The switch was painted black to increase the surface emittance.

The only measurements taken on this switch were for a forward bias of 50 mA, the bias chosen for the switch matrix operation. The switch in series with the RF line carried 30 watts of RF power. Four sink temperatures were considered, -33°C, 4°C, 31°C, and 69°C. The observed temperatures after stabilizing are plotted in Fig. 44. Based on the difference in temperature of the diode and the switch support, the thermal resistance  $\theta_c$  remained at about 20°C/watt in the -30°C to +30°C range. The value increased at the high sink temperature of +69°C since radiation heat transfer was not as efficient at the higher background temperature.

The use of this approach (by conduction and radiation) to keep the diode temperature increase low was found to be successful, and was the method adopted for the satellite switches.

### C. Switch Matrix Temperatures

Temperature values for a switch matrix under normal operation were needed that were more accurate than could be provided by any measurements of an SPST unit. The switch matrix is designed so that a single boron nitride slab dissipates the heat from several diodes. On the other hand, any one diode is on forward bias for  $\frac{1}{4}$  or  $\frac{1}{2}$  of any interval of time. To further simulate the satellite conditions, the switch should be mounted in approximately the same way as in the satellite.

A switch matrix with 3-mil diodes was mounted on a filter similar to the triplexer filter used in the satellite. It was connected with a hybrid whose "4th port" was tied to a matched load. This assembly was mounted in the vacuum chamber and nine cables (1 input and 8 output) were run from the switch to coaxial connectors on the chamber wall. A photograph of this setup is shown in Fig. 45.

Four thermocouples were bonded to four diode blocks in the manner shown in Fig. 19 to measure the temperature of diodes c, g, k, and m. A fifth thermocouple was bonded on the blackened cover plate which is visible in the photograph. A sixth was bonded to one of the switch support



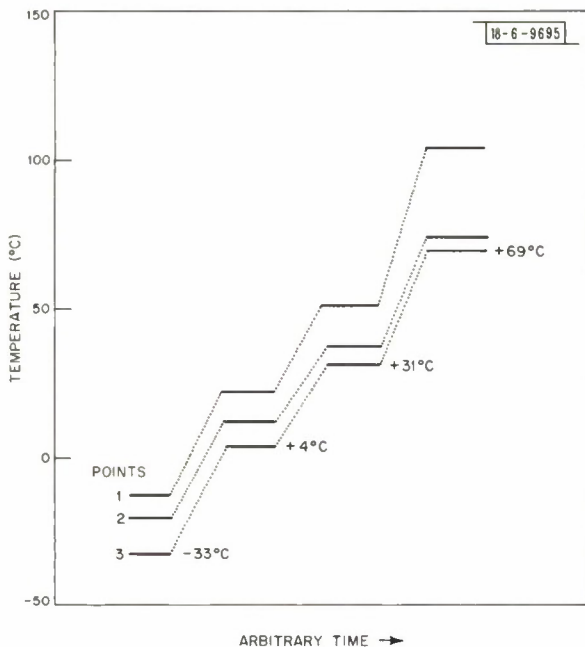


Fig. 44. Temperatures measured in vacuum chamber of forward-biased SPST unit with the thermal conductor, boron nitride, as shown in Fig. 19;  $P_T = 30$  W.

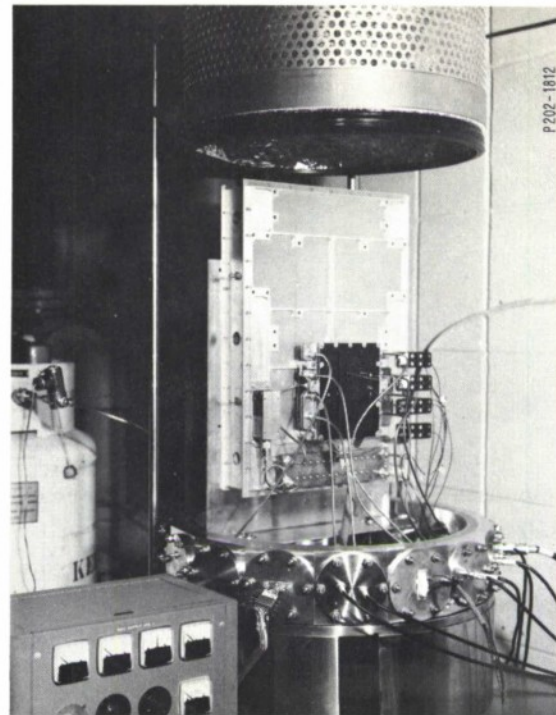


Fig. 45. Switch matrix mounted on a filter as on the satellite ready for thermal-vacuum tests.

legs near the center of the filter, also visible in the photograph. A seventh thermocouple was bonded on the top plate of the filter near its center. This gave what might be taken as the sink temperature.

The switch matrix used exhibited an insertion loss averaging about 0.38 dB and VSWR less than 1.10 (measurements without the hybrid). The cables connecting the switch and hybrid were chosen so that the two output signals differ by  $63^\circ$  in phase. The RF power used for the measurements was at a 60-watt level.

Three sets of temperatures were recorded. The first was for a set of biases on the diodes corresponding to beam J, that is, with diodes c, g, k and l on forward bias (and diode m on reverse bias). The second set was for the normal switch operation, that is to say, with the switch going through the switching sequence at the normal rate as on the satellite – the Scan Mode. The third set was for all diodes on forward bias, the Omni-Mode.

Table IV summarizes the temperatures measured for all three sets after conditions stabilized, requiring at least a 2-hour period of time.

We see that in normal satellite operation, any diode should experience a temperature increase of less than  $10^\circ\text{C}$  above the sink temperature. The high temperatures associated with the Omni-Mode are due to the large RF power dissipated in the "4th port" load, namely about 21 watts. This can cause a situation where a diode has a lower temperature than the sink. We notice also that if the cables had been chosen so that the phase difference of the output signals differed by  $46^\circ$  rather than  $63^\circ$ , the power dissipated in the "4th port" load would be about 15 watts as Fig. 39 shows. The sink temperature then would not have been as high as the value measured here.



TABLE IV MEASURED TEMPERATURES ON SWITCH MATRIX*			
Point	Temperature (°C)		
	Switch on Beam J	Switch on Scan Mode	Switch on Omni-Mode
Diode c metal block ( $R = 0.50 \text{ ohm}$ , $\theta_j = 26^\circ\text{C/watt}$ )	51	48	60
Diode g metal block ( $R = 0.74 \text{ ohm}$ , $\theta_j = 29^\circ\text{C/watt}$ )	$46\frac{1}{2}$	46	$57\frac{1}{2}$
Diode k metal block ( $R = 0.63 \text{ ohm}$ , $\theta_j = 20^\circ\text{C/watt}$ )	$46\frac{1}{2}$	47	54
Diode m metal block ( $R = 0.70 \text{ ohm}$ , $\theta_j = 23^\circ\text{C/watt}$ )	43	48	59
Switch surface	42	45	54
Support leg	41	42	57
Sink	40	41	56
* Values of $R$ and $\theta_j$ are provided by the manufacturer.			

The sink temperature values of these measurements are probably quite different from those expected on the satellite. In this setup, the mount did not have a good thermal connection with the bulk of the vacuum chamber. An extensive thermal study program of the satellite was made, as was mentioned earlier, indicating that the "sink" temperature, the average temperature on the instrument platform, should be at most  $40^\circ$  or  $50^\circ\text{C}$  even for the Omni-Mode. The diodes should heat no more than  $10^\circ\text{C}$  above this value, and the semiconductor chip should exhibit no more than another  $15^\circ\text{C}$  increase in the most pessimistic view. Therefore, the chip should get no hotter than  $80^\circ\text{C}$  under any conditions. This value is well within the margin needed for good diode reliability as is shown in Sec. XI.

## VI. MULTIPACTOR

Multipactor is a phenomenon which might be referred to as electrical arcing in a vacuum.<sup>11,12,13</sup> It occurs across two surfaces which have an oscillating electric field between them. In simplified terms, the nature of the phenomenon is that electrons dislodged from one surface at the appropriate time, by cosmic rays for example, are accelerated by the electric field to the other surface, there to dislodge more electrons. The electric field now having reversed polarity will accelerate the secondary electrons toward the original surface. Under appropriate conditions, the process continues to grow and eventually degrades the system operation. This degradation manifests itself in several ways:

- (a) An increased reflected signal affects the operation of the signal source and increases the system loss.
- (b) The surfaces involved deteriorate in quality.
- (c) Gas is liberated which may lead to a gas breakdown.
- (d) The noise level is increased.

Whether multipactor arises depends on several factors, namely, the frequency, amplitude, and configuration of the electric field, the shape and separation of the two surfaces, and the nature of the surfaces (which need not be metal). It is unlike electric arcing involving a gas. There the arcing intensifies due to ionization of the gas molecules and the pressure must be  $10^{-3}$  to  $10^{-4}$  Torr at least. Multipactor occurs at any pressure less than this down to a perfect vacuum.

The conditions for multipactor can be solved theoretically for specific surface and electric field configurations. For example, Fig. 46 shows the bounds on the conditions for multipactor for two parallel plates. A region exists on a plot of electric field amplitude  $E$  versus the frequency-surface separation product  $fd$  outside of which multipactor cannot occur. There is no multipactor for a sufficiently small value of  $E$  regardless of the value of  $fd$ , and vice versa.

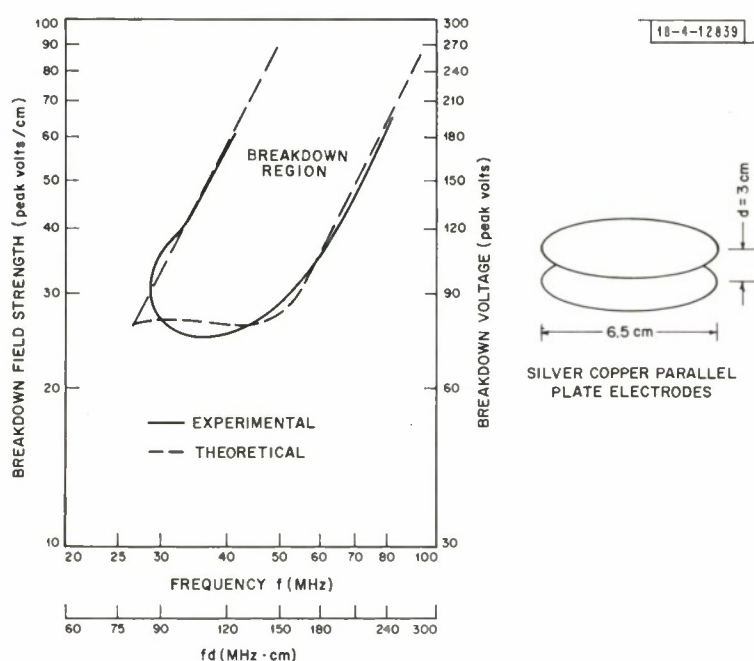


Fig. 46. Region of field strength-frequency-surface separation in which multipactor may occur for two parallel plates; experimental curve was obtained from configuration shown on right.

Likewise, for a larger value of  $E$ , there is a range of values of  $fd$  below or above which there is no multipactor. In the range of  $fd$  where multipactor may occur, the electrons involved adjust their position and velocity with respect to the phase of the electric field so that the time of flight between surfaces is a half period (or an odd multiple of a half period which is not plotted in the figure). This accounts for the range of parameter values that may give rise to multipactor. In the more general case — contoured surfaces and non-uniform electric field — there may be a region within the device which may meet the conditions for multipactor. For this reason, a test had to be made on a switch matrix to indicate any signs of the multipactor phenomenon.

It was convenient to take the same switch matrix setup used in the thermal measurements for this test (Fig. 45). The procedure of the test was to apply RF power in approximately 10-watt steps up to 75 watts and to observe any change in reflected signal from what is expected. Each step was of two minutes' duration. This range of power levels gave a safety margin above the normal 50 watts, as well as verifying that multipactor did not occur at below-normal levels. The procedure was carried through all 16 sets of bias states corresponding to the 16 beam positions where the electric field differs in each case. No effect of possible multipactor was noted. Multipactor may exist in the switch that is too weak to be observed, but it was concluded that in any case the switch performance was not measurably degraded.

## VII. INTERMODULATION PRODUCTS

### A. General

The satellite antenna system is designed to transmit simultaneously two high power signals, the transmit and beacon, and receive a very weak signal extending in frequency through the receive and RFI bands. Hence, the elements of the antenna system are of concern where they can possibly degrade the performance of the receiver. Specifically, the diodes in the switches (1) are nonlinear giving rise to harmonic and intermodulation frequency generation, (2) exhibit charge storage phenomena which generate switching transients, and (3) are noisy and lossy which contributes to the receiver noise figure. This section deals with the intermodulation products falling in the RFI band. Following sections are concerned with the switching noise and the noise figure.

Intermodulation products (IM) arise when a signal consisting of two frequencies and represented by the equation

$$i = I_T \sin 2\pi f_T t + I_B \sin 2\pi f_B t \quad (53)$$

passes through a nonlinear device whose characteristics may be described by a power series

$$e = \sum_{\ell} a_{\ell} i^{\ell} \quad (54)$$

An IM is a signal with a frequency which is a linear combination of the frequencies  $f_T$  and  $f_B$ , thus

$$f_{IM} = mf_T + nf_B \quad (55)$$

where  $m$  and  $n$  are integers. For a particular value for  $m$  and for  $n$ , the lowest order term of Eq. (54) that can give rise to this frequency, denoted as the  $k^{\text{th}}$  order, is

$$k = |m| + |n| \quad (56)$$

Rearranging Eq. (55), we get

$$f_{IM} - f_T = (m + n - 1) f_T + n(f_B - f_T) \quad (57)$$

For the satellite,

$$f_B - f_T = 5 \text{ MHz} \quad (58)$$

The IM falling in the RFI band are the primary concern, and for them

$$40 \text{ MHz} \leq f_{IM} - f_T \leq 65 \text{ MHz} \quad (59)$$

Substituting these frequency differences into Eq. (57),

$$40 \text{ MHz} \leq (m + n - 1) f_T + n(5 \text{ MHz}) \leq 65 \text{ MHz} \quad (60)$$

In the case where

$$m + n - 1 = 0 \quad (61)$$

then

$$8 \leq n \leq 13 \quad (62)$$

The corresponding  $m$ , by Eq. (61), is

$$-7 \geq m \geq -12 \quad (63)$$

and the IM orders [Eq. (56)] are

$$k = 15, 17, 19, 21, 23 \text{ and } 25 \quad (64)$$

Other possibilities such as  $m + n - 1 = 1$ ,  $-42 \leq n \leq -37$  also give rise to IM in the RFI band, but the corresponding values of  $k$  are 76 and higher. These values are too high to be of concern. If the lower orders are suitably taken care of, the higher orders will resolve themselves.

The beacon signal of the satellite is essentially a single frequency, but the transmit signal due to the characteristics of the transponder has a 500-kHz bandwidth. By Eq. (55), a frequency component  $\frac{1}{4}$  MHz from  $f_T$  would have a corresponding IM component  $m$  ( $\frac{1}{4}$  MHz) from its center. Thus, the bandwidth of the transmit signal is multiplied  $m$  times in the IM signal.

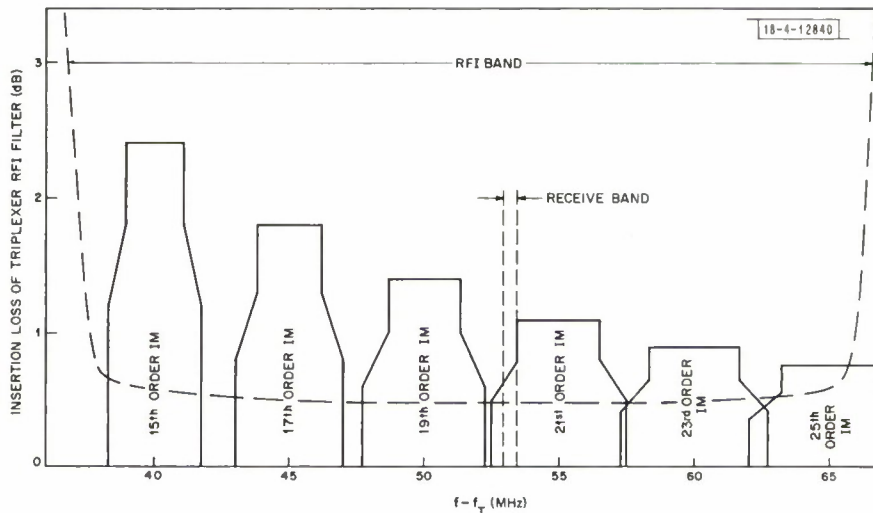


Fig. 47. Representation of intermodulation products (IM) of transmitter and beacon signals arising from nonlinear element in antenna system; typical pass band of the triplexer which determines extent to which IM gets to RFI instruments is also shown.

The spectrum of the IM terms falling in the RFI band is shown pictorially in Fig. 47. The spectral distribution of the transmit signal is approximately reproduced in each term but adjusted to an appropriate width. The peak amplitudes depicted are not significant other than that they generally, but not always, decrease with increasing order. Accurately placed in the plot is the receive band which is  $\frac{1}{2}$  MHz wide. Some of the 21st order IM falls in the band, but only on its skirt. There is a concern that IM might arise at any point in the antenna system, and it would



have been desirable to choose the transmit and beacon frequencies so that no IM falls in the receive band. However, due to restrictions imposed by the facilities of various potential satellite users as well as a consignment by certain groups on frequency allocation, the situation pictured was the most acceptable.

What IM frequencies get into the RFI instrumentation depends on the passband characteristics of the triplexer. The insertion loss for the triplexer employed in the satellite is plotted in Fig. 47.<sup>14</sup> It is apparent that for all of five orders and part of a sixth, the attenuation is less than 1 dB.

In addition to the transmit and beacon signals, a telemetry signal is transmitted from a separate antenna on the satellite. There will be some coupling into the switched antenna and some IM will be generated. The telemetry signal has a frequency of about

$$f_L = (f_T - 12.4) \text{ MHz} \quad . \quad (65)$$

The IM terms resulting from transmit-telemetry and beacon-telemetry interaction are plotted in Fig. 48. The orders are lower than the transmit-beacon IM and would be expected to be higher in amplitude for the same power levels. But the power level of the telemetry signal is initially

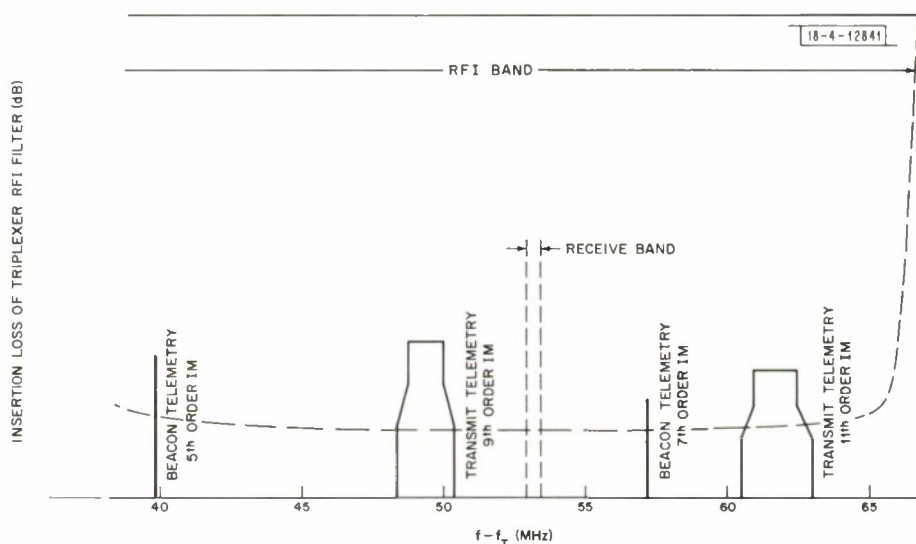


Fig. 48. Intermodulation products of transmit-telemetry and beacon-telemetry signal combinations.

lower than the beacon and is further reduced by the loose coupling between the two antennas. The telemetry is a single frequency signal, and the IM resulting from the interaction with the beacon has no bandwidth.

Ultimately, IM arises from all three signals. The lowest order in this case is the 7th which results from five different combinations of frequencies. One example is

$$F_{IM} = -f_T + 4f_B - 2f_L = f_T + 44.8 \text{ MHz} \quad (66)$$

The combination falling nearest the receive band is

$$F_{IM} = +f_T + 3f_B - 3f_L = f_T + 52.2 \text{ MHz} \quad (67)$$

Interestingly, the bandwidths of these IM terms are the same as the transmit signal.

The amplitude of the IM reaching the transponder and RFI instruments, although generated by the diodes of the switch matrix, depends very much on the characteristics of other satellite components. First of all, not only does the IM amplitude depend on the power levels of the signals, but also on the shape of their spectrums. The spectrum of the transmit signal was largely a consequence of the information it was designed to carry. Secondly, the IM depends on the impedances of the RF system. As an example of an extreme case, suppose there is a resonance at frequency  $3f_T$  on the RF line where the IM is generated. Then the third harmonic of the transmit signal which is generated is greatly increased in amplitude and would react accordingly with the beacon signal to give IM in the RFI band which would differ in amplitude if the resonance did not exist. In a less extreme situation, the mere difference of VSWR in the satellite and in a measurement setup would alter the IM levels. Thirdly, as pointed out earlier, the IM associated with the telemetry depends on the coupling between antennas. The conclusion is then, like the thermal problem, that the IM levels that exist on the satellite can only be found accurately by measurements on the actual satellite.

The study of the IM problem is then carried out under the following philosophy. IM is examined in an SP2T switch to establish ways in which the IM arising from the diode can be minimized. The IM generated in the switch matrix connected with the 3-dB hybrid is then found so that levels are demonstrated to be suitably low. Finally, the transponder and RFI instrument sensitivity in the complete satellite is recorded.

Sections VII-B and VII-C deal with IM generated in the SP2T unit and the switch matrix, in particular the IM of the transmit-beacon combination of the 15th, 17th, 19th. . . 25th orders and primarily of the 15th order because of its higher intensity. The maximum IM level for normal operating conditions is set by the transponder and RFI instrument sensitivity which is  $-120$  dBm. Because of the possible large variation in IM level and the difference between measurement and actual conditions, a goal was set for a maximum IM of  $-130$  dBm throughout the RFI band to give a good safety margin. This value was adopted as the criterion for the switch design.

## B. Intermodulation Products from the PIN Diodes<sup>15,16,17</sup>

As indicated in Sec. III-B, if the diode is not located at the junction, the RF voltage across the diode is not the same as the RF voltage on the line. Thus, to get the true IM generation characteristics of the diode, it must be placed adjacent to the main RF line. If SPST units are used, two are needed, one for forward bias cases where the diode is in series with the line, and the other for reverse biases where the diode shunts the line. The use of an SP2T switch accomplishes both purposes: if a forward-biased diode is measured, the diode in the other arm of the SP2T switch can be omitted, and for a reverse-biased diode, the other diode is replaced by a short metal rod. The diodes are located adjacent to the junction; a photograph of the switch with two diodes in place is shown in Fig. 41.

Figure 49 is the equipment setup used for measuring the IM amplitudes. It essentially represents the satellite system except that the switch output ports are terminated in matched loads rather than antennas. Two signals are combined by a triplexer to be passed on to the switch under test. Signals falling in the RFI band are then separated by the triplexer and monitored. The triplexer is a junction of three bandpass filters with pass bands of  $f_T$ ,  $f_B$  and the RFI band. The insertion loss of these filters at the three frequencies is given in Table V. The VSWR in the low insertion loss cases is 1.2 or less.

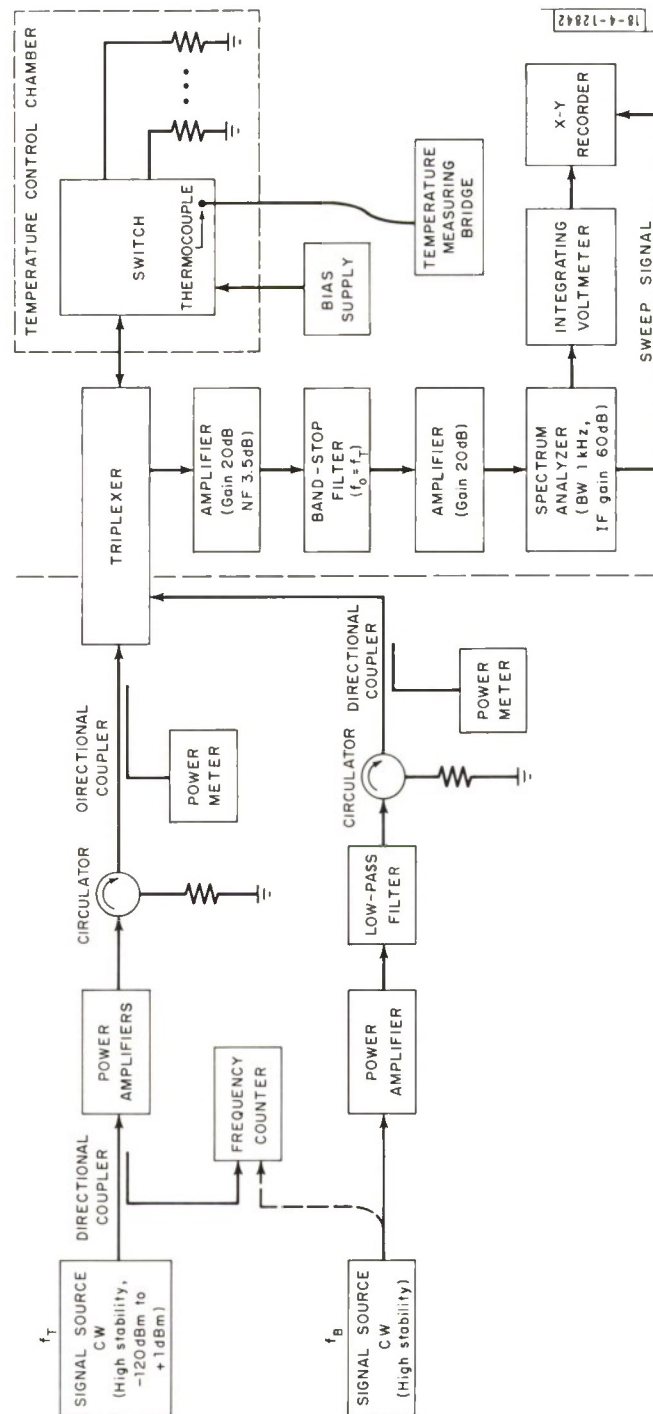


Fig. 49. System for measuring amplitudes of IM arising from switch.

TABLE V INSERTION LOSS OF TRIPLEXER FILTERS			
Filter	Insertion Loss (dB)		
	$f_T$	$f_B$	RFI Band
Transmit	0.6	44	>90
Beacon	44	0.6	>90
RFI	>90	>90	0.5

The signal sources have good frequency stability – residual FM is 1.2 kHz maximum by specification. Included in the lines tied to the signal sources are circulators to safeguard against high reflections, and instruments for monitoring power level and frequency. The power meters were calibrated initially to give the power levels at the switch.

The two amplifiers in the receive line have a total gain of over 40 dB and a net noise figure of 3.5 dB. A band stop filter with center frequency at  $f_T$  is included since the transmit signal is not attenuated sufficiently by the triplexer to prevent saturation of the second amplifier. The spectrum analyzer was set at a bandwidth of 1 kHz which was swept through a 100-kHz range. Its 1F gain was set at 60 dB. The addition of an integrator and recorder provided additional sensitivity and a permanent record. The calibration of the recorded signals was obtained by replacing the switch with a generator with its frequency set to that of the IM being measured. The output of this generator could be adjusted to as low as –145 dBm within 2 to 3 dB. Signals as weak as –140 dBm could be routinely detected on the recorder.

The switch was located in a chamber with a controllable temperature and a thermocouple was mounted on the switch to monitor its temperature. Considerable precaution was taken in this setup to assure that IM recorded originated from the diode alone. Contacts were carefully inspected and kept clean. The fact that the IM could be reduced below –140 dBm by adjusting the diode bias gave assurance that all other components were satisfactory. A photograph of the complete equipment arrangement is shown in Fig. 50.

Four variable parameters are relevant to the IM measurements: the transmit power  $p_T$  which is nominally 25 watts (44 dBm) at each diode in normal satellite operation; beacon power  $P_B$  nominally 1 watt (30 dBm) at each diode; the bias nominally 100 V or 50 mA; and temperature. Although the operating temperature is not specified, except that it has lower and upper limits of –40°C and +60°C, we take as the nominal value the average,  $T = +10^\circ\text{C}$ . The diode IM was measured as a function of one or two of these parameters while the others were held at the nominal values.

Figure 51 shows photographs of the spectrum analyzer display for a 2-mil diode at four reverse bias levels. The pass band of the triplexer is evident by the increased background level of noise. At the low bias of 50 V, the IM are highest in amplitude with all orders 15th to 25th visible (going left to right) as well as some of the 13th and 27th. The IM generally decrease in amplitude with increasing order, but as we see, there are some exceptions. As the bias is increased, the IM levels decrease until they are lost in the noise, which in these displays is about –128 dBm in intensity.



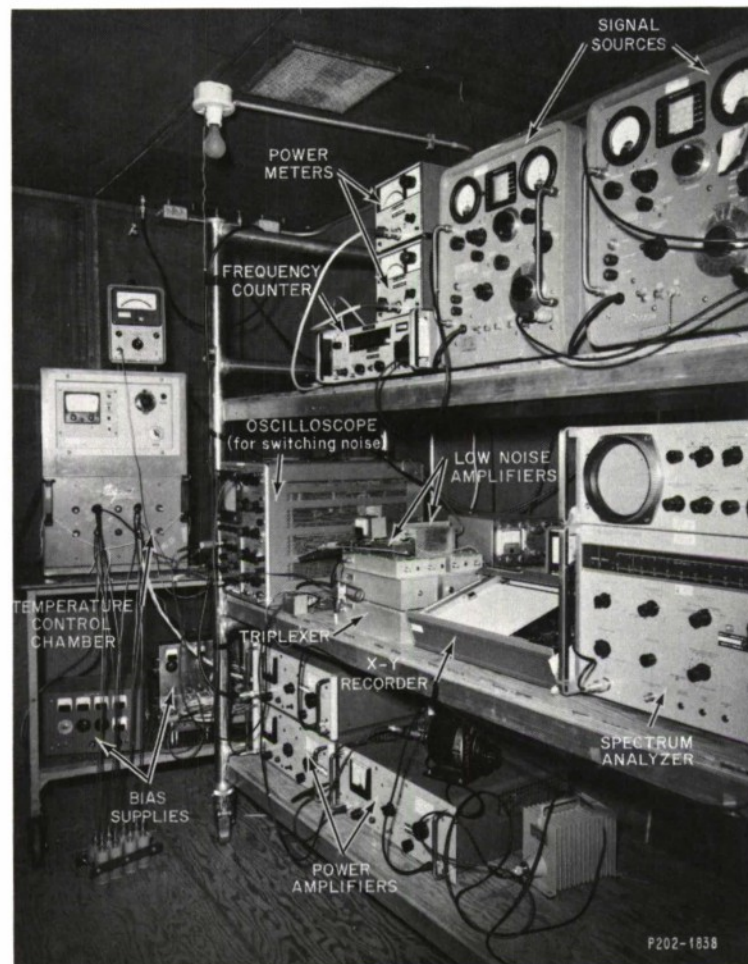
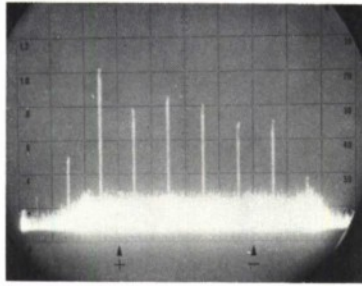
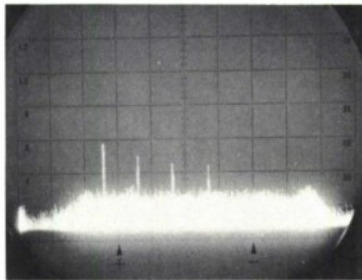


Fig. 50. Photograph of system for measuring IM amplitudes.

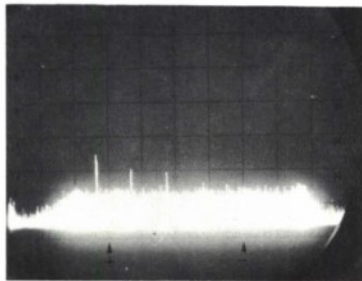
-63-7391-1



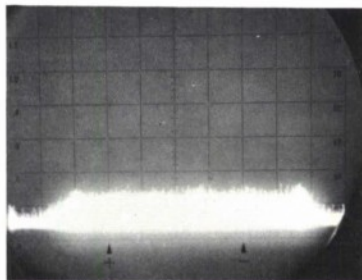
$V_R = 50V$



$V_R = 60V$



$V_R = 70V$



$V_R = 80V$

Fig. 51. Oscilloscope traces of signal spectrum emanating from SPST unit with 2-mil diode shunting main RF line;  $P_T = 47$  dBm,  $P_B = 33$  dBm. (RFI band is distinguished by increased noise level.)

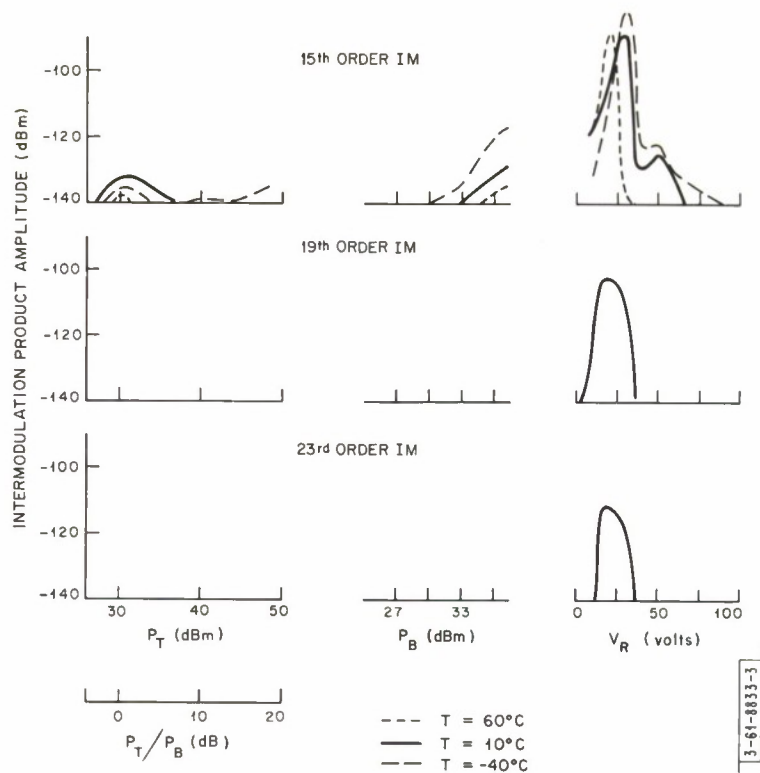


Fig. 52. IM dependence on  $P_T$ ,  $P_B$ ,  $V_R$ , and  $T$  for a 3-mil diode. When one parameter is varied, others are held at nominal values, namely,  $P_T = 44$  dBm,  $P_B = 30$  dBm and  $V_R = 100$  V.

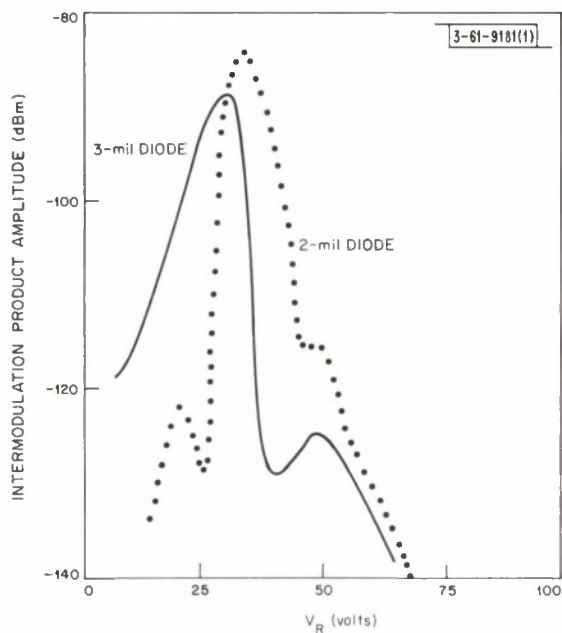


Fig. 53. Comparison of 15th order IM of typical 2- and 3-mil diodes;  $P_T = 44$  dBm,  $P_B = 30$  dBm and  $T = 10^\circ\text{C}$ .

Figure 52 shows the measured amplitudes of the IM for a typical 3-mil diode as a function of  $P_T$ ,  $P_B$  and  $V_R$ . (An example of the type of plot obtained on the recorder is shown in Fig. 58, Sec. VII-C.) The 15th order, which is plotted at the top, was measured at  $-40^\circ\text{C}$ ,  $+10^\circ\text{C}$  and  $+60^\circ\text{C}$ , the 19th and 23rd for  $+10^\circ\text{C}$  only. The second scale, the ratio  $P_T/P_B$ , was added to the plots involving  $P_T$ , since this ratio is significant, although here  $P_B$  remains fixed at 1 watt. In this figure, as well as in Figs. 53 through 57, when one parameter is varied the others are held at nominal values.

Some observations are that, in general,

- (1) The higher order IM have lower levels – they could not be observed at all as indicated in four of the plots,
- (2) IM increases with decreasing temperature,
- (3) IM exhibits a peak as a function of  $P_T$  or  $V_R$ ; a peak is evident where  $P_T = P_B$ ,
- (4) IM increases with  $P_B$  over the range plotted in the figure.

Similar plots for a 2-mil diode are published elsewhere<sup>15</sup> in more detail. Although the parameters used are slightly different, the trends are like those of the 3-mil diode, but peaks in the IM occur at higher bias voltages. Figure 53 provides such a comparison. The 2-mil diode exhibits higher IM at higher biases with differences as great as 20 to 30 dB. Measurements of IM for the 3-mil diode on forward bias failed to produce any observable values at biases from 10 to 50 mA as a function of the various parameters of power and temperature. The 2-mil devices, on the other hand, exhibited IM power levels of up to  $-100\text{ dBm}$ .

A more interesting graph is shown in Fig. 54. It is a map on a  $P_T - V_R$  plane showing contours of constant IM amplitude of the 15th order for the 3-mil diode at  $+10^\circ\text{C}$ . We see a main peak with an amplitude of over  $-90\text{ dBm}$  running diagonally upwards to the right. At the nominal power  $P_T$  of  $44\text{ dBm}$ , the bias must be set at  $60\text{ V}$  or higher for the IM to be below  $-130\text{ dBm}$ . The IM is also low at a low bias, but the margin is small; that is, a small decrease in  $P_T$  results in a rapid increase in the IM. Also, there are differences from diode to diode and many do not have this low value. These IM characteristics were the justification for using a bias of  $100\text{ V}$  for the normal operating voltage for the flight switch matrix. Interestingly, in Fig. 54 a minor peak also exists along the line  $P_T = P_B$ .

Other contour plots are given in Figs. 55, 56 and 57. Figure 55 is a map for the 3-mil diode with the beacon rather than the transmit power as the one variable. Its only distinctive feature is the general increase in level with  $P_B$ . Figure 56 is again the  $P_T - V_R$  map for the 3-mil diode

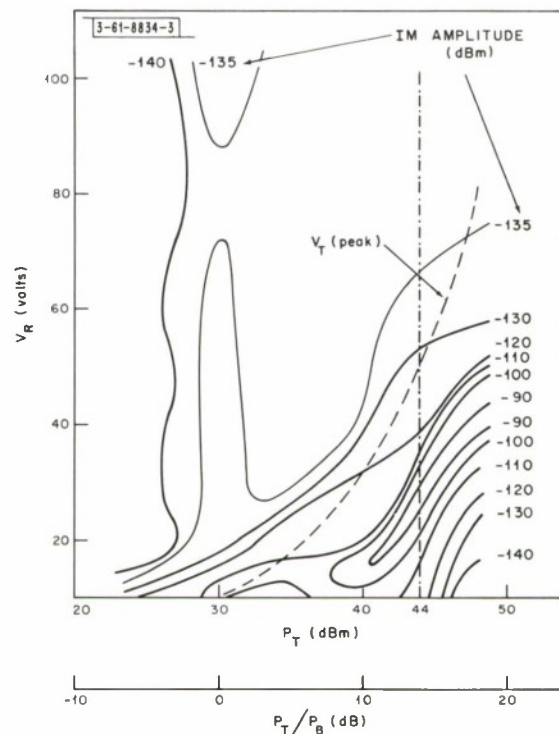


Fig. 54. Contours of constant 15th order IM on  $P_T - V_R$  plane for 3-mil diode;  $P_B = 30\text{ dBm}$  and  $T = 10^\circ\text{C}$ .



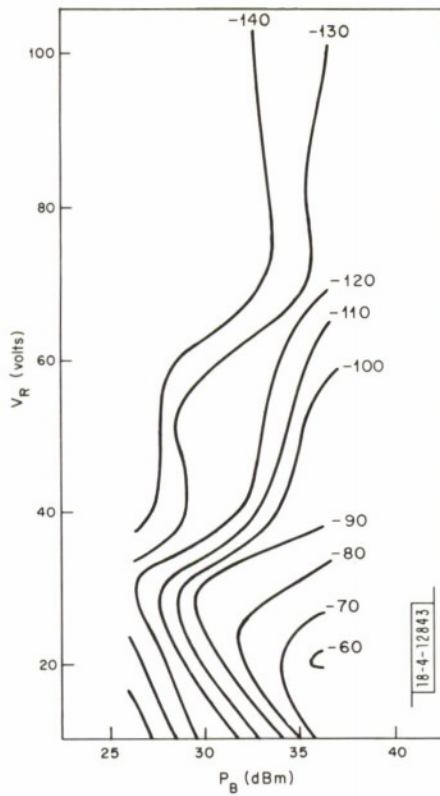


Fig. 55. Contours of constant 15th order IM on  $P_B - V_R$  plane for 3-mil diode;  $P_T = 44$  dBm and  $T = 10^\circ\text{C}$ .

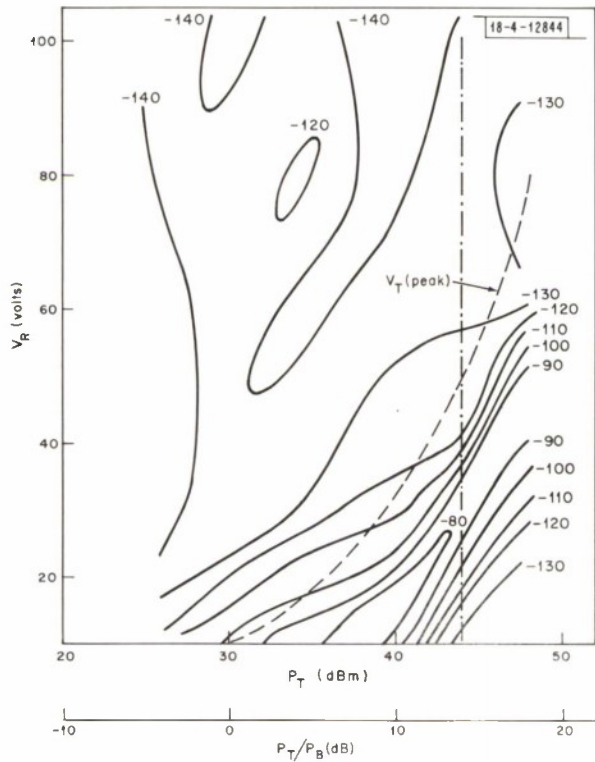


Fig. 56. Contours of constant 15th order IM on  $P_T - V_R$  plane for 3-mil diode;  $P = 30$  dBm,  $T = -40^\circ\text{C}$ .

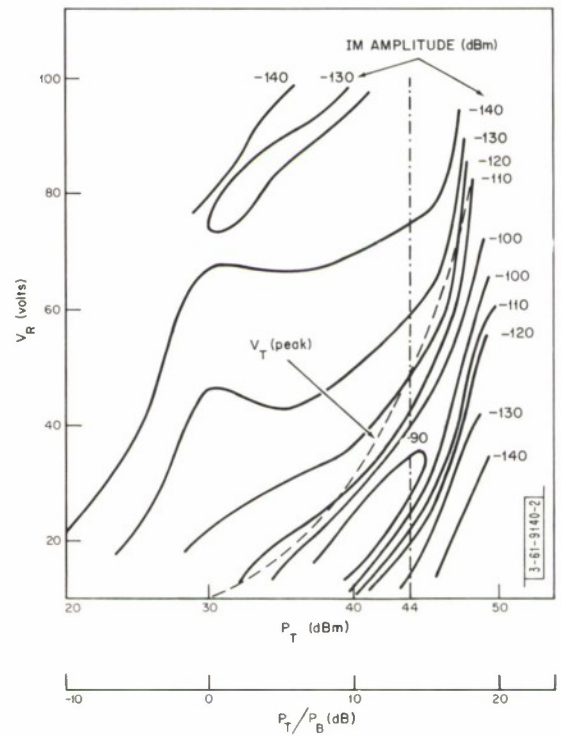


Fig. 57. Contours of constant 15th order IM on  $P_T - V_R$  plane for 2-mil diode;  $P_B = 30$  dBm,  $T = 10^\circ\text{C}$ .

but at a temperature  $T = -40^\circ\text{C}$ . It is much like the plot for  $T = +10^\circ\text{C}$  but with levels generally higher. Figure 57 is the  $P_T - V_R$  map for the 2-mil diode at  $T = +10^\circ\text{C}$ . We note now that the diagonal peak of the IM lies at a higher bias  $V_R$  than it did for the 3-mil diode.

It is difficult to understand why the IM has the character shown in these graphs. It is related to the dynamic capacitance-voltage characteristics of the reverse-biased PIN diode such as shown in Fig. 8. These capacitance measurements of both the 2- and 3-mil diodes, which were carried out with a small RF signal, showed a higher degree of nonlinearity at lower bias levels and would indicate a higher IM level. At sufficiently low bias levels, however, the diode is forward driven by the normally high RF signal and the prediction by a small signal measurement ceases to be accurate. In the contour plots is a dashed curve labeled  $V_T(\text{peak})$ . This curve indicates where the peak RF voltage equals the bias voltage. Its significance is that it provides an indication of how much of the nonlinear characteristic of the diode the combined voltage sees. Notably, the peak in the IM in all cases roughly parallels this curve.

The difference in IM and capacitance between the 2- and 3-mil diode reflects the difference in charge configuration of the diodes. Why this difference exists is not clearly understood, except possibly the thinner l-layer makes the diode look more like it has a graded junction. Figure 8 shows that the 3-mil diode exhibits a distinct "punch-through" voltage of about 20 V where the diode changes from a nonlinear to a linear characteristic. Above the punch-through voltage, the l-layer is swept free of charge carriers. No such voltage is distinctive in the 2-mil diode. This difference could be a reason that the IM of the 2-mil diode is higher at higher biases.

Relative to the input signal power levels, the maximum IM is very small (over 100 dB difference). The mechanism giving rise to the IM is subtle and the effect of bias on the RF characteristics such as insertion loss and VSWR is very slight in the range of parameter values referred to in the figures as verified by experiment. (The most pronounced effect was in the change in operating temperature, as discussed in Sec. V.) The effect would be small since the charge storage time of the diode is too long compared to the signal period to affect the charge configuration.

Not evident in the graphs is that riding on the general trends exhibited is considerable fine structure. The plots were joined by smooth curves, but an observation of the IM on the spectrum analyzer cathode ray tube reveals small rapid up-and-down variations riding on the gross change as the bias or power level is varied. This may arise from the interaction of the IM and harmonics generated and the RF impedances of the experimental setup as mentioned in Sec. VII-A. However, varying the length of line joining the switch to the triplexer showed no effect on the gross IM characteristics. A more peculiar effect occurring with some diodes is that a smaller second peak appears just beside the main peak as the bias voltage is increased. No explanation for this behavior is available at this time.

In general, the 2-mil diodes exhibited higher IM amplitudes at higher reverse bias levels and at all forward bias levels than the 3-mil diodes. For example, for a reverse bias of 80 V and normal RF power levels, in a random sample of 24 2-mil diodes, the 15th order IM of 7 exceeded  $-127\text{ dBm}$ . In a random sample of 43 3-mil diodes, the number was 1. These points were the justification for using 3-mil diodes. Of 76 diodes purchased to supply the flight switches, the 15th order IM of 3 lay between  $-130$  and  $-135\text{ dBm}$ , 7 lay between  $-135$  and  $-140\text{ dBm}$ , and the remaining were less, with normal operating parameters.

Two other precautions were also taken with regard to the IM. The reverse bias was chosen at 100 V. Although the nominal beacon power in the satellite is 2 watts (1 watt at each diode), it was originally set at 5 watts, but later reduced because of the IM concern in general.

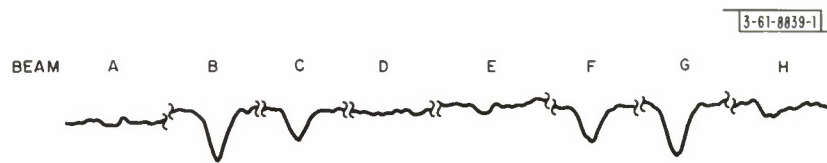


Fig. 58. Typical recordings of IM of switch matrix for eight beam positions.

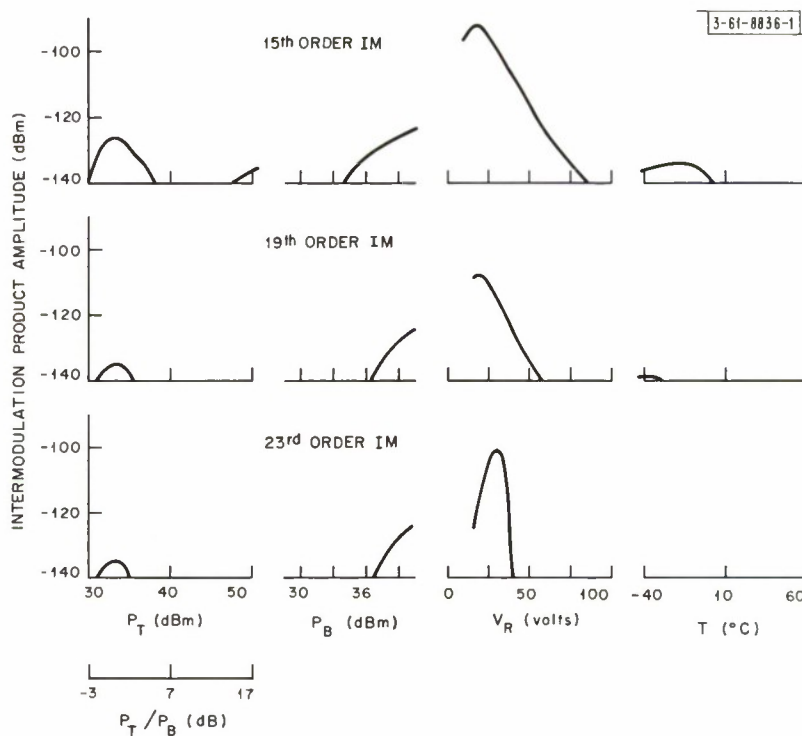


Fig. 59. IM dependence on  $P_T$ ,  $P_B$ ,  $V_R$ , and  $T$  for hybrid switch matrix combination used with dipole antennas on satellite. When one parameter is varied, others are held at nominal values, namely,  $P_T = 47$  dBm,  $P_B = 33$  dBm,  $V_R = 100$  V,  $I_F = 50$  mA, and  $T = 10^\circ\text{C}$ .

### C. Intermodulation Products Generated in Switch Matrix

The IM of a switch matrix depends not only on the operating parameters but also on which of the sets of 16 states the 12 diodes are in, corresponding to the 16 antenna beam positions. Many measurements were made on switches in both the course of development and final testing, for all 16 beam positions. A few of the more significant results are given in this section for only the states of the diodes corresponding to the first few beam positions. The values shall be labeled according to the beam, i.e., beam A, beam B, etc. The complete characteristics of the flight switches are listed in Appendix A.

Each switch matrix was evaluated in the same equipment setup as that used for the SP2T switches (Fig. 49). Each was connected with a hybrid as in Fig. 5(a) and terminated in eight matched loads. All the test components involved were checked to be IM free; the IM observed was generated only by the diodes. The nominal RF power levels at the hybrid input are now double (or increased 3 dB) those used for the SP2T switch measurements.

The first significant IM measurements were on a switch matrix with the early design of the 2P2T section shown in Fig. 22(b). Its values for the 15th order were found to be  $-118$  dBm,  $-124$  dBm,  $-122$  dBm,  $-118$  dBm,  $-121$  dBm... for beams A, B, C, D, E... respectively. These values were too high to be acceptable and were seemingly not in line with the values obtained with the SP2T switch. A measurement was made of the switch matrix without the hybrid and with one input port terminated. The RF signals, applied to the other input port, were set at 3 dB less. The IM now measured  $-136$  dBm at the most.

It was then apparent that the circuit of the switch matrix somehow altered the IM levels generated by the diodes. An investigation revealed the high RF voltage across diode j or k as explained in Sec. III-B. It was then necessary to redesign the switch matrix keeping the diodes as close as possible to the junction. In the 2P2T section, the minimum distance is limited by the capacitor and the metal block used for heat dissipation. It would then be expected that the IM would always be higher than if the same diodes were measured in the SP2T switch where they are placed right at the junction. It also became evident that diodes with the lowest IM should be used for diodes j and k in the flight switches. One would now anticipate that measured IM of a switch matrix would really be the IM of diode j or k, whichever is on reverse bias, unless one or more of the other ten diodes is significantly poorer.

Another factor now enters the picture. The RF voltage across this diode, j or k, depends on the phases of the signals on the diode cathode and anode as well as on the amplitude. This in turn depends on the relative phase of the signals at the two inputs, or physically on the lengths of the two cables joining the switch to the hybrid. Hence, relative phase is another parameter influencing the IM of a switch matrix.

A typical recording of IM of a switch matrix is reproduced in Fig. 58 for beams A through H. On beams A, D, E, and H where diode j is on reverse bias, the IM is below the noise level ( $-140$  dBm) or barely discernible. Switching the reverse bias to diode k as in beams B, C, F, and G, the IM comes up prominently, albeit small (about  $-136$  dBm), which reflects the slightly poorer characteristics of this diode.

Fifteenth order IM levels of one of the flight switches (with 3-mil diodes) for beam A is plotted in Fig. 59 versus transmit power  $P_T$ , beacon power  $P_B$ , reverse bias  $V_R$ , and temperature  $T$  with the relative phase  $46^\circ$ . (The nominal values are  $P_T = 47$  dBm,  $P_B = 33$  dBm,  $V_R = 100$  V,  $I_F = 50$  mA, and  $T = +10^\circ\text{C}$ .) These characteristics are basically those of diode j interacting with the switch circuit and are similar to the ones of Fig. 52 but with higher levels.



The effect of phase is illustrated by the measurement of a switch at two relative phases,  $46^\circ$  and  $63^\circ$ , the approximate satellite values for the slot switch and dipole switch, respectively. The temperature was reduced to  $-40^\circ\text{C}$  to make the IM more prominent but the other parameters were maintained at the nominal values. At  $46^\circ$ , the IM measured  $-138\text{ dBm}$ ,  $-131\text{ dBm}$ ,  $-133\text{ dBm}$ ,  $<-140\text{ dBm}$ ,  $-138\text{ dBm}$ ...for beams A, B, C, D, E... At  $63^\circ$ , the values were  $-133\text{ dBm}$ ,  $-127\text{ dBm}$ ,  $-126\text{ dBm}$ ,  $-132\text{ dBm}$ ,  $-132\text{ dBm}$ ... The average difference is about 5 dB.

The effect on the signal received within the RFI band of IM emanating from the switch could be displayed by replacing the spectrum analyzer by a detector and oscilloscope. The switch was cycled through the 16 beam positions as on the satellite and the bias reduced to 25 V to exaggerate the IM. The display is shown in Fig. 60. The noise adopts a different position for each beam depending on the IM amplitudes. Each level results from the combination of all orders of IM in the RFI band.

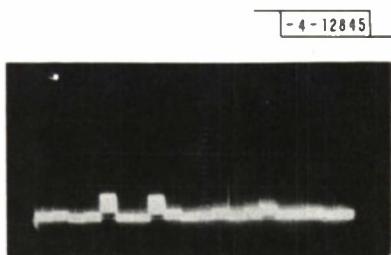


Fig. 60. Signal (in time domain) that would enter receiver if switch matrix generated high IM as it switches normally. IM was increased by reducing bias to  $V_R = 25\text{ V}$ .

Finally, with the switches installed in the satellite, the satellite receiver system was checked out to determine whether it had the anticipated sensitivity. This measurement would indicate whether the switches would degrade the system operation as well as bring to light IM-generating points in the RF system, such as imperfect contacts. It was found that the switches did not reduce the system sensitivity in any measurable way despite the fact that the IM was measured in the SP2T switch and complete matrix in a setup which had different impedance characteristics, and the signal generators used supplied single frequency signals.

## VIII. SWITCHING NOISE

### A. PIN Diode

When an RF peak detector with a time constant of several microseconds was used in place of the spectrum analyzer in the circuit of Fig. 49, a voltage pulse appeared at its output each time the switch under test was switched. For example, a switch matrix was sequenced through the 16 beam positions by a bias driver cycling at about the same rate that the switch is driven on the satellite. Such a signal from the detector as displayed on an oscilloscope is shown in Fig. 61. Some of the pulses are quite prominent such as those between beams C, D, and E.

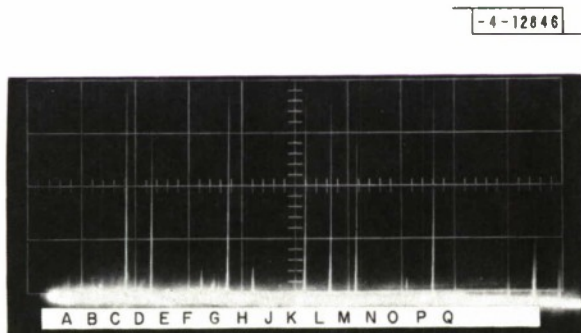


Fig. 61. Burst of noise generated in switch matrix each time it switches.

Others seem to be below the noise level as, for example, between A and B. An unusual aspect of these pulses is that they varied in amplitude at random from one switching to the next. Figure 61 is an exposure involving 15 sweeps of the oscilloscope so the intensity of a pulse is an integration of different amplitudes.

In an effort to characterize, understand, and control these noise pulses, measurements were made using the SP2T switch. The bias state of the two diodes was alternated by a square wave signal, with one diode ON while the other was OFF. A more accurate representation of the pulse could be put on display by shifting its frequency spectrum to where it could be observed on a conventional oscilloscope.

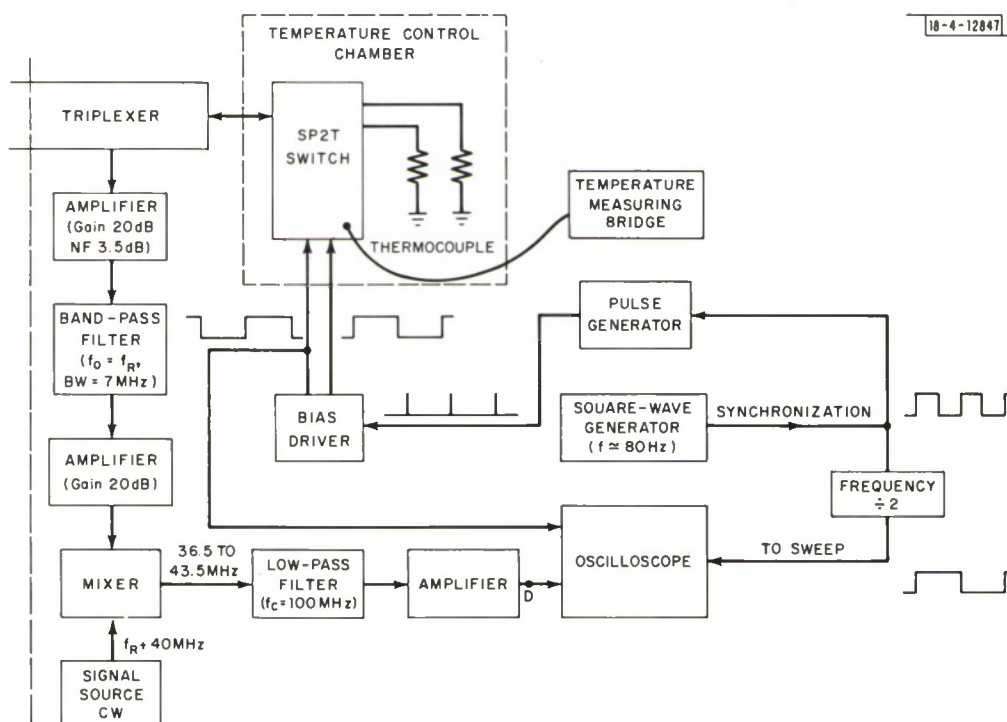


Fig. 62. System for measuring switching noise amplitude of SP2T switch. This circuit replaces circuit after triplexer shown in Fig. 49.

The measurement setup is shown in Fig. 49 but with the receiver circuit replaced by that shown in Fig. 62. The bandstop filter used in the IM measurement between the receive amplifiers is replaced by a bandpass filter with a bandwidth of 7 MHz centered at the receive frequency in order to simulate the transponder operation in the satellite. The signal is reduced in frequency to 40 MHz by use of a mixer driven by a local oscillator, and is then applied to an oscilloscope. Also utilized was a square wave generator set at an 80-Hz rate which simultaneously synchronized the bias driver of the switch and the oscilloscope. The system was calibrated by injecting a 1- $\mu$ s long RF pulse of known amplitude into the cable normally tied to the switch and observing the amplitude on the oscilloscope.

Figure 63(a) shows, with simulated transmit and beacon signals applied to the SP2T switch, a trace of the bias waveform on one diode (this signal is inverted to that shown in Fig. 6) and the RF signal in the 7-MHz band at the moment the switch is triggered. The scale is 1  $\mu$ s per major

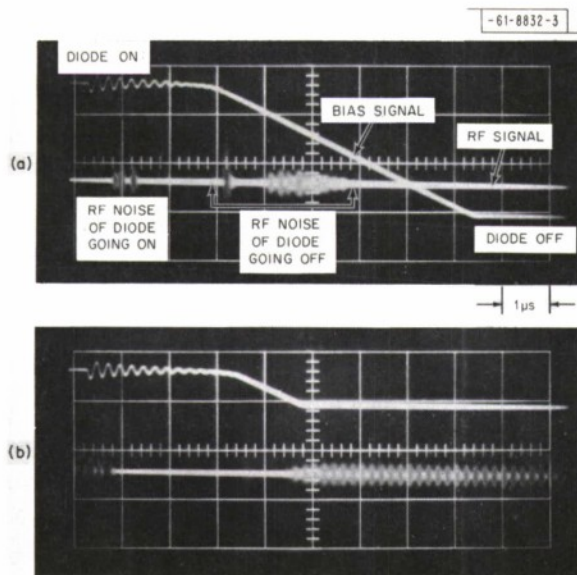


Fig. 63. Bias and RF signals during switching transient.  $P_T = 44$  dBm,  $P_B = 36$  dBm,  $I_F = 50$  mA,  $T = -40^\circ\text{C}$ . (a)  $V_R = 80$  V. (b)  $V_R = 20$  V.

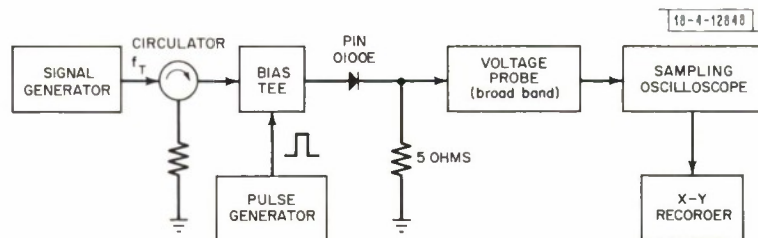


Fig. 64. System for observing RF signal transmitted through PIN diode as bias pulse is applied.

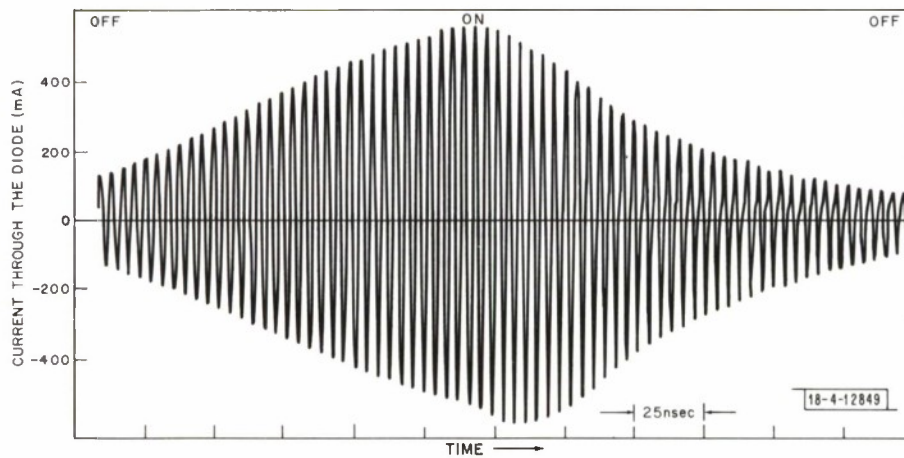


Fig. 65. Recording of RF signal current through 2-mil diode as bias pulse is applied; frequency =  $f_T$ .



division. The RF signal is characterized by noise bursts having several components, some associated with one diode turning ON and some associated with the other turning OFF. For the turning OFF case, for which we see the bias waveform in Fig. 63, the switch bias driver is approximately a constant current source. The initial oscillation is due to the natural resonant frequency of the bias circuit as loaded by the diode. The voltage remains constant for a few microseconds – the diode is clamped – while the stored charge is being depleted. The length of time in this state is related to the minority carrier lifetime (which is some 2 to 4  $\mu$ s) and the discharging by the reverse bias current source. At the same time, there is sufficient stored charge to prevent the RF signals from depleting it in the negative half cycles. A point is reached eventually when the stored charge is small enough for negative half RF cycles to fully and abruptly deplete the charge. The ensuing positive swing causes some rectification resulting in the large spike of signal voltage. Then, as the diode bias approaches the level of maximum intermodulation generation, the signal burst has a characteristic 5-MHz repetition frequency which is due to rectification of the beats between the transmit and beacon signals. This fact is more vividly illustrated in Fig. 63(b) in which the OFF state bias level has been reduced to the point where maximum IM generation occurs and the 5-MHz beat continues through the steady state. It is now apparent why the noise burst varies in amplitude each time the diode is switched. This amplitude would depend on the instantaneous amplitude of the rectified signal at the moment the noise burst would be generated.

It is also interesting to actually look at the RF signal on a sampling oscilloscope during the switching transient. The circuit arrangement of Fig. 64 enabled us to do this. A single source provided a signal at frequency  $f_T$  and power  $P_T = 7.5$  watts (to a matched load). The diode held on reverse bias in the steady state is driven into forward bias for about 0.2  $\mu$ s with a pulse generator. An RF signal picked up by a voltage probe is processed by the sampling oscilloscope and recorded. The signal on the probe is the voltage across a 5-ohm thin-film microwave resistor mounted in coaxial line in series with the diode and hence represents the RF current in the diode.

A recorded signal is given in Fig. 65 for a 2-mil diode. We see how the RF signal changes with the application of the bias pulse first in increasing then decreasing amplitude. The diode never becomes fully forward biased – the pulse turns it off before the current reaches a constant value. The region of interest of the sinusoidal waveform is just after the diode is switched off. The charge stored in the junction under forward bias is depleting and when the injected charge on the positive half cycles reaches a given value, a break occurs in the waveform (evident in the trace at about 40 mA) signifying the onset of rectification and nonlinear operation. Graphical integrations carried out in this region show that the ratio  $Q^+/Q^-$  is as high as 1.19 where  $Q^+$  and  $Q^-$  are the charges in the positive and negative half cycles respectively. This indicates then that there is some loss in charge due to the rectification of the RF signal. This experiment confirms the mechanism for generation of the spike noise that is observed.

Figure 66 shows a number of graphs of maximum amplitude of the switching noise signals observed for a 3-mil diode as a function of  $P_T$ ,  $P_B$ , and  $I_F$ . There are two sets for the two cases, OFF to ON and ON to OFF, and each plot has three curves for the three temperatures:  $-40^\circ\text{C}$ ,  $+10^\circ\text{C}$ , and  $+60^\circ\text{C}$ . Some definite observations can be made, namely,

- (1) The noise amplitudes are considerably higher than the IM amplitudes but generally last only a fraction of a microsecond.
- (2) The pulses are quite temperature dependent, the higher amplitudes corresponding to lower temperatures.
- (3) The ON to OFF amplitude peaks where  $P_T = P_B$ .



- (4) When only one of the RF signals is present, the amplitudes are still significant; introducing the second signal increases the noise substantially indicating an intermodulation or rectification effect coming into play.

There are no graphs showing how the noise amplitude varies with  $V_R$  since it was found to have little effect.

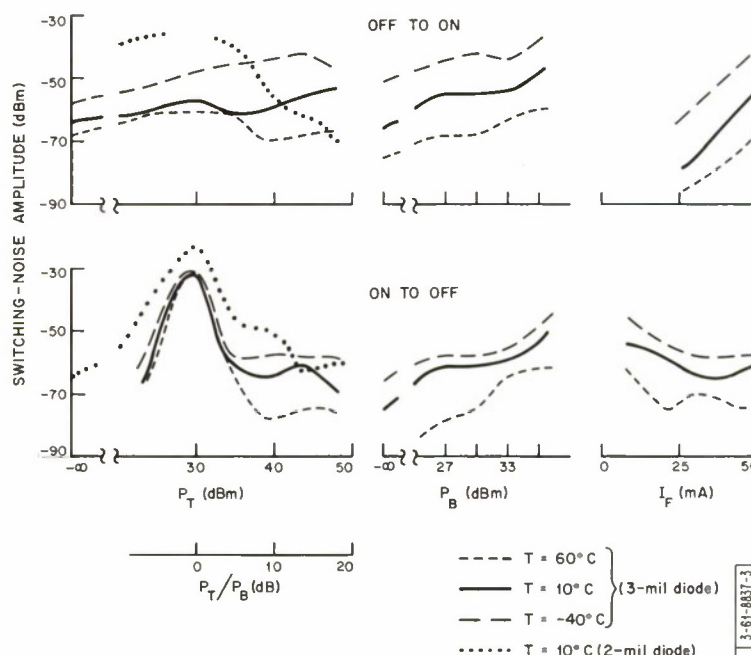


Fig. 66. Switching noise dependence on  $P_T$ ,  $P_B$ ,  $I_F$ , and  $T$  as measured in SP2T switch. When one parameter is varied, others are held at nominal values, namely,  $P_T = 44$  dBm,  $P_B = 30$  dBm,  $V_R = 100$  V and  $I_F = 50$  mA.

Included in the graphs are plots for a 2-mil diode with its dependence on  $P_T$ . It can be seen that the switching noise is generally 10 to 20 dB higher, another reason for using 3-mil diodes. There is a break in the OFF-to-ON curve due to the pulse being swamped by the ON-to-OFF noise of the other diode.

The time duration of the pulses above  $-90$  dBm fell between  $0.2$  and  $0.3 \mu\text{s}$  in all cases except when the power  $P_T$  was varied. As Fig. 67 shows, the ON-to-OFF pulse width increases to about  $1.0 \mu\text{s}$  at low values of  $P_T$ . For the 2-mil diode, this increase is to several microseconds.

We have not mentioned earlier that the amplitudes also depend on the shape of the bias waveform at the moment the noise is generated. The effect of bias indicated in Fig. 66 exists only insofar as this shape is changed. In the ON-to-OFF case, for a constant current source, the shape is dependent only on the characteristics of the diode as explained above. On the other hand, in turning OFF to ON, the rate of voltage change which decides the noise amplitude depends on the bias driver and the circuit which separates the bias and RF signals. The addition of the ferrite coil (Sec. II-F) had the effect of increasing the fall time of the voltage and hence reducing the noise burst a desirable amount. The graphs of Fig. 66 are applicable to a particular bias driver and the switch circuit of Fig. 40 (with the ferrite coil) and would differ under differing circumstances. However, the general conclusions still apply.

Another characteristic of interest is the spectral distribution of the noise burst. The above results pertained to the noise observed in a 7-MHz band centered at the receive frequency. In

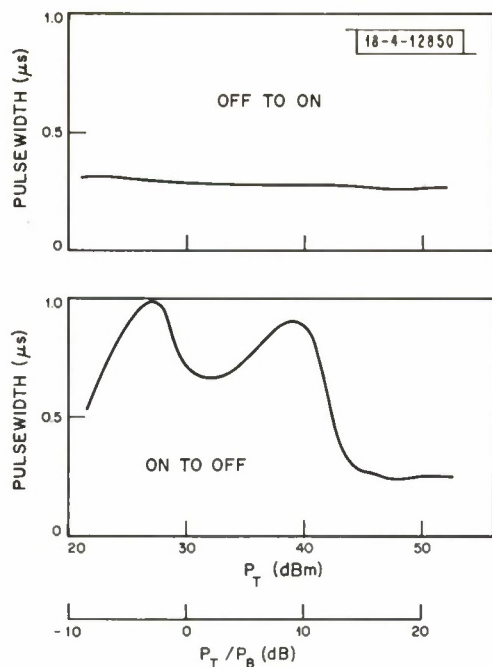


Fig. 67. Time duration of switching noise of 3-mil diode estimated from oscilloscope trace as a function of  $P_T$ ;  $P_B = 30$  dBm,  $V_R = 100$  V,  $I_F = 50$  mA, and  $T = 10^\circ\text{C}$ .

a separate measurement, the bandwidth was narrowed to 1 MHz and swept through the RFI band. Typically, the noise burst amplitude (as measured in dBm) decreased nearly linearly about 10 dB from the low frequency to high frequency end of the band. The values as observed with the setup of Fig. 62 are most representative of the situation in the satellite.

The 76 3-mil diodes purchased for the flight switches were all measured and evaluated. The distribution of their maximum value of switching noise amplitudes at the nominal operating conditions is plotted in Fig. 68. They ranged from  $-50$  dBm to lower than  $-90$  dBm with most falling between  $-70$  and  $-80$  dBm.

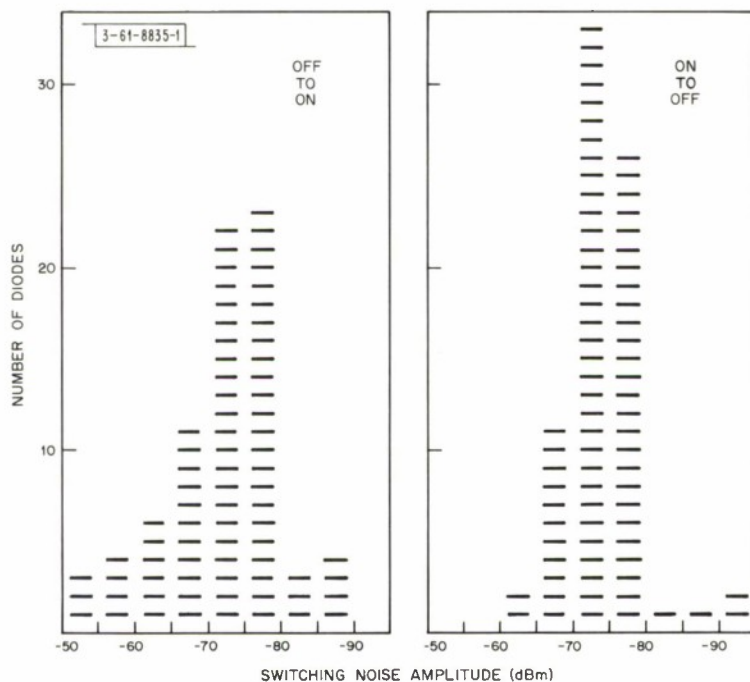


Fig. 68. Distribution of switching noise amplitudes of 76 3-mil diodes.  $P_T = 44$  dBm,  $P_B = 30$  dBm,  $V_R = 100$  V,  $I_F = 50$  mA, and  $T = 10^\circ\text{C}$ .

## B. Switch Matrix

For the measurement of the switching noise of a switch matrix, a bias driver was built to deliver a signal which would sequence the switch through the 16 beam positions continuously in a manner corresponding to that used on the satellite. However, with the setup of Fig. 62, it was not possible to observe the switching noise occurring in the transition between two beams, say A and B. The repetition rate was too low to leave a visible trace on the oscilloscope and therefore an RF peak detector employing a Schottky barrier diode was inserted between the RF amplifier and oscilloscope (at point D in Fig. 62). The pulses could then be observed and measured easily. An additional inaccuracy now enters the measurement for the detector output now depends on the pulse width as well as its height. The system was calibrated for a  $1\text{ }\mu\text{s}$  pulse. If in fact a pulse of  $0.25\text{ }\mu\text{s}$  duration is measured, its amplitude will be about 3 dB higher than the value obtained using the calibration. A  $4\text{-}\mu\text{s}$  pulse will have an amplitude 2 dB lower. In addition, the detector will receive a train of several pulses as several diodes in the switch matrix are being switched. The output will be that of the highest pulse affected by the time extent of the train. (A typical output of this system is shown in Fig. 61.)

A series of measurements was made on the same switch used to provide the curves of Fig. 59. The noise amplitudes are plotted in Fig. 69 for the three cases of switching from beam A to beam B, beam B to beam C, and beam C to beam D. The operating parameters are nominal as has been the case until now. For each point, only two or four diodes are involved. For example, in switching beam A to beam B, diodes k and l turn OFF and diodes j and m turn ON. The top set of plots of Fig. 69 then involves only these four diodes. Similarly, in switching beam B to beam C, only diodes a and b change state.

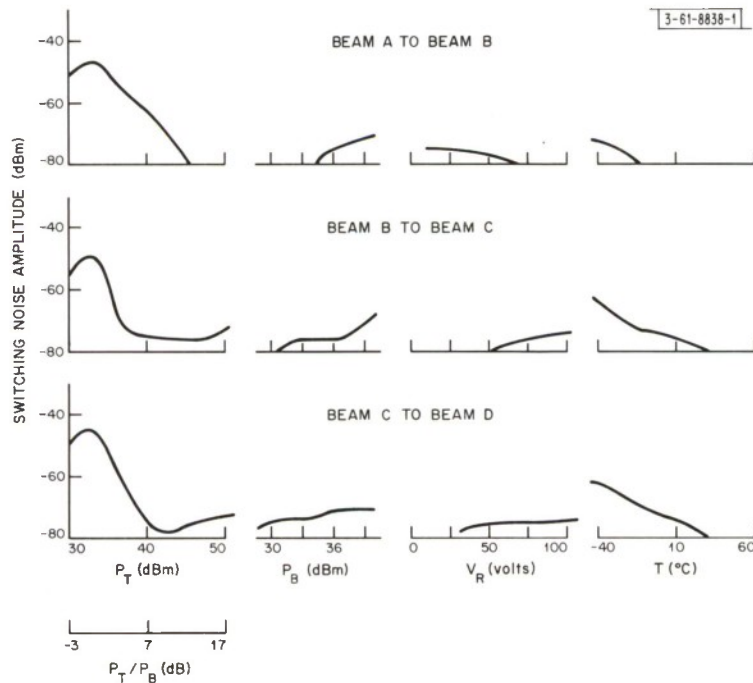


Fig. 69. Switching noise dependence on  $P_T$ ,  $P_B$ ,  $V_R$ , and  $T$  for hybrid-switch matrix combination used with dipole antennas on satellite. When one parameter is varied, others are held at nominal values, namely,  $P_T = 47\text{ dBm}$ ,  $P_B = 33\text{ dBm}$ ,  $V_R = 100\text{ V}$ ,  $I_F = 50\text{ mA}$ , and  $T = 10^\circ\text{C}$ .

The characteristics displayed by the plots of Fig. 69 are in line with those that would be expected from the diode alone. The fact that a higher RF voltage exists across diode j or k did not seem to have the pronounced effect on the switching noise level that it did on the IM level. The noise from diodes in the SP4T sections were often as high.

In the satellite, the noise bursts depend very much on the characteristics of the bias driver used as well as the characteristics of the antenna system and various other components. On the assembled flight satellite, the effect of the noise bursts on the rest of the system was investigated. The transponder was not affected at all. On the other hand, the peak-to-average measuring channel of the RFI instrument continually monitored the noise bursts as false readings. This problem was apparent at such a late date in the satellite program that it was impossible to apply corrective measures. For further development programs where such noise bursts exist, it is probably advisable to gate out the interfering signal to the extent necessary to eliminate its degrading effects on the system.

## IX. NOISE FIGURE

### A. Basic Aspects<sup>18,19</sup>

There was concern that the switch would degrade the noise figure of the satellite receiving system. As with the other tests, the noise figure was initially measured on SPST units with regard specifically to the PIN diode. This was followed by measurements of a switch matrix. Further consideration made it evident that the switch matrix could increase its noise figure when the transmit signal was applied. Therefore, the switch noise figure was examined under the two conditions, without and with 100 watts of incident power at one input port.

Let us briefly review the basic principles of the noise figure concept. This description shall be limited to the single frequency case rather than to frequency bands. Consider one or more amplifiers connected in tandem with total power gain  $G$  matched at both input and output to the same resistance. If the input and output signals are  $S_i$  and  $S_o$ , respectively, then

$$G = \frac{S_o}{S_i} \quad (68)$$

Suppose the noise input power  $N_R$  is that of a resistor at ambient temperature matched to the amplifier input. If the amplifier contributed no noise, the output noise power would be  $GN_R$ . In reality, the amplifier will contribute noise which we designate as equivalent to noise power  $N$  added at its input. The output noise is then

$$N_o = (N_R + N) G \quad (69)$$

The noise figure  $F$  is defined as the ratio of the input to output signal-to-noise ratio

$$F = \frac{S_i/N_R}{S_o/N_o} \quad (70)$$

Substituting Eqs. (68) and (69), we obtain

$$F = 1 + \frac{N}{N_R} \quad (71)$$

This equation may also have been used as the basic definition of noise figure. It has the advantage of excluding any reference to signals.



For a passive matched device with loss (represented by a value of  $G < 1$ ), the output noise must be the same as that of the resistor  $R$ ,

$$N_o = N_R \quad . \quad (72)$$

Equation (70) gives

$$F = \frac{1}{G} \quad . \quad (73)$$

For the general lossy device, we may then define excess noise

$$E = F - \frac{1}{G} \quad . \quad (74)$$

as an indication of the noise generated in addition to resistive noise.

A customary method of finding the noise figure is to measure the output noise by taking the input resistor  $R$  to two temperatures, one high and one low, in two consecutive tests. If the two output noises are  $N_{o1}$  and  $N_{o2}$  for two input noises  $N_{R1}$  and  $N_{R2}$ , then

$$N_{o1} = (N_{R1} + N) G$$

and

$$N_{o2} = (N_{R2} + N) G \quad . \quad (75)$$

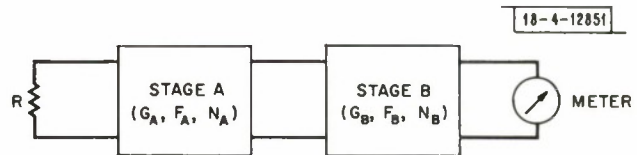
The gain is eliminated by dividing the two equations and solving for  $N$

$$N = \frac{N_{R1} N_{o2} - N_{R2} N_{o1}}{N_{o1} - N_{o2}} \quad . \quad (76)$$

The noise figure is then found by Eq. (71).

Usually, a measurement of the noise figure of a device requires amplifiers connected to the device output to raise the noise to a detectable level. To enable one to cancel out the noise contributed by the amplifier, the output noise is measured in the two steps where the device is absent

Fig. 70. Simple cascaded 2-stage system used for derivation of noise figure equations. Each stage has gain  $G$ , noise figure  $F$ , and equivalent noise power input  $N$ .



and present. Consider then the two stages in Fig. 70, with gains  $G_A$  and  $G_B$  and noise figures  $F_A$  and  $F_B$ , respectively. Let the stages be matched at both input and output to the same resistance value  $R$ . The equivalent input noises are

$$N_A = (F_A - 1) N_R$$

and

$$N_B = (F_B - 1) N_R \quad . \quad (77)$$

Because of the random nature of the noises  $N_A$  and  $N_B$  which are independent and approximately Gaussian distributed, the output noise is simply the sum of the noise terms. Thus

$$N_o = (N_R + N_A) G_A G_B + N_B G_B \quad . \quad (78)$$

The system noise figure  $F_{AB}$  can be found by Eq. (70) where

$$\frac{S_o}{S_i} = G_A G_B \quad (79)$$

Substituting Eqs. (78) and (79) into Eq. (70) and substituting Eq. (77) into the result, we obtain

$$F_{AB} = F_A + \frac{F_B - 1}{G_A} \quad (80)$$

Noise figures  $F_{AB}$  and  $F_B$  are found by measurement, and  $F_A$  is found from Eq. (80) which is known as the Friis formula. The excess noise is [from Eqs. (74) and (80)]

$$E_A = F_{AB} - \frac{F_B}{G_A} \quad (81)$$

In the measurement of the switch matrix with RF power applied, we need three stages A, B and C where B is the switch itself. Taking the gains as  $G_A$ ,  $G_B$ , and  $G_C$  and noise figures as  $F_A$ ,  $F_B$ , and  $F_C$ , respectively, the noise figure  $F_{ABC}$  of the combination is found in the same way as for the two-stage circuit. Thus

$$F_{ABC} = F_A + \frac{F_B - 1}{G_A} + \frac{F_C - 1}{G_A G_B} \quad (82)$$

The switch noise figure  $F_B = F_{B1}$  without the RF signal present is first found in the usual manner using the two-stage circuit of Fig. 70. If, then, in the three-stage system the system noise figures that are measured are  $F_{ABC1}$  and  $F_{ABC2}$  without and with an RF signal respectively, then we have two simultaneous equations. One is subtracted from the other and we solve for  $F_{B2}$  with the result

$$F_{B2} = F_{B1} + (F_{ABC2} - F_{ABC1}) G_A \quad (83)$$

Another consideration is the effect of mismatch on the noise figure. In all the measurements of noise figure, no stage is perfectly matched to some resistance value at either its input or output. Also, with two stages tied together, the reflections between them further complicate the noise figure calculation. If the noise figure of the switch matrix is known exactly, it still would not exhibit the same noise figure in the satellite because of the impedance characteristics of the other RF components joined to it. It is therefore impractical to concern oneself with the match in every component in each noise figure measurement. We might consider the effect of a single mismatch on the noise figure, however. Take for example the two-stage circuit of Fig. 70 where stage A has a reflection coefficient magnitude  $\Gamma$  at its input. Furthermore, assume that its noise  $N_A$  is not altered by the mismatch. The noise of resistor R is partially reflected and that portion entering stage A is  $N_R(1 - \Gamma^2)$ . The output noise is then

$$N_o = [N_R(1 - \Gamma^2) + N_A] G_A G_B + N_B G_B \quad (84)$$

Suppose now the procedure described earlier is followed, where the input resistor is varied in temperature to find an apparent noise figure  $F_{AB}$ . Then by Eqs. (71) and (76)

$$(F_{AB} - 1) N_R = \frac{N_{R1} N_{o2} - N_{R2} N_{o1}}{N_{o1} - N_{o2}} \quad (85)$$

Now,

$$N_{O1} = [N_{R1}(1 - \Gamma^2) + N_A] G_A G_B + N_B G_B$$

and

$$N_{O2} = [N_{R2}(1 - \Gamma^2) + N_A] G_A G_B + N_B G_B \quad . \quad (86)$$

Making the appropriate substitutions, we obtain

$$F_{AB} = 1 + \frac{1}{1 - \Gamma^2} \left( \frac{N_A}{N_R} + \frac{N_B}{N_R G_A} \right) \quad . \quad (87)$$

We now desire the true noise figure  $F_A$ . This is obtained by the definition, Eq.(70), applied to stage A alone. The ratio  $S_O/S_i$  is

$$\frac{S_O}{S_i} = (1 - \Gamma^2) G_A \quad (88)$$

(to conform with the form  $N_R(1 - \Gamma^2)$  of the noise entering the stage). Also

$$N_O = [N_R(1 - \Gamma^2) + N_A] G_A \quad . \quad (89)$$

Therefore, the noise figure is

$$F_A = 1 + \frac{1}{1 - \Gamma^2} \frac{N_A}{N_R} \quad . \quad (90)$$

The noise figure at stage B remains at

$$F_B = 1 + \frac{N_B}{N_R} \quad . \quad (91)$$

Substituting these last two equations into Eq.(87), we have finally

$$F_{AB} = F_A + \frac{F_B - 1}{(1 - \Gamma^2) G_A} \quad . \quad (92)$$

We see that the only change from the matched case, Eq.(80), is that  $G_A$  is replaced by  $(1 - \Gamma^2) G_A$ . However  $(1 - \Gamma^2) G_A$  is the gain, the ratio  $S_O$  to  $S_i$ , that one would measure if the reflection is not taken into account. It might be assumed that this is approximately true for a mismatch at any other point in the circuit.

The effect of mismatch may be indicated by an example. Consider  $G_A = 1$ ,  $F_B = 2.50$  (or 4 dB),  $F_{AB} = 2.56$ . When the VSWR is 1.5 ( $\Gamma = 0.2$ ), the value of  $F_A$  is 1 (or 0 dB). When the VSWR is 1.0, the value of  $F_A$  is 1.06 (or 0.26 dB). Thus, even with the large mismatch, the effect is generally insignificant for a receiver system.

## B. PIN Diode and SPST Unit

To measure noise figures, equipment was set up as in Fig.71. The noise source is a temperature controlled 50-ohm resistor whose noise power delivered to the switch is

$$N_R = kTB \quad (93)$$

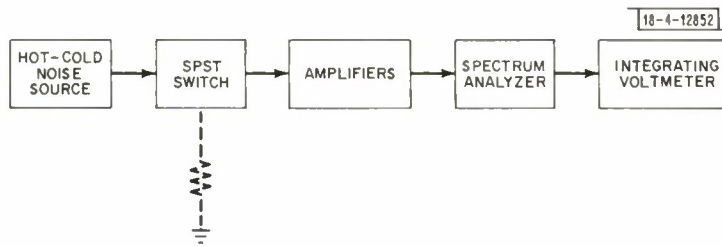


Fig. 71. System to measure noise figure of SPST switch.

where  $k$  is the Boltzmann constant and  $B$  the bandwidth. The temperature  $T$  is set at two values,  $77^\circ\text{K}$  and  $373^\circ\text{K}$ , by a liquid nitrogen bath and thermostat-controlled oven, respectively. The spectrum analyzer was used to limit the bandwidth to 10 kHz centered at the receive frequency. The amplifiers totalled more than 40 dB gain and spectrum analyzer provided another 60 dB gain. Without the switch, the system noise figure measured 3.1 dB [ $F_B$  of Eq. (80)].

Ten 3-mil diodes which had been subjected to the step stress test (Sec. XI-B) were measured in an SPST unit on both forward and reverse bias. For the forward bias of 50 mA (switch in series with the RF line), the noise figure proved to be approximately the same as the switch insertion loss ( $1/G$ ) within experimental error indicating that the excess noise as given by Eq. (74) is not measurable.

For the reverse bias case (switch as stub on the RF line), the noise figure apparently increases with the bias level. It is presumed that this increase comes about with the increase in leakage current. To illustrate, Fig. 72 is a plot of the measured noise figure versus the leakage current for the 10 diodes. There is a pair of points for each diode, for 100 V and 200 V bias, joined by a line to indicate the direction of the change with increasing bias. In five of the diodes there is an increase in noise figure with bias which seems to be greater with diodes of higher leakage current. The noise figure of one diode selected for its high leakage current (indicated by an arrow in Fig. 72), is plotted versus leakage current in Fig. 73. At lower values, the noise figure remains constant at about the insertion loss value, but swings upward when the leakage current exceeds  $100\mu\text{A}$ .

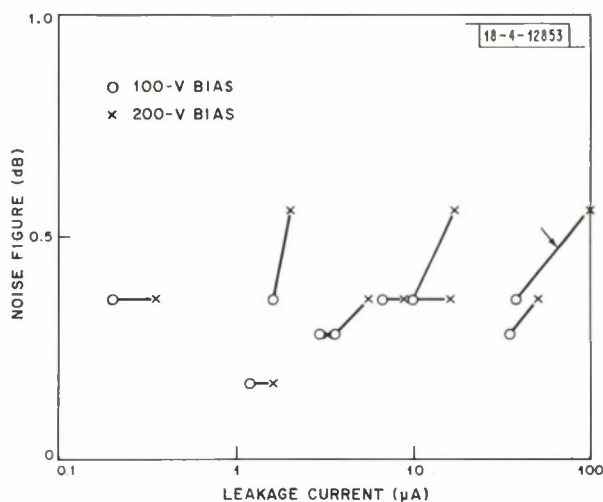


Fig. 72. Measured noise figures of ten 3-mil diodes on reverse bias as a function of leakage current.

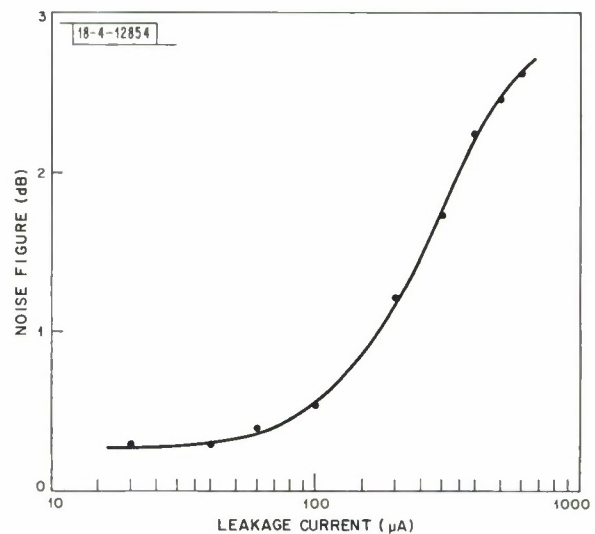


Fig. 73. Noise figure of 3-mil diode (indicated by arrow in Fig. 72) on reverse bias as a function of leakage current.



This characteristic provided a criterion for the acceptability of a diode for the satellite in the reliability tests described later. We may then consider a diode exhibiting a current exceeding say  $10\text{ }\mu\text{A}$  for 100 V bias unsuitable. This would be the "failure" criterion as described in Sec. XI. The ten diodes measured here were of substandard quality. Diodes going into the flight switches would be selected for high quality based on low leakage current, among other factors.

### C. Switch Matrix

The noise figure of a flight switch was measured. The 3-dB hybrid was omitted and one of the two input ports connected to the amplifiers. One output port was tied to the hot-cold noise source, and the diode biases set so that the RF connection was from the noise source to the amplifiers. The remaining eight ports were terminated in matched loads. This arrangement does not exactly represent the satellite configuration but offered a straightforward measurement and the result would be expected to be accurate nonetheless. It was found that the noise figure approximately equalled the insertion loss (about 0.4 dB), and the excess noise is thus small.

Another matter of concern was the increase in noise figure when the RF power is applied. To carry out this test, the RF signal has to be applied to the switch, but kept isolated from both the noise source and amplifiers. To accomplish this, two triplexers are used, one on each side of the switch. The complete circuit now has the layout shown in Fig. 74. The noise signal and RF signal are separated on both sides of the switch by the two triplexers and diverted to appropriate equipment.

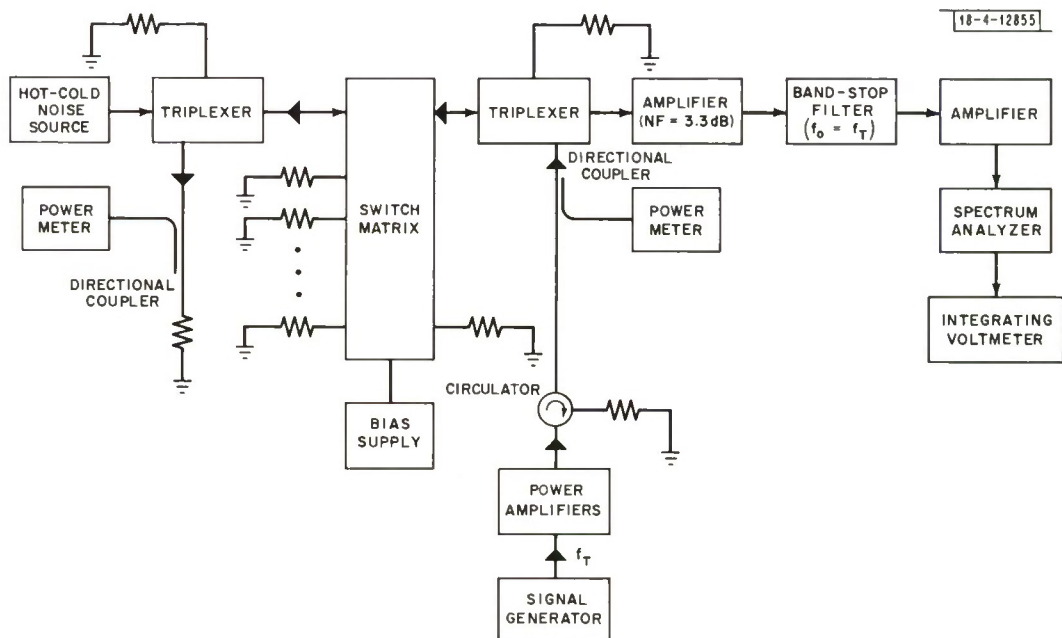


Fig. 74. System for measuring noise figure of switch matrix carrying RF power. Filled-in orrowheads give poth of RF signal. Noise from hot-cold noise source to voltmeter is traced by open orrowheads.

The noise figure of the system was measured for four different switch positions, that is, for different input and output connections and corresponding beam positions. The noise figure was found in each case with no RF signal and with a 100-watt signal. The 100-watt signal was four times the normal input power, which increased the noise figure enough to permit measurement.

TABLE VI NOISE FIGURE OF SWITCH MATRIX CARRYING 100 WATTS OF RF POWER						
Input at Diodes	Output at Diode	Beam	$F_{ABC1}$ ( $P_T = 0$ W)	$F_{ABC2}$ ( $P_T = 100$ W)	$F_{B2}$	$F_{B2}$ (dB)
l and m	a	A	3.435	3.772	1.42	1.52
l and m	e	C	3.617	3.907	1.38	1.40
j and k	d	O	3.545	3.966	1.50	1.76
j and k	h	Q	3.428	4.027	1.65	2.17

The measured values together with the calculated noise figures are given in Table VI. Equation (83) is used where we take  $F_{B1} = 1.12$  (or 0.50 dB) and  $G_A = 1/1.12$  (the triplexer). We see that the noise figure increase, and therefore the excess noise increase, runs from 1 to  $1\frac{1}{2}$  dB and depends on the switch beam position. In the normal satellite operation, the increase may be about half this value.

## X. EFFECT OF RADIATION DOSAGE IN ORBIT

The primary radiations at synchronous altitude above the Earth are the geomagnetically trapped electrons and protons and the solar flare protons which occur sporadically at times of intense solar activity. Other types of radiation such as galactic cosmic rays and gamma rays are negligible in comparison. The average particle fluxes at the intended satellite orbit are approximately  $10^8/\text{cm}^2/\text{sec}$  for protons in the 0.1 to 5 MeV energy range and drop below  $10/\text{cm}^2/\text{sec}$  for energies above 30 MeV. The flux of electrons is  $10^8/\text{cm}^2/\text{sec}$  for energies above 40 keV and  $10^4/\text{cm}^2/\text{sec}$  for energies above 1.6 MeV. This latter figure may vary as much as a factor of  $10^3$  with increased solar activity. The number of protons arising from solar flares is of the order of  $10^2/\text{cm}^2/\text{sec}$  in the 0.1 to 5 MeV range and  $40/\text{cm}^2/\text{sec}$  above 30 MeV. These numbers are averages over a long period of time.

To test the effect of radiation on the various satellite components, a Van der Graaf linear accelerator is available. It provides a beam of electrons of a single energy (which is controllable), and hence cannot duplicate the total radiation environment in orbit. To simulate five years in orbit, as near as is practical, it has been determined that the component under test should receive an accumulated dosage of  $10^{16}$  electrons/ $\text{cm}^2$  of 1 to 2 MeV electrons.

The main concern was the radiation damage to the PIN diode. Although the metal cover and boron nitride on the switch reduce the radiation intensity to the diode, it was desirable to know the effect of different radiation dosages on the diode's electrical characteristics. Several 3-mil diodes were irradiated while reverse biased at 100 V. Two were given a dosage of  $10^{15}$  electrons/ $\text{cm}^2$  and the switching noise amplitude measured before and after the test. The effect is shown in Fig. 75. The noise was remeasured four times in the following 4 days, with approximately the same results. Thus, there was some permanent damage to the diodes. Two diodes were radiated in steps from  $3 \times 10^{11}$  to  $10^{14}$  electrons/ $\text{cm}^2$  accumulated dose. No change in switching noise was noted for an accumulated dose up to  $3 \times 10^{13}$  electrons/ $\text{cm}^2$ . At  $10^{14}$  electrons/ $\text{cm}^2$ , one of the diodes dropped in breakdown voltage from 700 volts to less than 150 volts. However, 12 hours after its irradiation, the diode had recovered. It was conjectured that the damage observed on these diodes was associated with the semiconductor chip surface, because of the

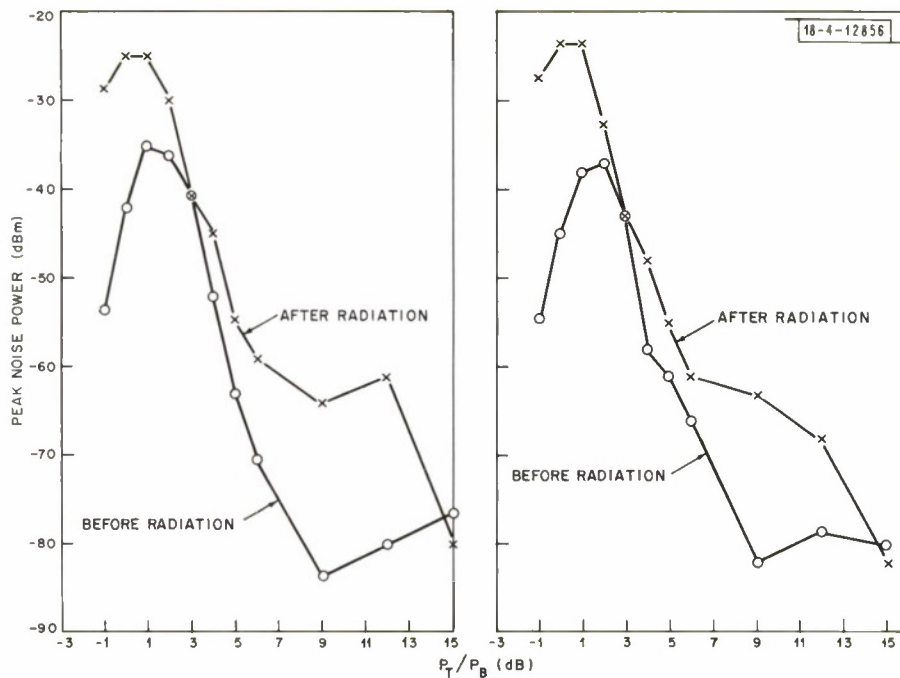


Fig. 75. Switching noise amplitude (as measured in circuit of Fig. 62) of two 3-mil diodes turning OFF before and after radiation with an accumulated dose of  $10^{15}$  electrons/cm<sup>2</sup> ( $P_B = 30$  dBm,  $V_R = 100$  V,  $I_F = 50$  mA, and  $T = 20^\circ\text{C}$ ).

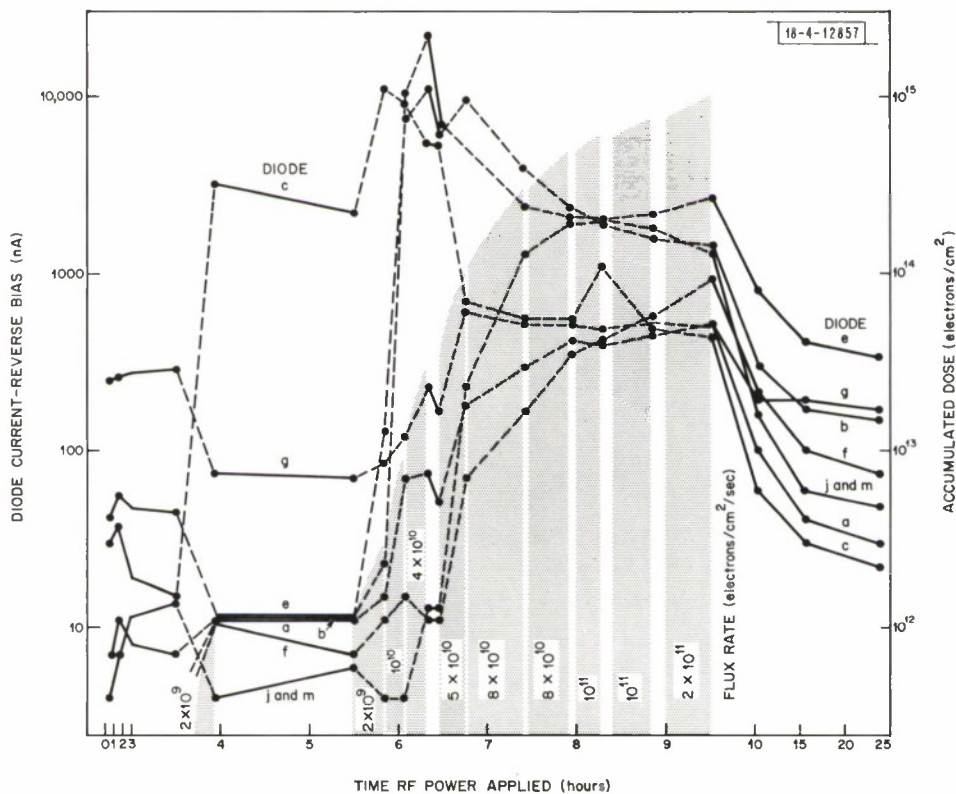


Fig. 76. Measurements of reverse-bias leakage current of 2-mil diodes in operating switch matrix set up in radiation beam. Switch diode units were configured as in Fig. 18. Bars indicate intervals during which switch was radiated. Electron energy = 2 MeV,  $P_T = 48$  dBm,  $V_R = 100$  V, and  $I_F = 45$  mA.



nature of the increased leakage current as discussed in Sec. II-C. It is estimated that the diodes will receive a maximum accumulated dosage of less than  $10^{12}$  electrons/cm<sup>2</sup> over 5 years.

Early in this program a switch matrix with 2-mil diodes and a radiative heat sink design (Fig. 18) was mounted in the Van der Graaf accelerator beam. The switch, connected with a hybrid, was set up so that the diodes in the SP4T sections, which were unshielded, were fully exposed to the electron beam. The switch was set on beam N, that is diodes d, h, k and l were put on forward bias, and 70 watts of RF power applied. Radiation of 2-MeV electrons was delivered in ten intervals of increasing dosage separated by periods of no flux. Before, between, and following the dosage intervals, the current of all ON and OFF diodes, and the RF power levels from seven of the output ports were monitored periodically up to 24 hours after the radiation was terminated. (No readings were taken on the eighth port because of a faulty cable.)

Figures 76 and 77 show the results of the measurements as well as the periods of radiation, electron flux rate and accumulation. (Because of the way the circuit was set up, the combined current of diodes j and m was measured.)

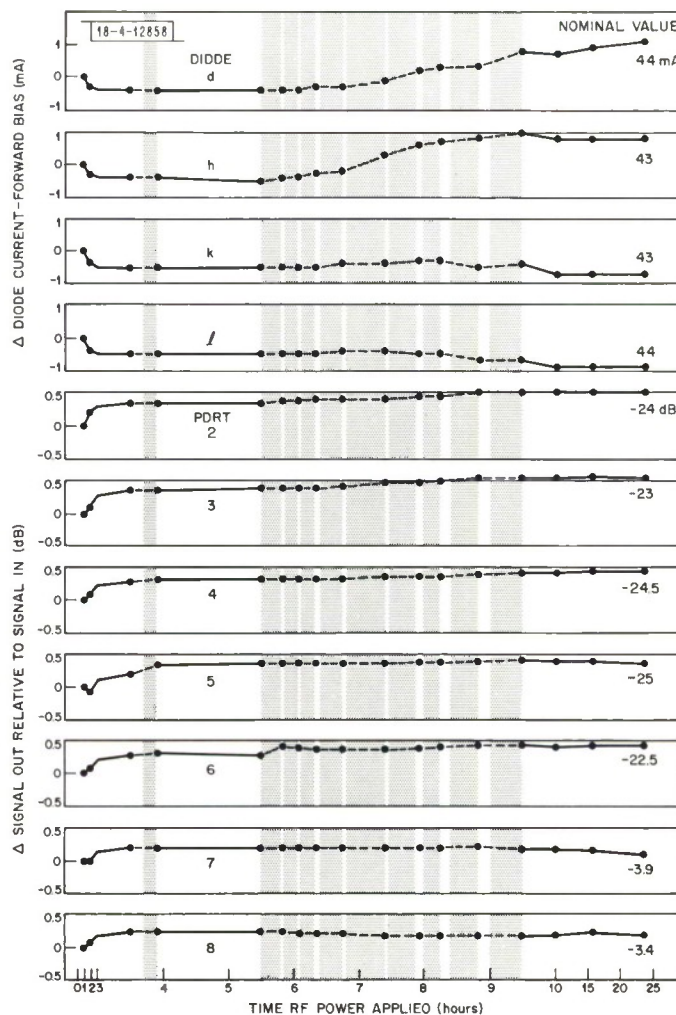


Fig. 77. Relative values of output RF signal level and diode forward-bias current for constant voltage for experiment described in Fig. 76.



A few observations are worth noting:

- (a) As with the 3-mil diodes irradiated separately, the reverse bias currents peaked in the course of the radiation. However, this leakage then decreased as the doses were increased. Over a period of time after the end of the radiation, the diodes recovered. Two of them, c and g, actually exhibited lower leakage at the end of the run. It would have been interesting to observe whether the 3-mil diodes would exhibit this anomalous behavior. Indications are, generally, that they would.
- (b) The forward bias currents of the two diodes k and l showed an initial rapid decrease, suggesting a breaking-in process, followed by a gradual decrease over the rest of the time period of this experiment. The diodes d and h, which faced the electron beam, showed an increase of about 1 mA.
- (c) No change in the RF characteristics, VSWR, insertion loss, and isolation was definitely attributable to radiation effects.

The important result learned from these tests is that an unshielded diode irradiated with an accumulated dosage equivalent to 5 years in orbit experiences changes in characteristics but in time recovers. In the real situation where the diodes are shielded and the dosage rate is greatly reduced, it is intuitively expected that the diodes should not be affected. It has been known that among diodes generally, the PIN diode has a high resistance to radiation. Therefore no problem due to radiation is anticipated.

## XI. RELIABILITY

### A. Various Considerations Involved

It was required that the switch matrix operate well throughout the anticipated 5 years in orbit. Its reliability depended on the stresses to which it would be subjected which fall in two main categories, mechanical shock and vibration associated with launch and the temperature conditions in the vacuum of space. The switches and components had to be subjected to an extensive testing program having several aspects, namely, to establish the mechanical sturdiness of the components, to remove weaker components from the batch of materials obtained for the flight switches, to produce an acceptable switch configuration and to demonstrate the integrity of the flight switches. For test purposes, whichever aspect is of concern determines the stress levels to which a component or switch is subjected. A part set aside for testing may be subjected to 200 percent of an actual expected stress whereas a flight part may be tested to 80 percent.

It is not practical to duplicate the stress levels that the switches undergo from launch through orbit. The real physical shocks and vibration that the switch encounters can be simulated accurately only in tests with the switch mounted on the triplexer in the complete satellite. In the same way as for the temperature measurements described in Sec. V, it is logical to have a test sequence involving each component alone, the completed switch, and the switch mounted in the satellite. These tests would have to be based on an estimate of the potential mechanical stresses.

The aspect regarding the life of the switch in orbit is more complex. It is simply not feasible to reproduce conditions and watch performance over an actual 5-year period. "Accelerated life" testing is called for, where stresses are intensified and the equivalent performance compressed within a shorter time. A relation involving the equivalence of the two situations then enters the picture.

One of two philosophies can be chosen for a given test. Whichever is chosen depends largely on the value of the end results. The first involves subjecting the components to stresses that are in a specific relation to the condition of launch and orbit. Such tests are appropriate for testing a structure for suitability for the flight. The second involves stresses which cause weak components to fail early so that they can be eliminated before components are selected for the flight hardware. It is then expected that survivors are sound and the end result is that the overall reliability is improved. In such a "screening" test, the stress levels must be judiciously chosen so that units that survive have not been weakened. In principle, the ideal situation is to find a stress level where the resulting reliability is maximized, and this depends on the nature of the failure rate of the device. It is best applied to devices whose failure rate is significantly higher in the initial time period. Tests of this kind are better suited for the selection of components to be used on the satellite.

A complete study of all these factors would have involved more time and effort than was at our disposal. The effort thus had to be apportioned among tests according to the amount of confidence in the item under question. That is, items of lower confidence required more testing.

Of the items used in the switches, the reliability of the PIN diodes was most in question. The coils and capacitors were well qualified by the testing and experience of other users as well as by the MIL standard requirements. The rexolite of the stripline had been investigated by others in vacuum tests for outgassing and tolerance to radiation. Although rexolite is brittle, its mechanical strength in the switch is enhanced by the aluminum ground planes, but whether sufficiently so remained to be determined.

As much care as was reasonable was used in the course of building each flight switch. Machined parts underwent visual and mechanical inspection. All machined metal parts were gold plated under a set of quality specifications. In the course of assembly, parts were cleaned at each stage of construction. Each solder joint was inspected and resoldered if necessary. Handling in general was kept at a minimum, and "clean room" procedures followed wherever possible.

Several extended testing programs were carried out. Some were concerned with the PIN diodes and the remaining with the switch matrix. Two aspects of the diodes were of consequence. One was the demonstration of their life duration under certain stress conditions and the other was the subjection of the diodes to a number of examinations to eliminate the less reliable. In addition, a switch matrix which was not of flight quality construction was subjected to conditions of somewhat severe mechanical shock and vibration and temperature cycling largely to demonstrate the integrity of the design. The flight switches were subjected to a similar test but of less severity in order to make evident any defects in workmanship. A description of each of these tests follows.

#### **B. PIN Diodes - Accelerated Life Tests**

Accelerated aging involves testing at a sufficiently high stress level so that a significant number of failures occur in a reasonable time. In conjunction with such a test a functional relation is needed enabling an extrapolation of the results to normal operating levels. Since temperature is the important stress seen by the diodes in their lifetime in orbit, it is the appropriate stress factor.

To enable an accurate extrapolation to operating levels, several measurements at different temperatures are needed. Values are most expediently found by a step stress test, that is, a test where the stress is taken through a series of levels at equal time intervals.<sup>20</sup>

Like other chemical processes in solid state devices, the degradation proceeds approximately at a rate

$$R = R_0 e^{-Q/T} \quad (94)$$

$T$  is the absolute temperature,  $R_0$  is related to the device geometry, and  $Q$  is associated with its energy levels. The total degradation in a time  $t$  is

$$S = R_0 t e^{-Q/T} \quad (95)$$

(which assumes that its previous history has had no effect). If  $f_s(\cdot)$  is the statistical distribution of  $S$ , then the fraction of failures is  $F_s(X)$  where  $X$  has a value determined by the failure criterion. The probability of failure within a system containing  $m$  of these components then depends on both  $F_s(X)$  and  $m$ .

For the step stress test, if there are  $n$  steps with temperature  $T_i$  at the  $i^{\text{th}}$  step, the degradation is

$$S = R_0 t \sum_{i=1}^n e^{-Q/T_i} \quad (96)$$

Here  $t$  is the time interval of each step. In the case where the temperature is stepped according to the relation

$$\frac{1}{T_i} = \frac{1}{T_0} - (i-1) \Delta \quad (97)$$

where  $\Delta$  represents a constant increment in the step, Eq.(96) reduces to

$$S = R_0 t e^{-Q/T_0} \frac{1 - e^{Qn\Delta}}{1 - e^{Q\Delta}} \quad (98)$$

This relation can be equated to a constant stress at an equivalent temperature  $T_{eq}$  where

$$\frac{1}{T_{eq}} = \frac{1}{T_0} - \frac{1}{Q} \ln \frac{1 - e^{Qn\Delta}}{1 - e^{Q\Delta}} \quad (99)$$

and

$$S = R_0 t e^{-Q/T_{eq}} \quad (100)$$

Before these equations can be used, the value of  $Q$  must be known. Some parameter may be measured if it is known to have an  $e^{-Q/T}$  dependence. Or the results of a constant stress test may be used to plot  $\log R$  versus  $1/T$ . The most directly related method is to fit the results of the step stress test to Eq.(98). The fitting however may be difficult.

The manufacturer of the PIN diodes had carried out many reliability testing programs with solid state devices. Specifically, constant stress and step stress tests were made on many PIN diodes. Some of their conclusions, which are relevant, are

- (1)  $\ln S$  fits a normal distribution well over most intervals of time, or the degradation  $S$  has a log-normal distribution. Discrepancies occur at long and at short times where the number of failures is higher than given by this distribution. Otherwise the accuracy of the model as represented by Eq.(94) is justified.



- (2) The failures occurred with reverse bias applied to the diodes, whereas the failure rate associated with forward bias was insignificant in comparison. The criterion adopted by the manufacturer for these tests was that the leakage current with normal reverse bias was in the milliampere range.
- (3) Two types of failure occurred. One was the abrupt change of the diode to a short circuit due to a bulk breakdown of the semiconductor. The other appeared gradually and was associated with the generation of surface channels as described in Sec. 11-C. However, there was no apparent correlation between the diodes that failed and those that had poor initial V-I characteristics, as, for example, those exhibited in Fig. 9(e).
- (4) No difference in failure rate, with or without a large RF signal, was observed, provided the temperature of the diode semiconductor was the same in both cases.

Numerical values of mean life time and temperatures are reported with this work (including a value of  $11,300^\circ\text{K}$  for  $Q$ ). However, they are not applicable to the switch operation in the satellite for several reasons. The "failure" of a diode is a subtle phenomenon here. Rather than noting the number of diodes that simply have stopped functioning, we must concern ourselves with diodes where the reverse bias leakage current has exceeded some value. This concern arises from the contributions of the diode to the noise figure of the satellite. As a result of the noise figure measurements described in Sec. IX, a criterion was adopted that to be acceptable the maximum current must be  $10\text{ }\mu\text{A}$  for a  $100\text{-V}$  bias. A second point is that the operating temperatures cited in the above report are high — above  $150^\circ\text{C}$  — and the extrapolation to temperatures below  $100^\circ\text{C}$  becomes questionable. Thirdly, the PIN diodes were of different geometry and construction.

In satellite operation, the switching rate of each diode is such that it is on reverse bias for  $\frac{1}{2}$  or  $\frac{3}{4}$  of any time period. The temperature of the diode depends on resistive losses on forward bias, but it is the combination of this temperature and the reverse bias that determines its reliability. The stable temperature values would be as determined in Sec. V. The tests described below involve application of a steady reverse bias to the diodes at various temperatures. The reliability may be affected by continuous switching of bias, but it is expected that, if anything, it improves. Therefore, the tests would give a safety margin if such is the case.

For the stress testing of diodes in this program, a system was set up as shown in Fig. 78. The reverse bias of  $100\text{ V}$  was continuously applied to the diodes throughout the tests and the leakage current monitored. A measure of the V-I curve of a reference diode provided the temperature, which had been previously calibrated. The parameter measured for the indication of performance was the current for the  $100\text{-V}$  bias at the ambient temperatures ( $20^\circ$  to  $25^\circ\text{C}$ ).

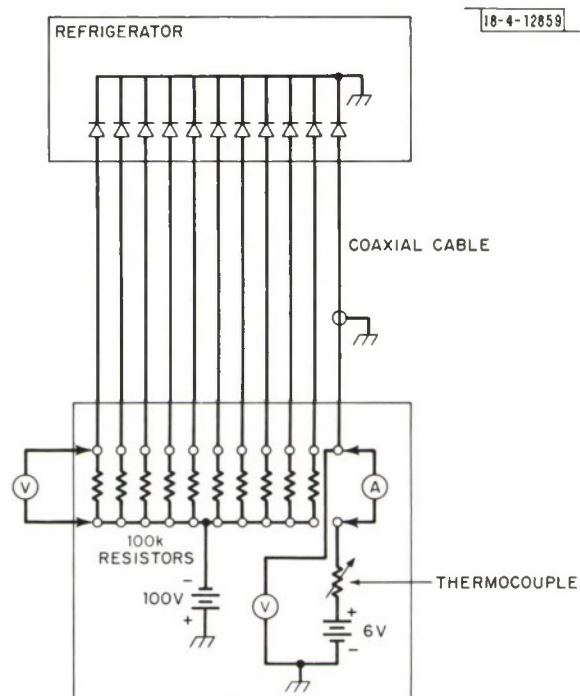


Fig. 78. System for life testing PIN diode. Reverse-bias leakage current is measured for indication of diode quality.



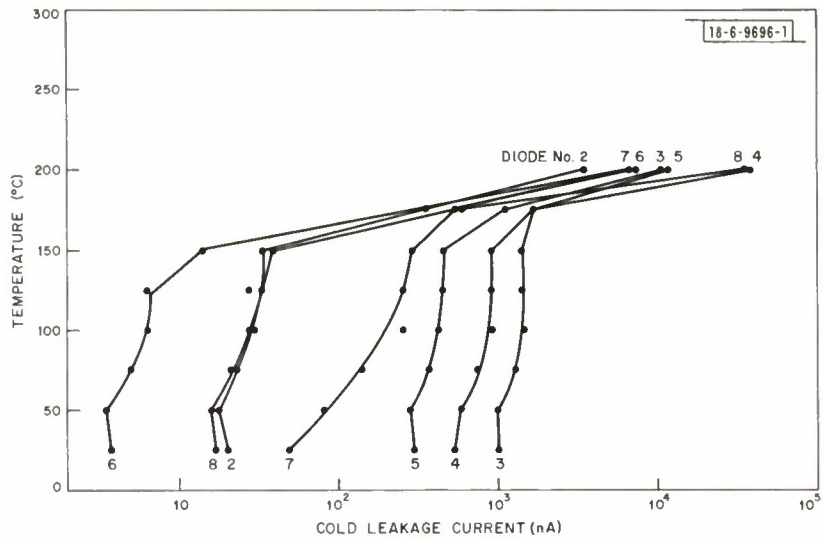


Fig. 79. Reverse-bias leakage current of ambient temperature in step stress test with 3-mil diodes subjected to reverse bias of 100 V and steps of 25°C amplitude and 24-hours duration from 25°C to 200°C.

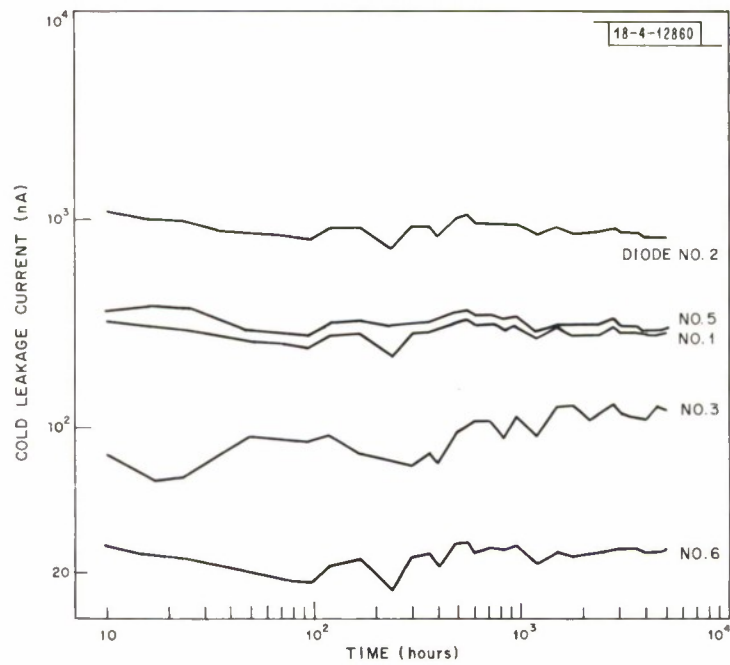


Fig. 80. Reverse-bias leakage current in constant stress test with 3-mil diodes subjected to reverse bias of 100 V at ambient temperature for 5000 hours.

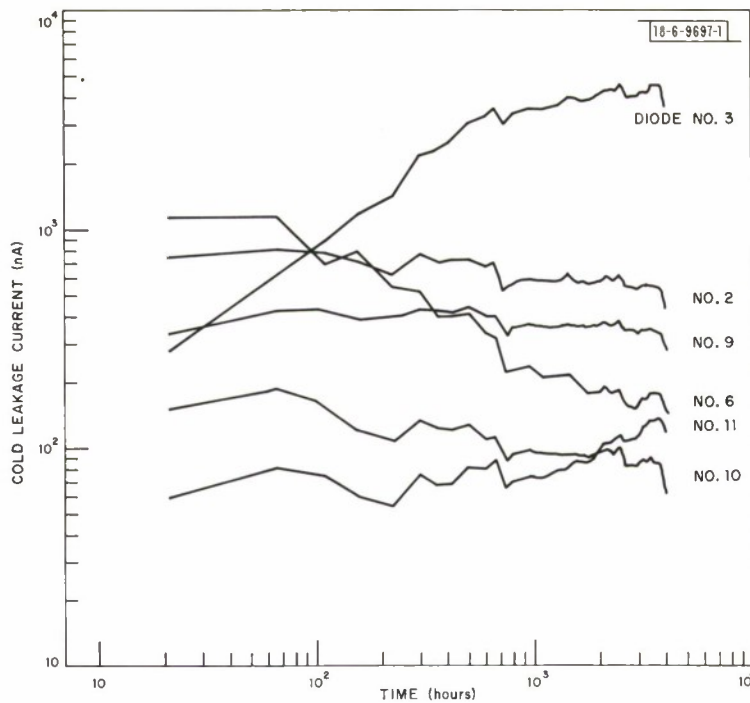
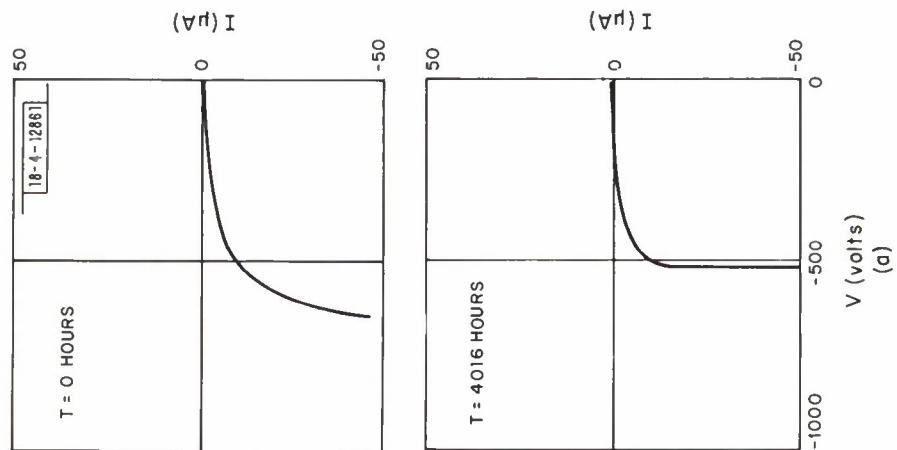


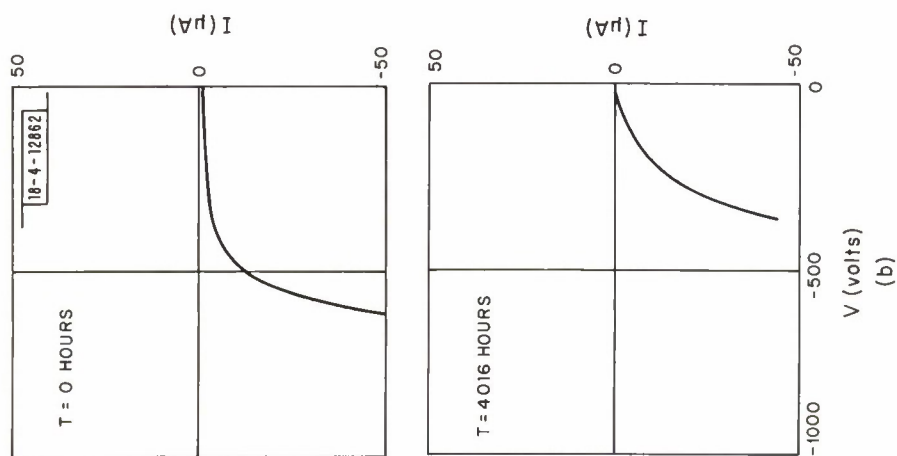
Fig. 81. Reverse-bias leakage current in constant stress test with 3-mil diodes subjected to reverse bias of 100 V at  $T = 125^{\circ}\text{C}$  for 4000 hours.

Seven 3-mil diodes were subjected to a step stress test. Each step was  $25^{\circ}\text{C}$  in amplitude and 24 hours in duration. The temperature range was from  $25^{\circ}$  to  $200^{\circ}\text{C}$ . The measured leakage current after each temperature step is plotted in Fig. 79 for diodes Nos. 2 through 8. If the equivalent temperature as given by Eq. (99) had been plotted and the form given by Eq. (100) represented the true characteristic, the plots would be straight lines. The abrupt change in slope in the  $150^{\circ}$  to  $175^{\circ}\text{C}$  region cannot be accounted for by the use of the actual rather than the equivalent temperature. It is assumed then that a physical change had occurred in the diodes that is irreversible. The diodes still had normal switching operation, however. With regard to the work of the manufacturer mentioned above, the concern was for total failure and this change in behavior went unobserved. Whatever the mechanism, it apparently is independent of the initial leakage current as indicated by the absence of any apparent correlation between final failure and the initial current.

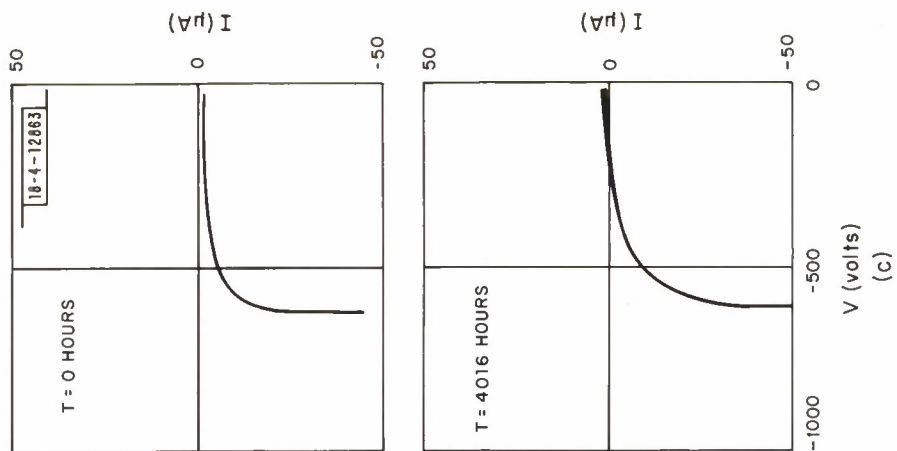
Due to the change in behavior of the diodes above  $150^{\circ}\text{C}$ , the step stress test did not offer meaningful data in the long term operation of the diodes. A long duration test was called for at an elevated temperature not exceeding  $150^{\circ}\text{C}$ . Two "life" tests were carried out, one involving six 3-mil diodes, Nos. 1 through 6, biased at 100 V and set at a temperature of  $20^{\circ}\text{C}$  continuously for 5000 hours, the other involving ten 3-mil diodes, biased at 100 V and subjected to a temperature of  $125^{\circ}\text{C}$  for 4000 hours. The results of the first test are given in Fig. 80 (where the results of diode No. 4 are omitted because of their similarity to the curves for diodes Nos. 1 and 5). The results of the second test are shown in Fig. 81 for six of the ten diodes. The remaining four, omitted for clarity, followed approximately a constant trend between the curves of diodes Nos. 2 and 10. The two extremes in the characteristics are exhibited by diodes Nos. 3 and 6. Diode No. 6 is interesting because of the large decrease in leakage current with time.



(a) Diode No. 2



(b) Diode No. 3



(c) Diode No. 6

Fig. 82. V-I curve traces of 3 diodes characterized in Fig. 81 before and after stress of 100 V and 125°C for 4000 hours.

This improvement with age is difficult to explain. Somehow, the surface channels on the diode were being eliminated by the stress conditions. The diode showing the most degradation, No. 3, settled in performance beyond 1000 hours.

It is apparent that maintaining the trends of these curves, it is unlikely that any of these diodes would exceed the leakage current level of  $10^4$  nA at 5 years (44,000 hours). The currents all stabilized at lower values in the course of the run. Thus the probability of one out of 24 diodes on the satellite failing in 5 years is negligible based on these results. Shown in Fig. 82 are V-I traces for diodes Nos. 2, 3, and 6 preceding and following the stress test. The change in the curves can be associated with the nature of the diode semiconductor as described in Sec. II-C.

The potential degradation of the diode in continued operation has been observed and supports the rationale for selecting diodes for low leakage current based on short life tests. It is thus desirable to remove diodes that initially have poorer than average V-I characteristics, or those that have a substantial degradation in these characteristics following a short life test. Although diode reliability would be considered good before screening, the reliability of the diodes remaining after screening would be excellent. The next section describes a diode screening process including some short term life tests.

### C. PIN Diodes - Screening

Some 81 diodes were subjected to a screening program from which the 48 best units were to be used for the flight and flight back-up switches. Some of the screening tests involved stressing the diodes so that weaker ones would fail and could be removed. As mentioned in Sec. XI-A, the stresses should be judiciously chosen so that the good diode is not weakened. Experience in general has given us a criterion that a stress should not cause any more than about 5 percent to fail; but at the same time, if the number of failures is few or nil, the usefulness of the test may be in question in some circumstances.

The screening tests are tabulated in Appendix C. They were the results of the considerations and compromises of several programs and studies. These included prior knowledge concerning PIN diodes, tests adopted for other components to be flown on the satellite, and tests used by the military on other missiles. The screening is divided into several groups of tests, each followed by measurements of their electrical characteristics such as the reverse-bias leakage current and forward-bias voltage. Among the tests are visual and x-ray examinations, mechanical shock and vibration tests, thermal shock, and abbreviated life tests. (The diodes were in two separate test lots, not for technical reasons, but due to schedule pressures.) Listed in Table VII are the qualities exhibited by the diodes after the screening as reflected by measurements of their various characteristics. (The failures did not necessarily occur as a result of the screening tests.) The best diodes were then selected for the flight and flight back-up switches.

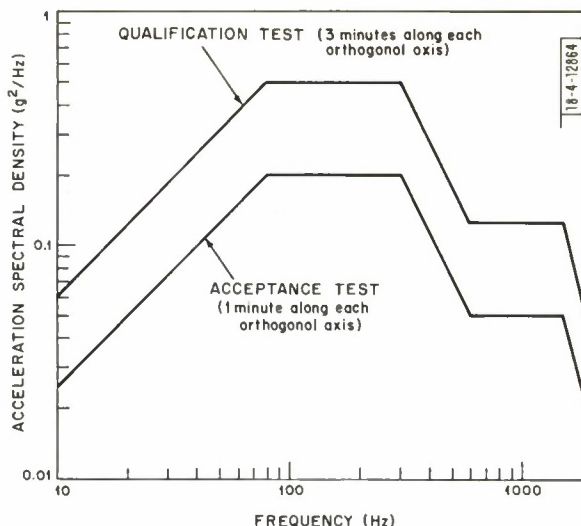
### D. Switch Matrix - Mechanical Tests

A switch matrix was set up as a qualification model to be subjected to stresses exceeding those anticipated in the flight satellite. In the shock and vibration tests, the switch was mounted on a platform which could be driven in programmed modes of oscillation. The spectrum of the vibration test adopted for the qualification switch is shown in Fig. 83. The vibration is directed along the three orthogonal axes of the switch for a duration of 3 minutes each. Following the application of the vibration mode along each axis, a shock impact of 850 g acceleration for 0.2 ms was applied. The appearance of the shock impulse was that of a half cycle of a sine wave.



TABLE VII DIODE QUALITIES AFTER SCREENING											
Diode No.	Visual, Mechanical, X-Ray	V-I V < 400 V for I = 10 $\mu$ A	IM > -135 dBm	Switching Noise > -60 dBm	Flight Switch	Diode No.	Visual, Mechanical, X-Ray	V-I V < 400 V for I = 10 $\mu$ A	IM > -135 dBm	Switching Noise > -60 dBm	Flight Switch
1						45					
2						46					
3		X				47		X			
4						48					S
5						49					
6						50	X				
10				X		51			X		
11	X					52					D
12	X					53					D
13					D	54					D
14					S	55					
15					D	56					
16						57					D
17						58				X	
18	X					59					S
19						60					S
20					D	61					
21					S	62					
22					D	63					
23						64					S
24		X				65					D
25	X					66					S
26				X		67		X			
27						68					
28						69					
29						70					
30		X				71					
31					S	72		X			
32						73					
33	X					74					D
34					S	75					D
35						76					S
36						77					D
37						78					S
38						79					
39					S	80					
40						81					
41						82					
42				X		83					
43						84					
44			X								
X - diodes of substandard quality S - flight switch for the slots D - flight switch for the dipoles											

Fig. 83. Spectrums of random vibration test to which switch matrix is subjected. Qualification test is for design suitability and acceptance test for acceptability of flight switch on satellite.



The first run of these tests on the switch qualification model resulted in many breaks in the bonds between the coils and the ground planes. An examination of the breaks led to the conclusion that the ground plane surface should be very clean, and more epoxy used. The addition of epoxy caused some minor degradation in the switch RF characteristics. Once the cure was effected, the switch successfully withstood the mechanical tests.

The four flight and back-up switches were subjected to the vibration tests whose spectrum is given in Fig. 83, one minute along each of the three orthogonal axes. No damage was observed as a result of the runs. The two flight switches, when mounted in the fully operating satellite, again underwent a vibration run and again without mishap.

#### E. Switch Matrix - Thermal Cycle

The qualification switch (the same one used for the mechanical tests) was taken through six full temperature cycles while the nominal transmit and beacon powers were applied to the switch. As a sensitive indicator of any degradation, the IM levels of the switch at the temperature extremes were monitored. The temperature cycle, as plotted in Fig. 84, had limits of  $+60^{\circ}$  and  $-40^{\circ}\text{C}$ , the values designated for the maximum operating temperature of satellite internal components. The period of each cycle was about 1 hour. At the completion of the run, no failures were observed.

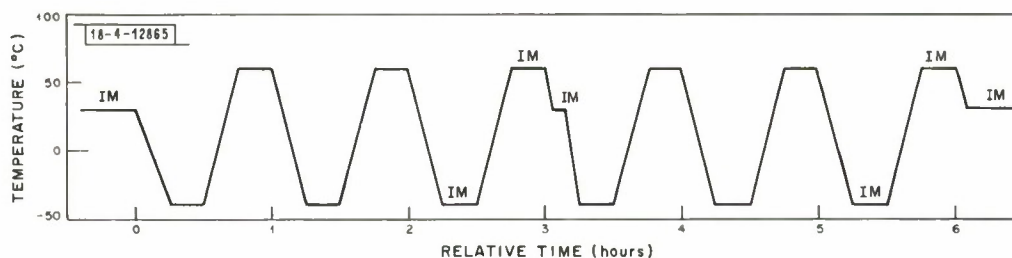


Fig. 84. Temperature cycle test to qualify switch matrix design. Points labeled IM indicate times when IM is measured.

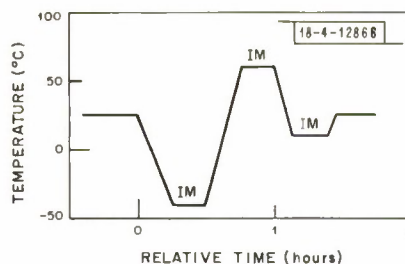


Fig. 85. Temperature cycle test for flight switches.

For the flight switches, there was one thermal cycle preceding and one following the vibration tests as shown in Fig. 85. Again, no change in performance was detected.

To add to our information, when the switches were mounted and completely connected together in the satellite with the antenna system, measurements of the VSWR at the triplexer transmit filter input were made under various diode failure modes. At the transmit frequency, the highest VSWR values observed was about 1.6 where all four diodes on the 2P2T section of the slot switch were put on reverse bias

which is equivalent to the diodes all becoming open circuits. At the same time, the signal to the dipole hybrid load was 5.7 dB below the input signal. This information might be useful for diagnostic purposes if failures ever occur while in orbit.

## XII. ANTENNA PATTERNS AND CHOICE OF SWITCH MATRIX CONFIGURATION

Following is a discussion of the considerations which led to the switch configuration shown in Fig. 5(a). Although the study preceded the development and testing of the switch, this account was postponed until now because it is not directly related to the switch characteristics.

### A. Discussion of Antenna Patterns in General

Given a satellite geometry and antenna elements of specified type and numbers, a knowledgeable decision was to be made concerning the total number of beams  $n$  to generate. To do this, the coverage required of one beam which depends on the number  $n$  must be established and the corresponding optimum pattern determined. Next the excitations of the antennas which give rise to approximately the optimum pattern must be found; and finally, the switch matrix configuration which can generate any one of  $n$  such patterns is chosen. Of the several possibilities that come into consideration, the best choice is based on weighing the antenna system gain observed at any station on the earth against the complexity of the antenna system.

Relative to the satellite beam that is on, an earth station may lie anywhere within a range of directions which defines a region of solid angle. It is then desired to obtain the maximum gain throughout this region. In other words, given the limitations of the antenna system, there is an optimum pattern where the lowest gain in the region is maximized. This section will first deal with antenna patterns and coverages as a function of the number of beams  $n$ .

The layout of the communications system involving the satellite  $O$  and the earth, center  $E$ , is represented in Fig. 86, with north pointing to the viewer. For the moment, the discussion shall be confined to the two-dimensional plane of the equator (or the plane normal to the spin axis). The figure shows the typical pattern of a beam in the two limiting cases, the moment it is turned ON (solid curve), and the moment it goes OFF (dashed curve). The pattern directions at these two limits are determined by other instruments on the satellite such as earth and sun sensors and clocks. An arbitrary line  $OA$  is designated as the beam center so that other lines may be referred to it. In the first moment, a station at some point  $P$  is located at an angle  $AOP$  from the beam center which, as shown in the figure, is the largest of any subtended between the beam center and any station. For this observer the satellite is on the horizon. Similarly, at the last moment, the largest angle is  $BOQ$ , where now the beam has moved through angle  $AOB$

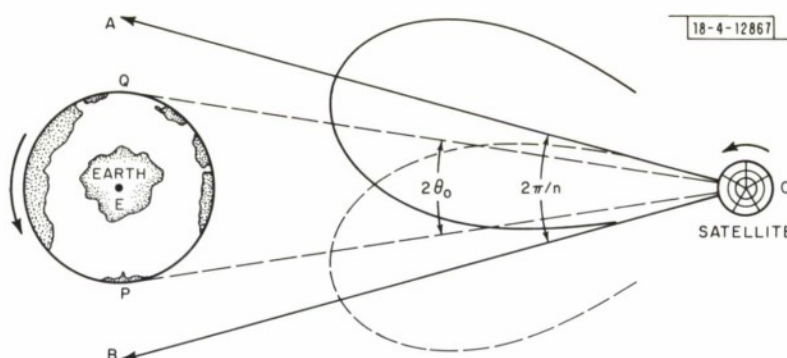


Fig. 86. Representation of one of antenna patterns at limits of its positions: the moment it turns on (solid curve) and off (dashed curve).

and the "furthest" located station is at Q. The angular range of the antenna pattern that is of concern is then given by

$$2\varphi_0 = \angle AOP + \angle BOQ \quad . \quad (101)$$

Now

$$\angle AOP = \angle AOE + \angle POE \quad (102)$$

and

$$\angle BOQ = \angle BOE + \angle QOE \quad . \quad (103)$$

Therefore

$$2\varphi_0 = \angle AOE + \angle POE + \angle BOE + \angle QOE \quad (104)$$

There are  $n$  beams, and we shall consider only the case where each beam is on for  $1/n$  of one rotation of the satellite. Hence,

$$\angle AOE + \angle BOE = \angle AOB = \frac{2\pi}{n} \quad . \quad (105)$$

At the altitude of the synchronous satellite ( $3.59 \times 10^7$  m),

$$\angle POE = \angle QOE = 0.15 \text{ radian } (8\frac{1}{2}^\circ) \quad . \quad (106)$$

This angle shall be denoted  $\theta_0$ . Equation (104) then reduced to

$$2\varphi_0 = \frac{2\pi}{n} + 2\theta_0 \quad . \quad (107)$$

Some values of angle  $2\varphi_0$  are listed in Table VIII for different values of  $n$ . The last case,  $n \rightarrow \infty$ , corresponds to the alternate situation of scanning the beam in a continuous mode as mentioned in Sec. I.

TABLE VIII					
VALUES OF ANGLE $2\varphi_0$ FOR DIFFERENT $n$ FROM EQ. (107)					
$2\varphi_0$ (degrees)	$n$				
	4	8	12	16	$\infty$
	107	62	47	$39\frac{1}{2}$	17



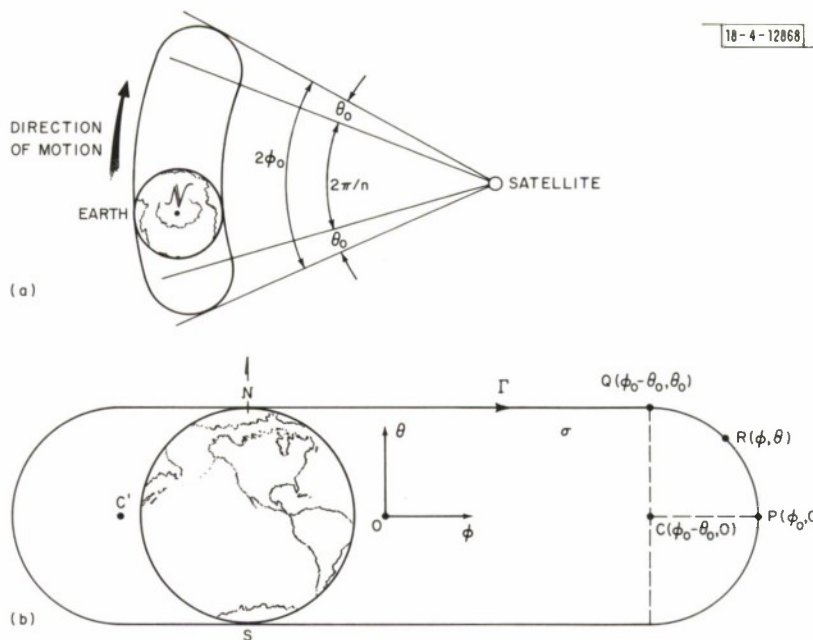


Fig. 87. (a) Region traced by earth in satellite antenna pattern. (b) Coordinate system setup in region  $\sigma$  traced by earth.

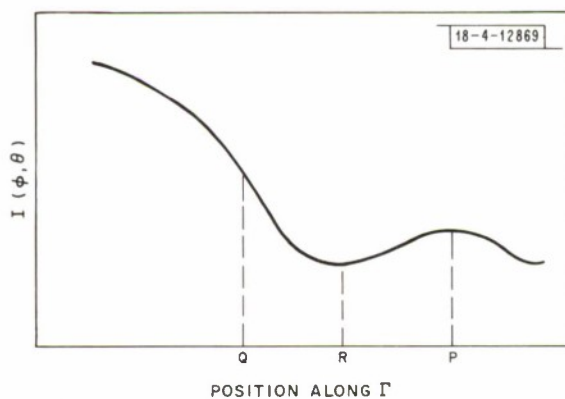


Fig. 88. Trend of field intensity moving along boundary  $\Gamma$  of region  $\sigma$ .

Now removing the restriction that the station lie in the region of the equator, it is necessary to look at the complete solid angle within the antenna pattern in which any ground station can lie. Figure 87(b) shows this region  $\sigma$  enclosed by the curve  $\Gamma$ . Its shape is a rectangle where the two opposite sides have been replaced by semicircles. Its length is  $2\varphi_0$  and width  $2\theta_0$  (angles are referred to as distances). A rectangular coordinate system is centered in the region. The coordinates of some points related to the one semicircle are  $C(\varphi_0 - \theta_0, 0)$ , its center:  $P(\varphi_0, 0)$ , the center of the arc; and  $Q(\varphi_0 - \theta_0, \theta_0)$ , the point where it joins the straight line at  $\theta = \theta_0$ .

The ideal situation would be to have the entire radiation pattern bounded inside the curve  $\Gamma$  (the existence of radiation outside would reduce the gain inside) and uniformly flat (to increase the gain at one point would cause a decrease in gain at another point). However, the control one has on the pattern is limited. Because there are only two rows of elements on the satellite, the only feasible pattern along the  $\theta$ -axis is symmetrical and centered at  $\theta = 0$ , and there is essentially no shaping that can be effected. For the pattern along the  $\varphi$ -axis, it is possible to control its width (say, at XdB below the peak) or shape by a suitable selection of antenna element amplitudes and phases. But again, with the few parameters at our disposal, the width and shape are not independently adjustable. A detailed examination must then be made concerning the patterns that are possible to obtain, with the view of ultimately selecting the best one.

Some information can be gathered concerning the pattern based on several assumptions. Denoting the pattern by an intensity function  $I(\varphi, \theta)$  or simply  $I$ , it will be a smooth function inside the region  $\sigma$ . It will be symmetrical in  $\theta$  and will have a peak at or near the origin. Approaching the curve  $\Gamma$  from the origin, the slopes  $\partial I / \partial \varphi$  and  $\partial I / \partial \theta$  will be negative for positive  $\varphi$  and  $\theta$  (that is, pattern nulls are outside the region  $\sigma$ ). Also, generally patterns are characterized by negative values of  $\partial^2 I / \partial \varphi^2$  and  $\partial^2 I / \partial \theta^2$  throughout much of their main lobe.

It can then be expected that the minimum value of  $I$  in the region  $\sigma$  occurs somewhere on the boundary  $\Gamma$ . Hence, the logical step is to note the trend in  $I$  along the curve. Such a trace would have the appearance shown in Fig. 88. Traversing  $\Gamma$  at the top toward the point  $Q$ ,  $I$  decreases (since  $\left. \frac{\partial I}{\partial \varphi} \right|_{\varphi > 0} < 0$ ). At point  $P$ ,  $I = I_P$  has a slope of 0 because of its symmetry in  $\theta$ .

Hence,  $I_P$  is a maximum or a minimum. If  $I_P$  is maximum, there must exist a point  $R$  between  $P$  and  $Q$  where  $I = I_R$  is minimum. The existence of the point  $R$  is significant, because it is the point in the whole region  $\sigma$  where  $I$  is minimum. Ideally, it is the point where one would try to get the maximum gain under the constraints imposed by the antenna system. In practical circumstances, to attempt to ascertain the voltages of the antenna element excitations to evoke the maximum field at point  $R$  would be tedious when approached both mathematically and by actual measurement.

The point  $R$  may fall anywhere along the arc  $QP$ . In the one extreme, it may coincide with point  $P$  and  $I_P$  is now a minimum. This occurs when the pattern along the  $OP$  line is too narrow and the problem would then reduce to striving for the optimum pattern along  $OP$ . For the other extreme, if point  $R$  is near point  $Q$ , the field  $I_R$  is primarily influenced by the  $\varphi$ -axis pattern. That is to say, assuming the relative pattern from  $C$  to  $R$  is not adjustable and remains constant, one may achieve the maximum absolute value of the pattern by a suitable choice in the  $\varphi$ -axis pattern. Interestingly, for both cases where point  $R$  lies near point  $P$  or point  $Q$ , one may be concerned only with the one pattern but with consideration given to the field at two different points,  $P$  or  $C$ . When point  $R$  lies between the two extremes, logically it might be surmised that the field intensity  $I_R$  is made maximum by increasing the field at a point between  $P$  and  $C$ . However,

complications arise when this is attempted, for point R will slide to a new location when the field at the point changes. It can be concluded that, generally, it is sufficient to consider the  $\varphi$ -axis pattern and the field at point P or C to achieve the best field distribution throughout the region  $\sigma$ . The problem is not quite as simple for some small range in pattern shapes when point R is not near either P or Q.

It is of some value to look at the situation quantitatively. In principle, the actual field distribution  $I(\varphi, \Theta)$  is the unknown, and therefore  $I_R$  is also unknown. But some form of the behavior of  $I_R$  is needed to determine the optimum pattern. To avoid this impasse, a few simplifying assumptions shall be made, and approximate relations evolved.

Let us take a two-variable Taylor series expansion about the point P:

$$\begin{aligned}
 I(\varphi, \Theta) = I(\varphi_0, 0) &+ \left. \frac{\partial I}{\partial \varphi} \right|_{\varphi=\varphi_0, \Theta=0} (\varphi - \varphi_0) + \left. \frac{\partial I}{\partial \Theta} \right|_{\varphi=\varphi_0, \Theta=0} \Theta + \frac{1}{2} \left. \frac{\partial^2 I}{\partial \varphi^2} \right|_{\varphi=\varphi_0, \Theta=0} (\varphi - \varphi_0)^2 \\
 &+ \frac{1}{2} \left. \frac{\partial^2 I}{\partial \Theta^2} \right|_{\varphi=\varphi_0, \Theta=0} \Theta^2 + \left. \frac{\partial^2 I}{\partial \varphi \partial \Theta} \right|_{\varphi=\varphi_0, \Theta=0} (\varphi - \varphi_0) \Theta + \dots
 \end{aligned} \quad (108)$$

Terms higher than the second order shall now be neglected. Because  $I(\varphi, \Theta) = I(\varphi, -\Theta)$ , some of the terms are zero and hence,

$$I(\varphi, \Theta) = I(\varphi_0, 0) - a(\varphi - \varphi_0) - b(\varphi - \varphi_0)^2 - c\Theta^2 \quad (109)$$

where

$$\begin{aligned}
 a &= - \left. \frac{\partial I}{\partial \varphi} \right|_{\varphi=\varphi_0, \Theta=0} \\
 b &= - \frac{1}{2} \left. \frac{\partial^2 I}{\partial \varphi^2} \right|_{\varphi=\varphi_0, \Theta=0}
 \end{aligned}$$

and

$$c = - \frac{1}{2} \left. \frac{\partial^2 I}{\partial \Theta^2} \right|_{\varphi=\varphi_0, \Theta=0} \quad (110)$$

The coefficients  $a$ ,  $b$  and  $c$  are positive because of the assumptions made about the pattern shape. Also because

$$\left. \frac{\partial I}{\partial \varphi} \right|_{\varphi=\varphi_0, \Theta=\Theta_0}$$

is negative,

$$a > 2b\Theta_0 \quad (111)$$

The point  $R(\varphi, \Theta)$  is restricted to lie on a circle, and therefore its coordinates are related:

$$\varphi = \varphi_0 - \Theta_0 + \sqrt{\Theta_0^2 - \Theta^2} \quad (112)$$

or

$$\Theta^2 = (\varphi_0 - \varphi)(2\Theta_0 - \varphi_0 + \varphi) \quad (113)$$

To find where  $I_R(\varphi, \Theta)$  is minimum, the differential of Eq. (109) is equated to 0 subject to the restriction of Eq. (112); that is,

$$\frac{dI_R(\varphi, \Theta)}{d\Theta} = \frac{\partial I_R(\varphi, \Theta)}{\partial \varphi} \frac{d\varphi}{d\Theta} + \frac{\partial I_R(\varphi, \Theta)}{\partial \Theta} = 0 \quad (114)$$

$$[-a - 2b(\varphi - \varphi_0)] \frac{-\Theta}{\sqrt{\Theta_0^2 - \Theta^2}} - 2c\Theta = 0 \quad (115)$$

Substituting Eq. (112) for  $\sqrt{\Theta_0^2 - \Theta^2}$  and simplifying,

$$[a - 2c\Theta_0 - (2b - 2c)(\varphi_0 - \varphi)]\Theta = 0 \quad (116)$$

There are two solutions, one in which  $\Theta = 0$  corresponds to the point P, and the other where

$$\varphi_0 - \varphi = \frac{a - 2c\Theta_0}{2b - 2c} \quad (117)$$

corresponds to the point R.

Angle  $\varphi_0 - \varphi$  lies between 0 and  $\Theta_0$ . Thus

$$0 \leq \frac{a - 2c\Theta_0}{2b - 2c} \leq \Theta_0 \quad (118)$$

If  $b > c$ , this reduces to

$$2c\Theta_0 \leq a \leq 2b\Theta_0 \quad (119)$$

but this contradicts Eq. (111). Hence, the point R would not exist (or would have merged with point P).

If  $b < c$ , we get

$$2b\Theta_0 \leq a \leq 2c\Theta_0 \quad (120)$$

Thus, for the point R to exist separately from point P,

$$\left| \frac{\partial^2 I}{\partial \varphi^2} \right| < \frac{1}{\Theta_0} \left| \frac{\partial I}{\partial \varphi} \right| \leq \left| \frac{\partial^2 I}{\partial \Theta^2} \right| \quad (121)$$

where each term is evaluated in the region of R. The equality on the left side was removed to conform with Eq. (111). Equation (121) shows that the existence of R depends on a close relation between the shapes of the  $\varphi$ -axis and the  $\Theta$ -axis patterns.

Substituting Eq. (113) and Eq. (117) into Eq. (109) provides the field intensity at point R:

$$I_R = I(\varphi_0, 0) + \frac{(a - 2c\Theta_0)^2}{4(b - c)} \quad (122)$$



For comparison, the field at point P( $\varphi_o, 0$ ) is

$$I_P = I(\varphi_o, 0) \quad (123)$$

and at point Q( $\varphi_o - \theta_o, \theta_o$ ) is

$$I_Q = I(\varphi_o, 0) + a\theta_o - (b + c)\theta_o^2 \quad (124)$$

Hence, the three field intensities can be compared if the coefficients a, b and c are known. An interesting case arises if

$$a = 2c\theta_o \quad (125)$$

Then

$$I_R = I_P \quad (126)$$

and the field is uniform along the arc PR. In addition, if

$$b \rightarrow c \quad (127)$$

then

$$I_Q \rightarrow I_P \quad (128)$$

and the field approaches a constant value along the whole semicircle.

Equation (122) shows that  $I_R$  has two parts,

$$I_1 = I(\varphi_o, 0) \quad (129)$$

and

$$I_2 = \frac{(a - 2c\theta_o)^2}{4(b - c)} \quad (130)$$

If each part is made maximum, then  $I_R$  is maximum. However, the two parts are not independently variable; if one part is altered, the other is affected. It is reasonable to assume that since  $I_2$  is considerably smaller than  $I_1$ , changes in  $I_1$  are associated with correspondingly smaller changes in  $I_2$ . We conclude that if  $I(\varphi_o, 0)$  is maximum, then  $I_R$  is near maximum, and the field distribution  $I(\varphi, \theta)$  throughout the region  $\sigma$  is near optimum, with the restriction that the relative  $\theta$ -axis pattern is fixed. (In a number of pattern calculations associated with the satellite, the fields  $I_P$  and  $I_R$  always differed by less than 0.2 dB.)

More information may be obtained about the optimum pattern if it can be specified approximately by a formula along the  $\varphi$ -axis. For the moment, let us assume that Eq.(109) represents the pattern throughout the range of  $\varphi$  where  $I(\varphi, \theta)$  is positive and is 0 otherwise. At  $\theta = 0$ , the pattern is a parabola whose peak lies at

$$\varphi_m = \varphi_o - \frac{a}{2b} \quad (131)$$

The parabola is to be centered at the origin; then

$$\varphi_o = \frac{a}{2b} \quad (132)$$

The field intensity, Eq.(109), is now given by

$$\begin{aligned}
I(\varphi, 0) &= b(\xi - \varphi^2) & \text{for } \varphi^2 < \xi \\
&= 0 & \text{for } \varphi^2 > \xi
\end{aligned} \tag{133}$$

where

$$\xi = \frac{I(\varphi_0, 0)}{b} + \frac{a^2}{4b} \tag{134}$$

The peak field is  $b\xi$  and the beam width is determined by the value of  $\xi$ . The next step is to find the relation between the peak field and beam width, where the total energy radiated is constant.

The total energy is proportional to the energy radiated along the plane  $\Theta = 0$  (since the relative  $\Theta$ -axis pattern does not change). The integral

$$E = \int_{-\pi}^{+\pi} I(\varphi, 0) d\varphi \tag{135}$$

is then a constant.

Substituting Eq. (133),

$$E = \frac{4}{3} b\xi^{3/2} \tag{136}$$

Equation (133) then becomes

$$I(\varphi, 0) = \frac{3}{4} E(\xi^{-1/2} - \xi^{-3/2} \varphi^2) \quad \text{for } \varphi^2 < \xi \tag{137}$$

The question now is for what value of  $\xi$  is the field  $I(\varphi_0, 0)$  maximum, when considered at the point  $\varphi = \varphi_0$  specifically. This is found by equating to 0 the differential of  $I$  with respect to  $\xi$ . Thus

$$\xi = \xi_m = 3\varphi_0^2 \tag{138}$$

Then the field intensity is

$$I(\varphi_0, 0) = I_m(\varphi_0, 0) = \frac{E}{\sqrt{12} \varphi_0} = \frac{E}{2 \sqrt{\xi_m}} \tag{139}$$

For the same pattern, the intensity at  $\varphi = 0$  is

$$I_m(0, 0) = \frac{3}{4} \frac{E}{\sqrt{\xi_m}} \tag{140}$$

By dividing Eq. (139) by Eq. (140), we obtain the interesting result

$$\frac{I_m(\varphi_0, 0)}{I_m(0, 0)} = \frac{2}{3} \rightarrow -1.8 \text{ dB} \tag{141}$$

This implies that for a specified value of  $\varphi_0$ , the directivity goes through a maximum as  $\xi$  is increased. This maximum occurs at  $\xi_m = 3\varphi_0^2$ . For larger values of  $\xi$ , the pattern is more uniformly flat but low in directivity throughout. On the other hand, if  $\xi$  is smaller, the pattern is narrower, and although the peak directivity is higher, it drops off too rapidly at

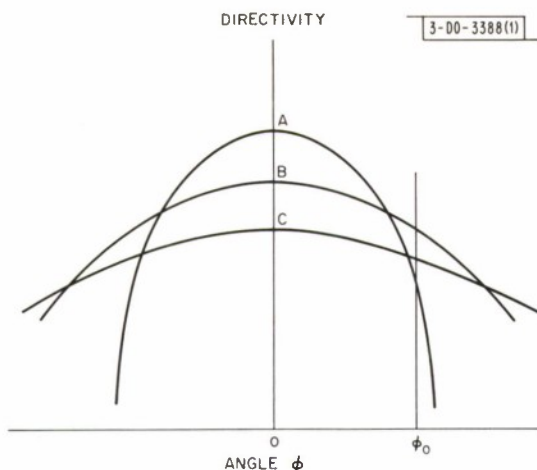


Fig. 89. Different directivity patterns available from single antenna system illustrating interdependence of beam width and directivity.

increasing values of  $\varphi$ . The various situations are illustrated in Fig. 89 with three directivity patterns A, B and C of increasing beamwidth. For the specific value of  $\varphi_0$  shown, pattern B is the best choice. At another value, one of the other patterns might have been a better choice. A second point now comes to mind. Suppose two arbitrary angles  $\varphi_0$  are chosen and the corresponding optimum patterns compared. We will find the reduction in directivity [Eq. (141)] the same for both, seemingly as if the one pattern could be scaled on the  $\varphi$ -axis to coincide with the other where the values of  $\varphi_0$  are matched. The pattern with the smaller  $\varphi_0$  value will have the higher directivity throughout, of course.

In this latter discussion, an antenna pattern with a simple form was assumed and, consequently, the accuracy of the conclusions comes into question. Let us then suppose that the fields  $I_m(\varphi_0, 0)$  and  $I_m(0, 0)$  are the maximum that one can obtain from a realistic situation, rather than from the simplified situation considered. It can at least be stated that if angle  $\varphi_0$  is decreased,  $I_m(\varphi_0, 0)$  and  $I_m(0, 0)$  both increase since now the radiated energy is concentrated in a smaller angle. But we may wonder if the ratio remains unchanged, say, at some value which is not necessarily  $\frac{2}{3}$ . If the answer is affirmative for the cases in which we are interested, it provides a significant aid to the pattern selection. This point will be clarified later.

## B. Arrangements of Antenna Excitations and Beams

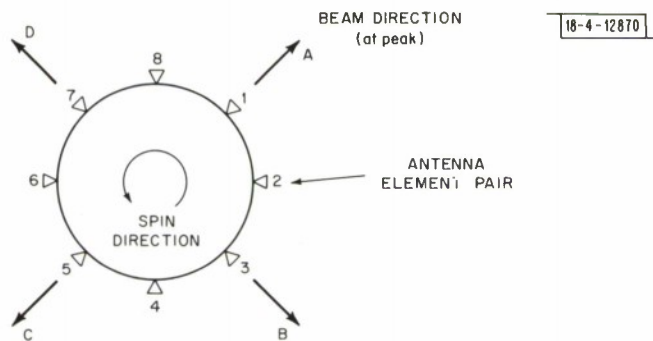
In any scheme implemented on the satellite for generating the antenna patterns,  $m = 1, 2, 3$  or 4 adjacent element pairs will be excited at a time. More than four is not feasible since radiation from two of the ON elements is in diametrically opposite directions. For  $m = 1$ , only one pattern exists insofar as change in the phase or amplitude is concerned. (Henceforth, when reference is made to the phase or amplitude, it is implicit that it concerns the field excitation of the antenna element pair. It will be the same for each element of the pair so that the pattern is symmetrical about the satellite equator.) For  $m = 2$ , the peak gain of the pattern will be higher than for  $m = 1$  and will be highest when the amplitudes are equal. That is to say, reducing the amplitude of one antenna pair caused the pattern to look more like the  $m = 1$  case. Altering the relative phase causes the beam to shift direction within limits. If the phase difference becomes large, the pattern degrades since the signals are in phase at an angle where the gains of the individual element patterns have values below the peak.

With  $m = 3$ , having the three amplitudes equal could produce a higher peak gain than for  $m = 2$ . It is also possible that having unequal amplitudes could further enhance the gain by exciting, for example, the middle element with a higher amplitude than the elements on either side. On the other hand, changing the amplitude of one of the outer element pairs relative to the other two should cause the pattern to approach that of the  $m = 1$  or  $m = 2$  case. Like the  $m = 2$  case, the beam can be aimed within limits by appropriate phasing. For  $m = 4$ , it cannot be intuitively decided whether higher gains can be obtained since two element pairs face directions  $135^\circ$  apart, quite a large value. It is reasonable to assume that the peak gain is highest when the two middle

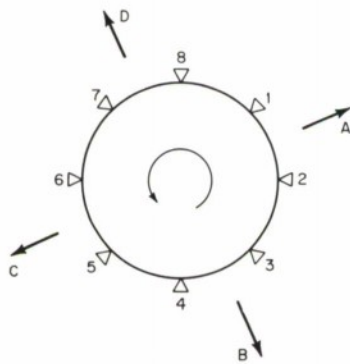
element pairs are excited equally, and the outer pairs are also equal but possibly at another level.

Each of the patterns that exist for each of these several cases has a beam width (measured at some value, say XdB, below the peak) associated with it. This value will give a fairly good indication of the directivity but not an exact one due to slight variations in the pattern shape and the side lobes. Hence, the pattern will be near optimum for some angle  $2\varphi_0$ . That is to say, while in the last section the angle  $2\varphi_0$  was specified and the best pattern was to be determined, now the pattern is given and the problem is to find the angle  $2\varphi_0$  for which the given pattern agrees approximately with the optimum pattern. Having accomplished this, the value of  $n$  can then be found by Eq. (107). A definite relation between the number of beams to design the satellite for and the number of antenna elements to excite at a time has then been established.

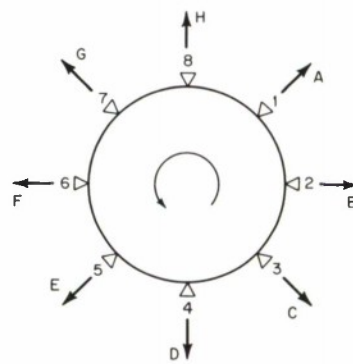
In those cases where  $n = 4, 8, 12$  or  $16$ , the arrangement of the beams is compatible with the arrangement of the antennas around the satellite. These cases are pictured in Fig. 90(a) to (g). The antenna elements are numbered consecutively and beams lettered consecutively (with the letter I omitted). The directions representing the beams correspond to the center of the



(a)  $n = 4$  beams aligned with antennas.



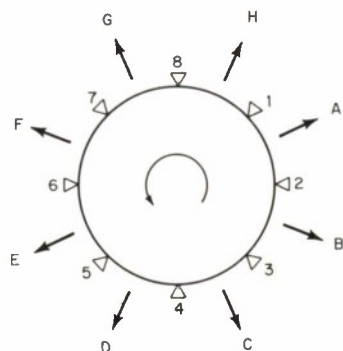
(b)  $n = 4$  beams midway between antennas.



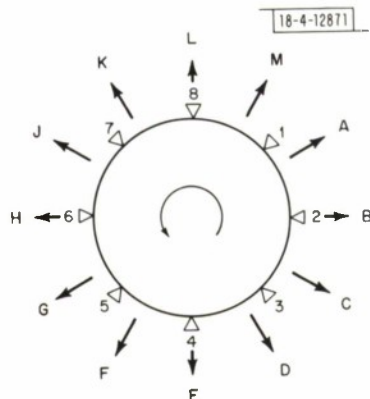
(c)  $n = 8$  beams aligned with antennas.

Fig. 90. Considered arrangements of equally spaced beam directions relative to satellite antenna positions.

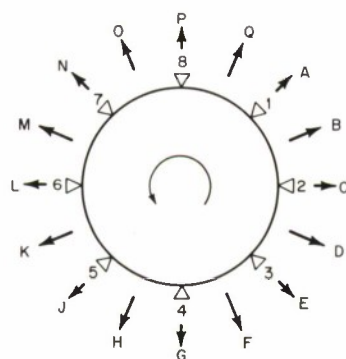




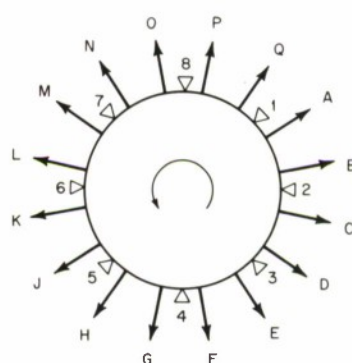
(d)  $n = 8$  beams midway between antennas.



(e)  $n = 12$  beams, every third of which is aligned with an antenna.



(f)  $n = 16$  beams aligned and midway between antennas.



(g)  $n = 16$  beams with antennas midway between pairs.

Fig. 90. Continued.

coverage angle delineated in Fig. 87. If  $n = 4$  or  $n = 8$ , the beams will align with the antenna elements [Fig. 90(a) or (c)], or fall midway between them [Fig. 90(b) or (d)], if the beams are to be placed symmetrically with respect to the antennas. If  $n = 12$ , every third beam aligns with every second antenna [Fig. 90(e)]. If  $n = 16$ , the beams are aligned with the antennas and the midway points [Fig. 90(f)], or placed so that antennas are midway between beams [Fig. 90(g)].

Various feasible arrangements of antenna excitations are tabulated below, where each entry, labeled with a letter, gives the figure number, value of  $n$ , beam, and in parentheses the antennas that are excited to produce that beam.

A [Fig. 90(a)],  $n = 4$ : A(1); B(3); C(5); D(7).

Here only one antenna is ON at a time and half the antennas are not used.

B [Fig. 90(a)],  $n = 4$ : A(8, 1, 2); B(2, 3, 4); C(4, 5, 6); D(6, 7, 8).

It is unlikely that three element pairs are needed to produce the pattern which is optimum for the  $107^\circ$  width.

C [Fig. 90(b)],  $n = 4$ : A(1, 2); B(3, 4); C(5, 6); D(7, 8).

D [Fig. 90(b)],  $n = 4$ : A(8, 1, 2, 3); B(2, 3, 4, 5); C(4, 5, 6, 7); D(6, 7, 8, 1).

E [Fig. 90(c)],  $n = 8$ : A(1); B(2); C(3); D(4)... .

F [Fig. 90(c)],  $n = 8$ : A(8, 1, 2); B(1, 2, 3); C(2, 3, 4); D(3, 4, 5)... .

G [Fig. 90(c)],  $n = 8$ : A(1, 2); B(1, 2); C(3, 4); D(3, 4)... .

G is an example where two beams are obtained from the same two elements by appropriate phasing.

H [Fig. 90(d)],  $n = 8$ : A(1, 2); B(2, 3); C(3, 4); D(4, 5)... .

J [Fig. 90(d)],  $n = 8$ : A(1, 2, 3); B(1, 2, 3); C(3, 4, 5); D(3, 4, 5)... .

K [Fig. 90(d)],  $n = 8$ : A(8, 1, 2, 3); B(1, 2, 3, 4); C(2, 3, 4, 5); D(3, 4, 5, 6)... .

L [Fig. 90(e)],  $n = 12$ : A(1, 2); B(1, 2); C(2, 3); D(3, 4); E(3, 4)... .

M [Fig. 90(e)],  $n = 12$ : A(8, 1, 2); B(1, 2, 3); C(1, 2, 3); D(2, 3, 4)... .

N [Fig. 90(f)],  $n = 16$ : A(1, 2); B(1, 2); C(1, 2); D(2, 3); E(3, 4)... .

O [Fig. 90(f)],  $n = 16$ : A(8, 1, 2); B(1, 2, 3); C(1, 2, 3); D(1, 2, 3); E(2, 3, 4)... .

P [Fig. 90(g)],  $n = 16$ : A(1, 2); B(1, 2); C(2, 3); D(2, 3)... .

Q [Fig. 90(g)],  $n = 16$ : A(8, 1, 2); B(1, 2, 3); C(1, 2, 3); D(2, 3, 4)... .

R [Fig. 90(g)],  $n = 16$ : A(8, 1, 2, 3); B(8, 1, 2, 3); C(1, 2, 3, 4); D(1, 2, 3, 4)... .

There are other arrangements, but they are generally either clumsy, that is, not easily adaptable to a switching logic circuit, somewhat like L above, or show no advantage over another arrangement such as N with P.

### C. Calculated Antenna Patterns

Directivity patterns<sup>21</sup> were calculated at  $\Theta = 0$  and frequency  $f_T$  for the slot antennas using the satellite dimensions quoted in Sec. I. The concern for optimizing the pattern is principally at the frequency at which the satellite transmits its signal since its power output is limited, whereas

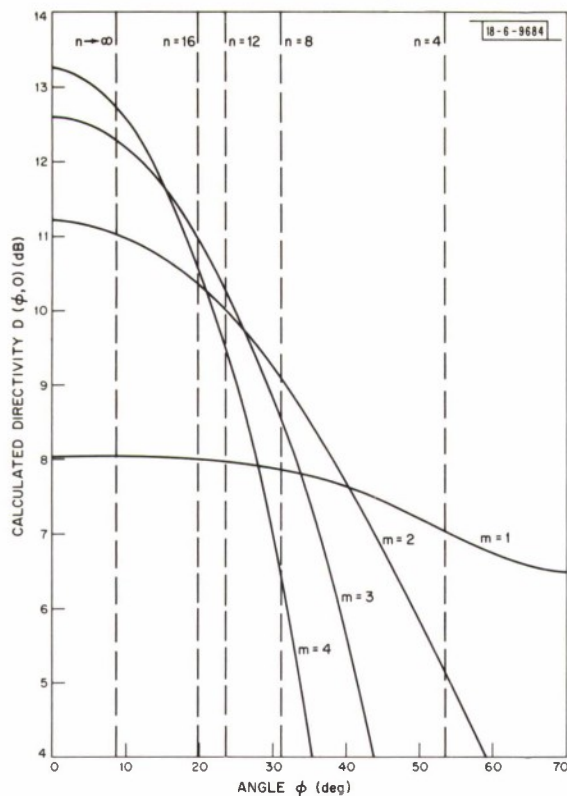
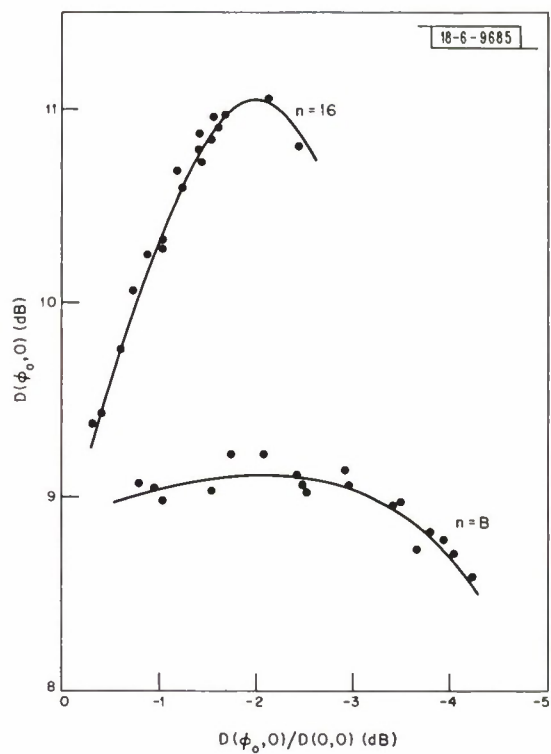


Fig. 91. Calculated directivity patterns along the  $\phi$ -axis for  $m = 1, 2, 3$  and  $4$  antennas excited with signals of equal amplitude and phase determined by a plane wave requirement. Vertical lines for  $n = 4, 8, 12, 16$  and  $\infty$  beams mark limit of angle of coverage as given by Eq. (107).

Fig. 92. Directivity calculated at  $\phi_0$  corresponding to  $n = 8$  and  $n = 16$  for a number of antenna excitations as a function of difference (in dB) between this directivity and peak value.



presumably any slight reduction in gain at the receive frequency can be compensated for at the ground terminal. Some of the optimum patterns were recalculated at frequency  $f_R$  to provide a measure of the change in directivity with frequency, and the change at angle  $\varphi_0$  was found to be less than 0.2 dB.

Four patterns are plotted in Fig. 91 in terms of the directivity  $D(\varphi, 0)$  showing only a part of the main lobe. One pattern,  $m = 1$ , is of a single slot pair. The other three patterns,  $m = 2, 3$ , and  $4$ , are based on the conditions that the amplitudes of the excitations are equal and the phases adjusted so that the signals arrive in phase at a plane whose normal is centrally located among the ON antennas. On the same figure, angle  $\varphi_0$ , given by Eq. (107), is plotted for the  $n$  with values  $4, 8, 12, 16$ , and  $\infty$ . It is evident that if the choice is limited to the four patterns, for  $n = 4$ , pattern  $m = 1$  is the best choice; for  $n = 8$ , the choice is pattern  $m = 2$ ; for  $n = 12$  or  $16$ , it is pattern  $m = 3$ ; and for  $n = \infty$ , it is pattern  $m = 4$ . It can be noted in addition that in the cases  $n = 8, 12$ , and  $16$ , for the best pattern  $I(\varphi_0, 0)/I(0, 0) = D(\varphi_0, 0)/D(0, 0) \rightarrow -2.1 \text{ dB}, -2.3 \text{ dB}$  and  $-1.7 \text{ dB}$ , respectively. These values are not too different from the values of  $-1.8 \text{ dB}$  given in Eq. (141).

Either pattern,  $m = 3$  or  $m = 4$ , can be broadened or narrowed if the relative amplitudes or phases are changed. There are thus any number of alternative patterns to those in Fig. 91. On the other hand, the calculated patterns are not accurate due to the neglect of the mutual coupling between antennas. In other words, given  $n$ , a number of patterns can be calculated to obtain  $D(\varphi_0, 0)$  and the one that has the largest value  $D_m(\varphi_0, 0)$  chosen, but the result may not be the same as one obtained by actual pattern measurements. Suppose, however, that there are two patterns, one calculated and one measured, whose main lobes have about the same shape. (They may arise from different antenna excitations.) If the calculated pattern is optimum, then the measured pattern will also be nearly optimum, and the ratio  $D_m(\varphi_0, 0)/D_m(0, 0)$  will be about the same in the two cases. If this ratio can be calculated, then it can be applied to a measured pattern to find the angle  $\varphi_0$  for which it is optimum. The alternate procedure of measuring many patterns and comparing the directivities at a specified angle  $\varphi_0$  involves considerably more effort.

Many patterns were calculated, and the directivities  $D(\varphi_0, 0)$  plotted versus  $D(\varphi_0, 0)/D(0, 0)$  for the two cases,  $n = 8$  and  $n = 16$ . The plot is shown in Fig. 92. Except for some scattering of points, there is a well defined trend. Both curves exhibit a maximum directivity  $D_m(\varphi_0, 0)$  at approximately  $D(\varphi_0, 0)/D(0, 0) \rightarrow -2.0 \text{ dB}$ . This is in good agreement with the value of  $-1.8 \text{ dB}$  determined mathematically [Eq. (141)]. In conclusion, the ratio  $D(\varphi_0, 0)/D(0, 0) \rightarrow -2.0 \text{ dB}$  can be applied to a measured pattern to determine angle  $\varphi_0$ , and therefore  $n$ , by Eq. (107). One of the plans given in Fig. (90) can then be chosen and the switch configuration derived.

It can incidentally be noted in both Figs. 91 and 92 that in going from  $n = 8$  to  $n = 16$  beams, an increase in directivity of about 2 dB can be expected. Figure 91 also shows that possibly another 2 dB increase would be obtained if the satellite had been designed to operate in a continuous scan mode (corresponding to  $n \rightarrow \infty$ ).

#### D. Pattern Measurements

A satellite antenna model was set up for pattern measurements. The results of these measurements as well as those of the flight satellite are reported elsewhere, together with details of the slot and dipole configurations.<sup>1,10</sup> A few typical patterns are reproduced here which are relevant to this discussion.



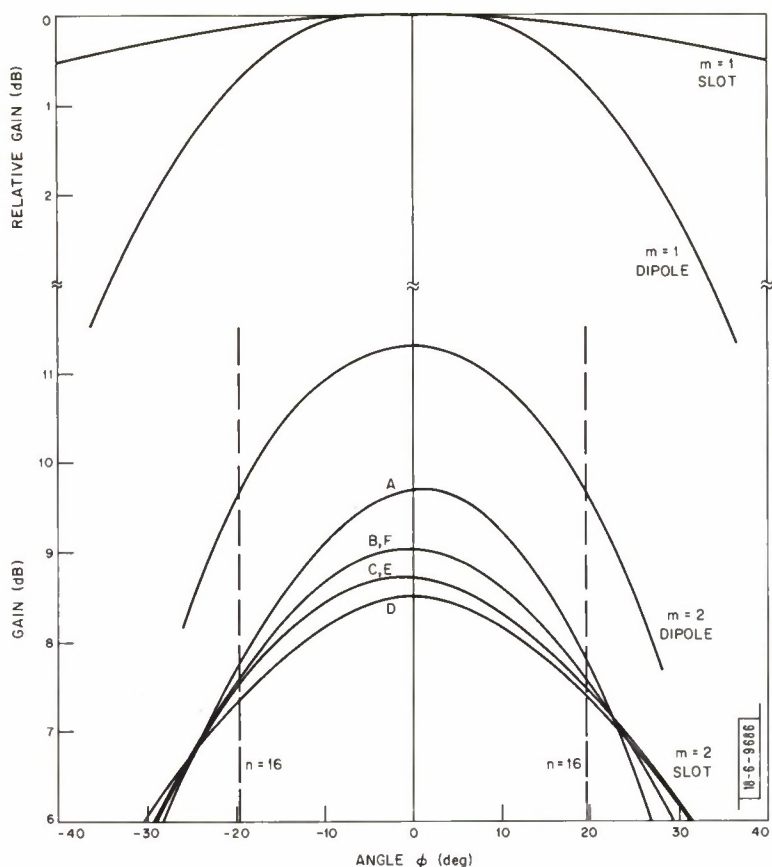


Fig. 93. Measured values of gain of satellite antenna model where 1 dipole pair, 1 slot pair (relative gain values), 2 dipole pairs, and 2 slot pairs are excited. Latter case varies with position of open-circuit termination of unexcited slots. Trend is from pattern A through B, C, D, E, F, and back to A again.

The patterns of one slot pair and one dipole pair at frequency  $f_T$  are shown at the top of Fig. 93; both are plotted on a scale where their peaks are arbitrarily set at 0 dB. The slot pattern depends to some extent on the terminations of the other seven slot pairs because of the mutual coupling; the pattern in Fig. 93 is typical. The effect of mutual coupling on the dipole pattern is negligible. The slot pattern agrees fairly well with the calculated pattern in Fig. 91, but the dipole pattern is somewhat narrower.

The patterns at the bottom of Fig. 93 show the gains of two dipole pairs and two slot pairs as measured at the input to the cable that would be connected to the triplexer. Hence, it includes cable and power divider losses. Because of differences in configuration and matching technique, the dipole pattern has about 1.6 dB higher gain than the slot pattern. Considering first the dipole pattern, the ratio  $D(\phi, 0)/D(0, 0)$  is  $-2.0$  dB at  $\phi = 21\frac{1}{2}^\circ$  and therefore the optimum  $n$  is about 14. If  $n$  is set equal to 16 as indicated by the vertical lines in the figure, the ratio  $D(\phi, 0)/D(0, 0)$  has the value  $-1.7$  dB which should be satisfactory.

In the case of the slots, the pattern depends on the termination of those slot pairs that are not directly excited, because of mutual coupling. In the satellite system, this termination would be approximately an open circuit at the output ports of the switch matrix. Thus for these pattern measurements, movable open (and short) circuits on the unexcited slot pairs were run through a series of positions, where the six distances were kept equal. Four of the measured patterns,

A, B, C, and D, are shown in Fig. 93. (Relative values of line lengths on unexcited slot pairs were 24, 21, 17, and 13 inches, respectively.) Pattern A is the one found to have the highest peak gain. Then the pattern trend is through B, C, and to D which has the lowest peak, 1.2 dB below that of pattern A. Continuing to slide the open circuits, the trend reverses to exhibit patterns E and F which are similar to C and B, and finally A is attained again.

Pattern D has nearly the same appearance as the calculated pattern  $m = 2$  in Fig. 91. It is somewhat broader than the ideal for  $n = 16$ . Pattern A shows  $D(\varphi, 0)/D(0, 0) = -2.0$  dB at  $n = 16$  and therefore  $n = 16$  is just the optimum for this pattern. We note, incidentally, that these patterns all intersect at about 2 dB below the average of the peaks. This provides a rough check on our accepted value of the optimum directivity ratio.

Why the pattern can be controlled by the position of the open circuits of the unexcited slot pairs is qualitatively explained by supposing that RF energy coupled to these slots is reflected and reradiated, and hence affects the pattern. The phase of the reradiated signal can be adjusted to enhance the peak gain. The pattern approaches the  $m = 4$  pattern in Fig. 91 because this situation is similar to exciting four or more slot pairs directly when there is no mutual coupling.

These points raise an interesting possibility. If the pattern can be controlled somewhat by the mutual coupling, it ought to be more directly controllable by the deliberate coupling of some energy between lines which feed adjacent antennas, such as by capacitors or directional couplers. In the case under discussion, the mutual coupling is sufficient to provide the optimum pattern; but in another system, additional internal coupling may be used to obtain a more desirable pattern. This means that fewer antennas need be excited directly and consequently, the system needed to rotate an antenna beam can be simplified.

Slot and dipole patterns measured along the  $\theta$ -axis are shown in Fig. 94. The vertical lines mark the north and south edge of the earth. The ratio  $D(0, \theta)/D(0, 0)$  is about  $-0.8$  dB at  $\theta = 8\frac{1}{2}^\circ$  for both patterns. It is then likely that the patterns are broader and therefore of lower gain than the ideal pattern.

#### E. Choice of Configuration for the Switch Matrix

The plan that now seems to be a good choice is to generate 16 beams where two antennas at a time are excited. This is either plan N or P of those tabulated earlier. Plan N requires a more involved switching scheme and has no apparent advantage. It is therefore rejected. Plan P is the one that is adopted and the antenna and beam positions are as displayed in Fig. 90(g). With this decision made, the switch circuit chosen is that shown in Fig. 5(a), and its operation is described in Sec. II-A.

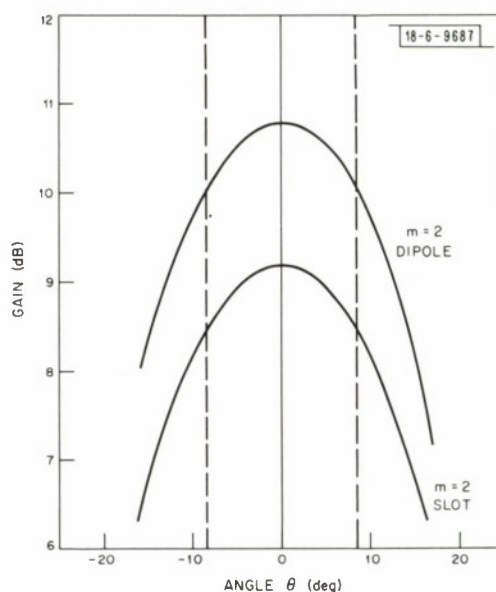


Fig. 94. Measured gain along  $\theta$  axis for two dipole pairs or two slot pairs excited simultaneously. Vertical dashed lines mark angle subtended by earth's diameter.

As indicated in Sec. IV-B, for each diode that the RF signal passes through, there is an insertion loss of about 0.2 dB. In addition, there is about 0.1 dB loss due to radiation leakage out of the OFF ports as well as other incidental losses. This switch matrix will then have a total insertion loss of about 0.5 dB. This value, together with those in the patterns of Fig. 93, show that the net expected antenna gain at angle  $\varphi_0$  is  $9.6 - 0.5 = 9.1$  dB for the dipoles and 7.2 dB for the slots.

Let us digress for the moment and indicate what gain would have been expected if another switching scheme had been chosen, namely, if the number of beams had been  $n = 12, 8$  or  $4$ . Switch configurations have been worked out for some of these schemes and evaluated. If  $n = 12$ , there is a decrease in gain over the  $n = 16$  case. There are no conceivable simplifications in the switch matrix so this scheme has no advantage. If  $n = 8$ , plan H (described in Sec. XII-B) would be used. The corresponding switch matrix is the same as the one that was finally chosen but with the omission of the 2P2T section (i.e., now consisting of a power divider and two SP4T sections). The switch loss is then only about 0.3 dB, but the decrease in directivity is about 2 dB. Therefore, the gain is reduced 1.7 dB from the adopted case (resulting in a final gain value of 5.5 dB for the slots). Although the 2P2T section and its bias supply are absent, it was felt that this was not enough justification to accept the decreased gain. If  $n = 4$ , the pattern  $m = 1$  has higher gain than the pattern  $m = 2$  (see Fig. 94). The reduction in gain is over 3 dB, too large to warrant using this scheme. For completeness, we shall mention that if the satellite had been designed to have an omnidirectional pattern for which no switch was used, the estimated gain would be 2.6 dB and 1.0 dB for the dipoles and slots, respectively. Hence, by using a switch matrix scheme, the gain has been increased by over 6 dB.

### XIII. CONCLUSIONS

A UHF switch matrix was designed, developed, and tested for incorporation in a satellite. It had acceptable characteristics after it was tested and altered to meet a number of conflicting requirements. These included limits on the magnitude of the intermodulation product and switching noise amplitudes, a negligible noise figure, no evidence of multipactor or deterioration due to electron and proton radiation, and expected good reliability over a five-year lifetime while being subjected to high RF power levels. Now, a year after the satellite launch, the switches continue to operate normally, a tribute we believe due to the exhaustive testing described in this report.

### ACKNOWLEDGMENTS

A considerable portion of the work described in this report was done by R. L. Sicotte. In particular, he shared in resolving many of the intermodulation and switching noise problems, and carried out all the reliability life tests. The author wishes to thank B. F. LaPage for providing leadership throughout much of this work, D. Carberry and D. K. VanderKlish for carrying out many of the electrical measurements, and D. M. Nathanson for contributing significantly to the solution of the thermal problems. Gratitude is extended to many others, too numerous to list, for their cooperation in the mechanical design, development and testing efforts under the direction of D. R. Bold.

## APPENDIX A

### SUMMARY OF CHARACTERISTICS OF LES-6 SWITCHES



TABLE A-1  
SCAN MODE CHARACTERISTICS OF FLIGHT SWITCH FOR DIPOLES\*

SWITCH WITHOUT HYBRID																
Characteristic	Input at Diodes j and k								Input at Diodes l and m							
	ON Beam								ON Beam							
	A	B	E	F	J	K	N	O	A	B	E	F	J	K	N	O
VSWR																
$f_T$	1.21	1.20	1.19	1.22	1.23	1.24	1.22	1.24	1.18	1.22	1.21	1.16	1.22	1.22	1.20	1.17
$f_R$	1.31	1.29	1.26	1.36	1.29	1.30	1.26	1.34	1.26	1.34	1.30	1.27	1.28	1.33	1.31	1.28
Insertion loss (dB) to ON port																
$f_T$	0.51	0.46	0.50	0.47	0.48	0.48	0.48	0.47	0.45	0.50	0.46	0.47	0.49	0.48	0.48	0.48
$f_R$	0.68	0.64	0.66	0.63	0.66	0.66	0.64	0.65	0.59	0.65	0.59	0.62	0.63	0.62	0.61	0.63
Isolation† (dB)																
$f_T$	21.1	20.6	19.5	20.1	20.6	21.8	21.0	21.4	20.6	21.4	20.4	19.4	22.0	20.5	21.0	21.0
$f_R$	19.8	19.1	18.2	19.0	19.1	20.2	19.4	19.7	19.1	20.0	19.8	18.2	20.3	19.2	19.8	19.4
SWITCH CONNECTED TO HYBRID																
Characteristic	Beam															
	A	B	C	D	E	F	G	H	J	K	L	M	N	O	P	Q
Phase difference of two outputs (deg)																
$f_T$	45.0	46.1	45.2	45.4	45.4	45.7	47.0	44.6	45.1	47.0	47.1	45.4	45.2	47.0	46.8	44.8
$f_R$	35.6	35.0	34.0	36.4	36.2	34.5	35.8	35.4	36.0	35.8	36.0	36.1	35.8	36.0	35.6	35.6
15th order IM (dBm)																
$P_T = 45.5$																
$P_B = 31.5$																
$T = +60^\circ\text{C}$	-	-	-	-	-	-	-	-	-	-	-	-	-	-	-	-
$T = +10^\circ\text{C}$	-	-	-	-	-	-	-	-	-	-	-	-	-	-	-	-
$T = -40^\circ\text{C}$	-138	-131	-133	-	-138	-133	-134	-138	-139	-135	-135	-	-140	-134	-132	-134
15th order IM (dBm) with 63° phase difference																
$T = +60^\circ\text{C}$	-	-	-	-	-	-	-	-	-	-	-	-	-	-	-	-
$T = +10^\circ\text{C}$	-	-	-	-136	-137	-	-	-135	-133	-	-	-133	-133	-	-	-133
$T = -40^\circ\text{C}$	-133	-127	-126	-132	-132	-127	-129	-133	-133	-129	-131	-134	-131	-131	-129	-130
Switching noise (dBm) in 7-MHz band at $f_R$																
$T = +10^\circ\text{C}$																
		-76	-75	-75		-75	-75	-72		-72	-74	-66		-75	-73	
* See Sec. III-D for further characteristics.																
† The isolation as defined here is the decrease in signal going out of the port that is ON when the beam indicated is switched to another. The beam is switched to the one for which the decrease is smallest.																
‡ Values below -140 dBm were undetermined.																
§ Values given are the largest observed of 15 traces. Only beams exhibiting larger values are given.																

TABLE A-2  
SCAN MODE CHARACTERISTICS OF FLIGHT SWITCH FOR SLOTS

Characteristic		SWITCH WITHOUT HYBRID															
		Input at Diodes j and k								Input at Diodes l and m							
		ON Beam								ON Beam							
		A	B	C	D	E	F	J	K	N	O	A	B	C	D	E	F
VSWR																	
$f_T$		1.14	1.10	1.09	1.11	1.11	1.15	1.11	1.11	1.12	1.10	1.09	1.14	1.10	1.10	1.11	1.16
$f_R$		1.34	1.32	1.34	1.34	1.34	1.35	1.34	1.34	1.34	1.34	1.32	1.32	1.32	1.32	1.32	1.30
Insertion loss (dB) to ON port																	
$f_T$		0.46	0.44	0.43	0.43	0.43	0.46	0.44	0.44	0.47	0.42	0.41	0.42	0.39	0.38	0.41	0.43
$f_R$		0.59	0.59	0.56	0.56	0.56	0.61	0.55	0.55	0.60	0.57	0.52	0.53	0.49	0.50	0.54	0.59
Isolation* (dB)																	
$f_T$		20.4	21.3	19.3	20.8	20.5	20.5	20.6	21.2	21.0	21.0	21.0	21.0	20.4	19.2	20.6	19.6
$f_R$		18.6	19.4	19.4	17.6	18.4	18.4	19.1	19.6	18.3	18.3	18.8	18.6	18.2	17.2	17.6	17.0
		SWITCH CONNECTED TO HYBRID															
		Beam															
		A	B	C	D	E	F	G	H	J	K	L	M	N	O	P	Q
Phase difference at two outputs (deg)																	
$f_T$		45.3	47.8	47.8	45.8	47.2	46.0	46.2	47.0	46.5	46.1	46.0	46.4	46.0	46.9	46.7	46.3
$f_R$		37.3	35.2	35.4	37.6	36.9	35.8	36.4	35.2	35.6	36.0	35.5	36.9	35.2	36.6	36.3	35.9
15th order IM (dBm)																	
$P_T = 45.5$																	
$P_B = 31.5$																	
$T = +60^\circ\text{C}$		†	-	-	-	-	-	-	-	-	-	-	-	-	-	-	-
$T = +10^\circ\text{C}$		-	-	-	-	-	-	-	-	-	-	-	-	-	-	-	-
$T = -40^\circ\text{C}$		-139	-139	-	-139	-	-	-	-	-139	-	-	-138	-140	-	-139	-140
Switching noise (dBm) in 7-MHz band at $f_T$																	
$T = +10^\circ\text{C}$																	
		-68															
		-72															

† The isolation as defined here is the decrease in signal going out of the port that is ON when the beam indicated is switched to another. The beam is switched to the one for which the decrease is smallest.

‡ Values below -140 dBm were undetermined.

§ Values given are the largest observed of 15 traces. Only beams exhibiting larger values are given.

## APPENDIX B

TABLE 8-1 PARAMETERS OF DIODES USED IN FLIGHT SWITCHES*						
Diode	Total Capacitance ( $V_R = 50$ V $f = 1$ MHz) (pF)	Series Resistance ( $I_F = 100$ mA $f = 500$ MHz) (ohms)	Reverse Bias Current (V)	Thermal Resistance $\theta_i$ ( $^{\circ}\text{C}/\text{W}$ )	15th Order IM at $-40^{\circ}\text{C}$ (dBm)	Switching Noise at Ambient T
						OFF to ON (dBm)      ON to OFF (dBm)
Dipole Switch						
a	0.80	0.56	900	29	—	-73      -74
b	0.89	0.59	1000+	16.6	—	-74      -85
c	0.88	0.44	900	22.7	—	-60      -78
d	0.79	0.50	1000	15.6	—	-77      -72
e	0.74	0.50	1000+	14.3	—	-74      -74
f	0.88	0.63	875	17.8	—	-85      -80
g	0.87	0.44	900	25	—	-66      -65
h	0.86	0.47	975	15.6	—	-69      -73
i	0.83	0.47	900	17.8	—	-66      -67
k	0.81	0.53	900	18.5	—	-80      -71
l	0.83	0.44	875	14.7	-133	-66      -77
m	0.89	0.47	925	15.1	-139	-63      -71
Slot Switch						
a	0.63	0.66	900	20	—	-77      -74
b	0.83	0.56	800	14.3	—	-78      -77
c	0.71	0.56	920	23.8	—	-77      -74
d	0.82	0.47	775	19.2	-139	-68      -68
e	0.87	0.66	1000	28	—	-83      -80
f	0.83	0.53	900	21.7	—	-77      -80
g	0.86	0.66	1000	15.6	—	-87      -78
h	0.83	0.56	1000	13.9	—	-80      -80
i	0.62	0.59	1000	17.8	—	-87      -77
k	0.70	0.63	1000+	14.7	—	-80      -80
l	0.83	0.50	1000	12.2	—	-74      -74
m	0.81	0.44	820	14.7	—	-72      -71
* The material in the first four columns was provided by the manufacturer (after screening). IM and switching noise were measured at $P_T = 43$ dBm and $P_B = 28.5$ .						



APPENDIX C  
QUALITY ASSURANCE SCREENING SPECIFICATIONS  
FOR PIN DIODE FOR LES-6 SWITCH MATRIX

## SCOPE

This specification and individual test specifications establish requirements for nondestructive screening inspection of electronic parts on a 100-percent basis.

## REQUIREMENTS

### General

Throughout all the tests and inspection, special handling precautions must be exercised to prevent damage or contamination of the diodes or their markings.

Each diode shall be marked for identification by a number scribed on the small circular area at the anode end.

All the diodes of the lot are to be subjected to all the tests given with the exception that tests are discontinued on those diodes that become defective.

The test documentation shall contain a complete history of each diode, including the values of parameters measured at all points, tests performed, and disposition. A copy of all documentation (including the X-ray films) shall accompany the component shipment.

Inspections and tests shall be performed under ambient conditions ( $21^{\circ}\text{C} \pm 3^{\circ}\text{C}$ ) unless specified otherwise. Measured values should be given with sufficient accuracy to be meaningful.

Listed are six groups of tests, each concluded with measurements of electrical characteristics.

The diodes are grouped in Lot 1 or Lot 2 according to the request of Lincoln Laboratory and tested accordingly.

<u>Group A</u>				
<u>Test Number</u>	<u>MIL Standard</u>	<u>Method</u>	<u>Name</u>	<u>Details</u>
1	750A	2071	Visual and Mechanical Examination	Note also wear, contamination or flaking of the gold plating
2	750A	2066	Physical Dimensions	Product specification OD-S-30
3	750A	4011.1	Forward Current and Forward Voltage	$I_F = 50 \text{ mA DC}$
4	750A	4016.1	Reverse Current and Reverse Voltage	$V_R = 400 \text{ V DC}$
5			Capacitance	$V_R = 50 \text{ V DC},$ $f = 1 \text{ MHz}$
6			Series Resistance	$I_F = 100 \text{ mA DC},$ $f = 500 \text{ MHz}$
7			Thermal Resistance	

Group B

<u>Test Number</u>	<u>MIL Standard</u>	<u>Method</u>	<u>Name</u>	<u>Details</u>
8	202C	107B	Thermal Shock	Test condition B
9	750A	1056.1	Thermal Shock (Strain)	Test condition B

Allow one hour at ambient conditions before continuing.

10				Repeat No. 3
11				Repeat No. 4

Group C

<u>Test Number</u>	<u>MIL Standard</u>	<u>Method</u>	<u>Name</u>	<u>Details</u>
12	750A	2056	Vibration, Variable Frequency	Lower frequency limit 20 Hz. Each orientation – one traverse – 15 minutes. X <sub>1</sub> and Z <sub>1</sub> orientations.
13	750A	2016.1	Shock	6 blows of 200 g's. Duration 2 ms. X <sub>1</sub> and Z <sub>1</sub> orientations.
14	202C	112	Seal	Test condition C. Procedure III (omitting A or B test).
15	750A	1001.1	Barometric Pressure, Reduced	Test condition D. V <sub>R</sub> = 100 V DC.
16	202C	209	Radiographic Inspection	
17				Repeat No. 3
18				Repeat No. 4

Group D

<u>Test Number</u>	<u>MIL Standard</u>	<u>Method</u>	<u>Name</u>	<u>Details</u>
19	750A	1031.1	High Temperature Life	
			Lot 1	240 hours at 100°C
			Lot 2	336 hours at 100°C

Allow one hour at ambient conditions before continuing.

20				Repeat No. 3
21				Repeat No. 4

Group E

<u>Test Number</u>	<u>MIL Standard</u>	<u>Method</u>	<u>Name</u>	<u>Details</u>
22	750A	1026.1	Steady Operation Life	
			Lot 1	216 hours at $I_F = 50 \text{ mA DC}$
			Lot 2	288 hours at $I_F = 50 \text{ mA DC}$
23				Repeat No. 3
24				Repeat No. 4

Group F

<u>Test Number</u>	<u>MIL Standard</u>	<u>Method</u>	<u>Name</u>	<u>Details</u>
25			High Temperature Reverse Bias	48 hours at $T = 100^\circ\text{C}$ $V_R = 100 \text{ V DC}$

Allow one hour at ambient conditions but continuing to maintain  $V_R = 100 \text{ V DC}$  until Number 26 test is performed.

26				Repeat No. 4
27				Repeat No. 3
28				Repeat No. 5
29				Repeat No. 6
30				Repeat No. 7
31				Repeat No. 1

## REFERENCES

1. R.N. Assaly, M.E. Devane, B.F. LaPage, M.L. Rosenthal and A. Sotiropoulos, "LES-6 Antenna System," Technical Report 465, Lincoln Laboratory, M.I.T. (10 March 1969), DDC AD-693197.
2. R.P. Nanavati, An Introduction to Semiconductor Electronics (McGraw-Hill, New York, 1963).
3. H.A. Watson, Microwave Semiconductor Devices and Their Circuit Applications (McGraw-Hill, New York, 1969).
4. R.W. Peters (editor), Handbook of Tri-plate Microwave Components (Sanders Associates, Inc., 1956).
5. S.B. Cohn, "Problems in Strip Transmission Lines," Trans. IRE, Microwave Theory and Techniques, MTT-3, 119-126 (March 1955).
6. J. Swift, "Strip Transmission Lines," Electronic Engineering 39, 490-494 (August 1967).
7. N. Marcuvitz (editor), Waveguide Handbook, Vol. 10, Radiation Laboratory Series (McGraw-Hill, New York, 1949).
8. A.D. Sills, "Properties of Strip Transmission Line," Vols. I and II, Clearing House for Federal Scientific and Technical Information, U.S. Department of Commerce (October 1964), DDC AD-614035 and AD-614036.
9. M.E. Devane, D.J. Frediani, B.F. LaPage, M.L. Rosenthal and A. Sotiropoulos, "Antenna System for LES-5," Technical Report 451, Lincoln Laboratory, M.I.T. (18 July 1968), DDC AD-684167.
10. M.L. Rosenthal, M.E. Devane and B.F. LaPage, "VHF Antenna Systems for Spin-Stabilized Satellites," Trans. IEEE, Antennas and Propagation AP-17, 443-451 (July 1969), DDC AD-696883.
11. A.J. Hatch and H.B. Williams, "The Secondary Electron Resonance Mechanism of Low Pressure High Frequency Breakdown," J. Appl. Phys. 25, 417-423 (April 1954).
12. "The Study of Multipactor Breakdown in Space Electronic Systems," Report No. P65-49, Aerospace Group, Hughes Aircraft Company (April 1965).
13. Space Programs Summary, Vol. IV: Supporting Research and Advanced Development, Jet Propulsion Laboratory  
     Summary No. 37-35, pp. 282-288, 31 October 1965  
     Summary No. 37-36, pp. 278-284, 31 December 1965  
     Summary No. 37-38, pp. 168-172, 217-223, 30 April 1966  
     Summary No. 37-39, pp. 106-112, 193-196, 30 June 1966  
     Summary No. 37-41, pp. 207-209, 242-247, 31 October 1966.
14. D.R. Bold, A. Sotiropoulos, "LES-6 Triplexer," Technical Report 459, Lincoln Laboratory, M.I.T. (2 December 1968), DDC AD-686418.
15. R.L. Sicotte and R.N. Assaly, "Intermodulation Products Generated by a p-i-n Diode Switch," Proc. IEEE 56, 74-75 (January 1968), DDC AD-668721.
16. R.N. Assaly and R.L. Sicotte, "IM and Switching Noise of a Pin Diode Switch in the UHF Band," NEREM Record 10, 214-215 (1968).
17. R.L. Sicotte and R.N. Assaly, "Intermodulation Product Switching Noise Amplitudes of a PIN Diode Switch in the UHF Band," Trans. IEEE Microwave Theory and Techniques, MTT-18, 48-50 (January 1970).
18. H.T. Friis, "Noise Figures of Radio Receivers," Proc. IRE 32, 419-422 (July 1944).
19. H.A. Haus, R.B. Adler, Circuit Theory of Linear Noisy Networks (Wiley, New York, 1959).
20. G.A. Dodson and B.T. Howard, "High Stress Aging to Failure of Semiconductor Devices," Proc. Seventh National Symposium on Reliability and Quality Control, p. 262 (1961).
21. L.J. Ricardi, "Directivity of an Array of Slots on the Surface of a Cylinder," Electronic Engineering 39, 578-581 (September 1967), DDC AD-668239.



DOCUMENT CONTROL DATA - R&D		
(Security classification of title, body of abstract and indexing annotation must be entered when the overall report is classified)		
1. ORIGINATING ACTIVITY (Corporate author)  Lincoln Laboratory, M. I. T.		2a. REPORT SECURITY CLASSIFICATION Unclassified
		2b. GROUP None
3. REPORT TITLE  Development of UHF Switch for LES-6 Satellite		
4. DESCRIPTIVE NOTES (Type of report and inclusive dates) Technical Report		
5. AUTHOR(S) (Last name, first name, initial)  Assaly, Robert N.		
6. REPORT DATE 4 December 1969	7a. TOTAL NO. OF PAGES 130	7b. NO. OF REFS 21
8a. CONTRACT OR GRANT NO. AF 19(628)-5167		9a. ORIGINATOR'S REPORT NUMBER(S) Technical Report 473
b. PROJECT NO. 649L		9b. OTHER REPORT NO(S) (Any other numbers that may be assigned this report) ESD-TR-69-386
c.		
d.		
10. AVAILABILITY/LIMITATION NOTICES  This document has been approved for public release and sale; its distribution is unlimited.		
11. SUPPLEMENTARY NOTES  None		12. SPONSORING MILITARY ACTIVITY  Air Force Systems Command, USAF
13. ABSTRACT  <p>A UHF switch matrix was developed for the LES-6 satellite to electronically despin the antenna beam as the satellite rotated on its axis. Initially, a study was carried out to determine the optimum antenna system and switch configuration for the constraints of satellite geometry and minimal complexity. Two such switch matrices, operated by logic circuits and sun and earth sensors, were used on the satellite, one to excite two adjacent of eight pairs of antenna dipoles, and the other to excite two adjacent of eight pairs of cavity-backed slots. The polarizations of the signals from the dipoles and slots are orthogonal and by adjusting the phase difference to 90°, the satellite will, in normal operation transmit and receive on right-hand circular polarization. Furthermore, by squinting the beam formed by two element pairs +11.25° or -11.25° from the center line of the element pairs, any of 16 beams can be formed which are equally spaced in azimuth about the satellite. Each switch consists of three parts, namely, a hybrid to divide the input power into two equal parts, a 2P2T section which switches phase, and two SP4T sections to switch on two antenna pairs.</p> <p>The switch was built in strip transmission line using PIN diodes in series with the inner conductor as the switching element. In its development, a number of conflicting characteristics were required to be optimized. These include the RF characteristics such as the VSWR, insertion loss, and isolation; thermal heating of the diodes which determine their reliability; and intermodulation products, switching noise, and random noise which can degrade the satellite receiver performance. It was also necessary to demonstrate that the switch was free from multipactor breakdown and could survive prolonged space radiation. Finally, it had to be proven that the switch had good reliability under the stresses of the rocket launch and through an expected 5-year life in orbit.</p> <p>A detailed discussion of the testing programs is given, as this type of information is not generally available in the open literature.</p>		
14. KEY WORDS  LES-6 intermodulation products UHF switch  PIN diodes communication satellites antenna switch  switch matrix switching noise diode reliability		